

(NASA-CR-175446) INTERACTION OF
TWO-DIMENSIONAL TRANSVERSE JET WITH A
SUPERSONIC MAINSTREAM Research Report,
period ending Aug. 1983 (Old Dominion Univ.,
Norfolk, Va.) 124 p HC AC6/MF AD1 CSCL 01A G3/02 18380

N84-20492

Unclass

DEPARTMENT OF MECHANICAL ENGINEERING AND MECHANICS
SCHOOL OF ENGINEERING
OLD DOMINION UNIVERSITY
NORFOLK, VIRGINIA

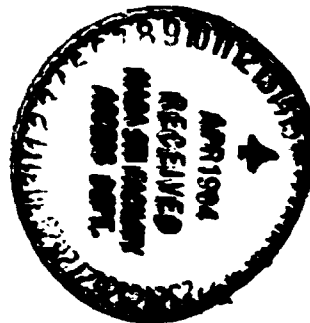
INTERACTION OF TWO-DIMENSIONAL TRANSVERSE
JET WITH A SUPERSONIC MAINSTREAM

By

G.C. Kraemer

and

S. N. Tiwari



Research Report
For the period ending August 1983

Prepared for the
National Aeronautics and Space Administration
Langley Research Center
Hampton, Virginia

Under
Grant NGR 47-003-052
Robert H. Tolson, Technical Monitor
Office of the Chief Scientist

December 1983

DEPARTMENT OF MECHANICAL ENGINEERING AND MECHANICS
SCHOOL OF ENGINEERING
OLD DOMINION UNIVERSITY
NORFOLK, VIRGINIA

INTERACTION OF TWO-DIMENSIONAL TRANSVERSE
JET WITH A SUPERSONIC MAINSTREAM

By

G. O. Kraemer

and

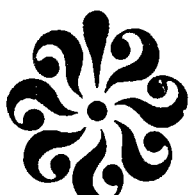
S. N. Tiwari

Research Report
For the period ending August 1983

Prepared for the
National Aeronautics and Space Administration
Langley Research Center
Hampton, Virginia

Under
Grant NGR 47-003-052
Robert H. Tolson, Technical Monitor
Office of the Chief Scientist

Submitted by the
Old Dominion University Research Foundation
P. O. Box 6369
Norfolk, Virginia 23508



December 1983

FOREWORD

The work presented in this report was conducted as a part of the "Graduate Engineering Research Participation in Aeronautics" program during the period 1980-82. The work was essentially completed by the end of August 1982, but certain modifications were made in 1983. The work was supported by the NASA/Langley Research Center through Grant NGR-47-003-052. The principal investigator of the Grant was Dr. A. Sidney Roberts, Professor of Mechanical Engineering and Mechanics at Old Dominion University. The Grant was monitored by Mr. Robert H. Tolson, Chief Scientist, NASA/Langley Research Center. The authors are grateful to Dr. R. Clayton Rogers of NASA Langley Research Center for providing extensive guidance and help during the entire course of this study.

TABLE OF CONTENTS

	Page
LIST OF TABLES.....	v
LIST OF FIGURE.....	vi
LIST OF SYMBOLS.....	x
1. INTRODUCTION.....	1
2. APPARATUS AND PROCEDURE.....	5
2.1 Model Apparatus.....	5
2.2 Instrumentation.....	13
2.3 Survey Procedure.....	17
3. DATA REDUCTION.....	18
4. RESULTS AND DISCUSSION.....	21
4.1 Visual Data.....	25
4.2 Surface Pressure Distribution.....	28
4.3 Surface Mole Fraction Distribution.....	41
4.4 Static and Pitot Pressure Profile.....	48
4.5 Mole Fraction Profile.....	62
4.6 Mass Flux Profile.....	69
5. COMPARISON OF THEORY WITH DATA.....	74
5.1 Model for Theoretical Investigation.....	74
5.2 Comparison of Results for Surface Distributions.....	76
5.3 Comparison of Results for Downstream Profile.....	82
6. CONCLUDING REMARKS.....	97

REFERENCES.....99

APPENDIX A. ERROR ANALYSIS.....102

LIST OF TABLES

Table	Page
1. Surface tap location.....	9
2. Test conditions for surface pressure distributions.....	22
3. Mean test conditions for the downstream surveys.....	23

LIST OF FIGURES

Figures	Page
1. Sketch of the aerodynamic features.....	6
(a) Sketch of model.....	7
(b) Photograph of model.....	8
2. Schematic of the jet supply.....	12
3. Survey probe design and position in probe wake.....	14
4. Schematic of sample collection system.....	16
5. Schlieren photographs for helium injection, $b = 0.043 \text{ cm}$	26
6. Schlieren photographs for nitrogen injection, $b = 0.043 \text{ cm}$	27
7. Surface pressure distribution correlation	
(a) $\text{PR} = 10$, helium injectant.....	30
(b) $\text{PR} = 10$, nitrogen injectant.....	31
(c) $b \times \text{PR} = 1.1$, nitrogen injectant.....	32
8. Effect of jet pressure on the surface pressure distribution, $b = 0.056 \text{ cm}$:	
(a) Helium injectant.....	34
(b) Nitrogen injectant.....	35
9. Dependence of $x_{1.5}$ on the jet parameters for helium and nitrogen:	
(a) For jet strength.....	38
(b) For jet momentum factor, $\gamma_j \times b \times \text{PR}$	38

Figure	Page
10. Correlation of surface pressure distributions by $x_{1.5}$, $b = 0.056$ cm	
(a) Upstream surface distributions offset by $x_{1.5}$	39
(b) Downstream surface distributions scaled by $x_{1.5}$	39
11. Injectant mole fraction surface distribution correlation	
(a) PR = 10, helium injectant.....	42
(b) PR = 10, nitrogen injectant.....	43
(c) $b \times PR = 1.1$, nitrogen injectant.....	45
12. Effect of jet pressure on the surface mole fraction distribution, $b = 0.056$ cm:	
(a) Helium injectant.....	46
(b) Nitrogen injectant.....	47
13. Nondimensional static pressure profile correlations	
(a) PR = 10, $x/b = 68$	51
(b) $b \times PR = 1.1$	52
14. Effects of downstream location of the static pressure profiles, PR = 10, $b = 0.056$ cm.....	54
15. Effect of jet pressure on the static pressure profiles, $x/b = 68$, $b = 0.056$ cm.....	55
16. Nondimensional pitot pressure profile correlation	
(a) PR = 10, $x/b = 68$	58
(b) $b \times PR = 1.1$	59
17. Effect of downstream location on pitot pressure profiles, PR = 10, $b = 0.056$ cm.....	60
18. Effect of jet pressure on the pitot pressure profiles, $x/b = 68$, $b = 0.056$ cm.....	61

Figure	Page
19. Injectant mole fraction profile correlation	
(a) PR = 10, x/b = 68.....	64
(b) b x PR = 1.1.....	65
20. Effect of downstream location on injectant mole fraction profiles, PR = 10, b = 0.056 cm.....	66
21. Effect of jet pressure on injectant concentration profiles, x/b = 68, b = 0.056 cm.....	68
22. Injectant mass flux profiles, b = 0.056 cm:	
(a) Helium injectant, PR = 10.....	71
(b) Helium injectant, PR = 20.....	71
(c) Nitrogen injectant, PR = 10.....	71
(d) Nitrogen injectant, PR = 20.....	71
23. Integrated mass flux variation with downstream survey location:	
(a) Total mass for PR = 5, 10, and 20.....	73
(b) Injectant mass.....	73
24. Comparison of surface pressure distributions, b = 0.056 cm:	
(a) Nitrogen injectant.....	76
(b) Helium injectant.....	77
25. Comparison of injectant mole fraction surface distributions, b = 0.056 cm:	
(a) Nitrogen injectant.....	80
(b) Helium injectant.....	81
26. Comparison of static pressure profiles, b = 0.056 cm:	
(a) Nitrogen injectant.....	84
(b) Helium injectant.....	85
(c) Helium injectant.....	86

Figure	Page
27. Comparison of pitot pressure profiles, $b = 0.056 \text{ cm}:$	
(a) Nitrogen injectant.....	88
(b) Helium injectant.....	89
(c) Helium injectant.....	90
28. Comparison injectant mole fraction profiles, $b = 0.056 \text{ cm}:$	
(a) Nitrogen injectant.....	91
(b) Helium injectant.....	91
29. Comparison of injectant mass flux profile.....	93
30. Comparison of total mass flux profile.....	94
31. Comparison of Mach number profile.....	95
A.1 Relative Mach number error.....	106
A.2 Relative mass flux error.....	108

LIST OF SYMBOLS

a	local sound speed
b	jet gap width
C _p	specific heat at constant pressure
C _D	discharge coefficient of the jet
F	frequency of the turbine meter
h _s	jet shock height (Eq. 4.2)
ṁ _j	jet mass flow rate
ṁ _T	model inlet ide'l mass flow rate
ṁ _{TM}	turbine meter mass flow rate
M	mach number
N/O	nitrogen to oxygen ratio
p	static pressure
p _b	tunnel supply pressure
p _{plume}	effective jet back pressure
p _t	pitot pressure
p _{t,j}	jet total pressure
p _{TM}	turbine meter pressure
p _w	surface pressure
p _{w,∞}	surface pressure from first surface tap
PR	jet to mainstream static pressure ratio
R̄	gas constant = universal gas constant/molecular weight of gas
T	static temperature
T _b	tunnel supply te:merature

xi

$T_{t,j}$	jet total temperature
T_{TM}	turbine meter temperature
u	axial velocity
x	axial distance (Fig. 1a)
$x_{1.5}$	location at which $p_w/p_\infty = 1.5$ in upstream region
X	volume fraction
y	vertical distance (Fig. 1a)
z	transverse distance (Fig. 1a)
α	mass fraction
γ	specific heat ratio
θ	separation shock deflection angle
ρ	density

Subscripts

1	air quantity
j	jet quantity
∞	undisturbed mainstream quantity

INTERACTION OF A TWO-DIMENSIONAL TRANSVERSE JET WITH A SUPERSONIC MAINSTREAM

By

G. O. Kraemer¹ and S. N. Tiwari²

SUMMARY

An experimental investigation of the interaction of a two-dimensional sonic jet injected transversely into a confined main flow has been conducted. The main flow consisted of air at a Mach number of 2.9. The effects of varying the jet parameters on the flow field were examined using surface pressure and composition data. Also, the downstream flow field was examined using static pressure, pitot pressure, and composition profile data. The jet parameters varied were gapwidth, jet static pressure, and injectant species of either helium or nitrogen. The values of the jet parameters used were 0.039, 0.056, and 0.109 cm for the gapwidth and 5, 10, and 20 for the jet to mainstream static pressure ratios. The features of the flow field produced by the mixing and interaction of the jet with the mainstream were related to the jet momentum. The data were used to demonstrate the validity of an existing two-dimensional elliptic flow code.

¹ Graduate Research Assistant, Department of Mechanical Engineering and Mechanics, Old Dominion University, Norfolk, Virginia 23509. Present affiliation, AVCO-Lycoming, Stratford, Conn. 06497.

² Eminent Professor, Department of Mechanical Engineering and Mechanics, Old Dominion University, Norfolk, Virginia 23508.

1. INTRODUCTION

A serious effort is currently underway to design hydrogen fueled, supersonic combustion ramjets (scramjets) for hypersonic vehicle propulsion. In the present concept, gaseous hydrogen fuel is injected from transverse and parallel fuel injectors, located on instream struts, into the supersonic mainstream air flowing through the combustor [1]*. At high flight speeds, a large portion of the fuel is added from transverse fuel injectors due to their rapid mixing and heat releasing qualities. At lower flight speeds, an increased portion of the fuel might be added from parallel fuel injectors to prevent possible thermal choking. These fuel injectors are generally operated at sufficient jet stagnation pressures so that the jet flow is sonic at the jet exit.

The flow produced by the interaction of a transverse fuel jet with a supersonic mainstream is quite complex. Sterrett et al. [2], for example, observed many of the typical flow features. The jet gas expands into the primary flow forming a plume shaped body, which eventually terminates at a strong normal shock wave. Formation of a curved bow shock and the separation of the turbulent boundary layer results from the obstruction produced by the jet body. An upstream separation shock is formed above the recirculation region. Downstream of the jet, the flow turns downward to the injection surface

* The number in brackets denote references.

producing a recompression shock near the location of boundary layer reattachment. A low pressure downstream recirculation region is formed due to the rapid expansion of the mainstream flow behind the jet. Both of these recirculation regions contain embedded regions of subsonic and supersonic flow. Due to these embedded subsonic regions, an elliptic flow theory is needed to analytically describe the transverse jet interaction (TJI) flow field. Because of the complexity and the large computer storage required to solve the elliptic computational flow theory, only the two-dimensional flow case has been examined at present [3].

Historically, interest in this type of TJI flow field was for applications to rocket thrust vector control, hypersonic vehicle guidance control, and scramjet fuel injectors. These areas have been examined for the three-dimensional case, as discussed in a recent review by Rogers [4]. A critical review by Werle [5] examined the two-dimensional TJI literature until 1968. In this review and other literature after 1968 [2-16], the two-dimensional investigations were for application to thrust vector control and vehicle guidance control. Thrust vector control investigations [17,18] sought to predict the shape and location of the bow shock by assuming that there was no upstream boundary layer or separated region. Vehicle guidance control investigations were conducted to predict the increased side force due to the altered pressure field in the upstream separated region. These investigations provided useful information about the jet penetration and surface pressure distributions and led to an increased understanding of the TJI phenomenon.

Since 1968, two-dimensional TJI investigations have been, in general, directed towards developing scaling relationships for characterizing the flow for vehicle guidance control applications. A common scaling parameter was the effective obstruction height which was predicted from either a method using a force balance or a physical analogy. In the first method [7] the jet was mathematically substituted by a hemicylinder control volume of jet gas facing the primary flow. The cylinder's radius was calculated from a balance of the jet momentum flux out of the downstream face with the drag force on the upstream face (usually by a Newtonian drag model). Another popular method [6, 13, 15, 16] used a physical analogy between a jet exhausting into a quiescent atmosphere with one exhausting into a supersonic flow. For an assumed jet back pressure, the jet shock height was calculated. Once the jet penetration was determined from the calculated cylinder radius or jet shock height, correlations were developed to predict the upstream separation distance. All previous two-dimensional investigations were for unconfined flows, and these investigations were limited to the collection of surface pressure and composition distributions and visual data. In a confined flow, however, Wu et al. [9] predicted that the "squeezing" of the flow would cause a significant decrease in the jet penetration at the same conditions. This would result in a smaller flow field disturbance.

Past applications of two-dimensional TJI data required only limited experimental investigations for unconfined flows. The current development of flow theories useful for scramjet design requires data for the flow field near the jet in a confined super-

sonic flow. Acquisition of these data are the primary consideration of the present experimental investigation. Another objective of this study is to increase the understanding of the flow field and determine various scaling factors, correlations, and empirical relationships. To meet these objectives experimental data for a cold flow are obtained at the various jet parameters of jet strength, jet gap width, and injectant species.

The apparatus and procedures used to conduct the experimental investigation are presented in Chap. 2. A discussion of the assumptions and equations used to reduce the data is given in Chap. 3. Experimental results are discussed in Chap. 4. Theory and data are compared in Chap. 5. Conclusions drawn from this investigation are presented in Chap. 6. The appendix presents the error analysis of the method used to determine local Mach number and mass flux.

2. APPARATUS AND PROCEDURE

As mentioned in the introduction, the flow produced by the interaction of a transverse fuel jet with a supersonic flow is quite complex as shown in Fig. 1. The apparatus and procedures used in the experimental investigation of this flow are presented in this chapter. The model configuration, model supply, and jet supply are discussed in Sec. 2.1. The instrumentation and survey procedures are discussed in Secs. 2.2 and 2.3 respectively.

2.1 Model Apparatus

A sketch of half of the uniform rectangular duct model is shown in Fig. 2a. One of the two identical stainless steel injector plates is shown in the sketch. The injector plates are 7.62 cm apart. Another identical stainless steel side wall is separated from the one shown by 3.81 cm. When assembled the model is 30.5 cm long. The side wall is seen to have a 20.3 cm long glass window. Before bolting the model together a thin film of room-temperature vulcanizing rubber is applied to seal the model and prevent leaks.

The figure shows the initial sharp leading edge of 5° and the slot injector spans the injector plate at a distance of 17.8 cm downstream of the leading edge. The inside surfaces of the model side walls are spaced to fit flush and parallel with the nozzle side walls. Along the injector plate's centerline and in four lateral rows are flush surface taps containing 0.152 cm tubing (Fig. 2b). These surface tap locations are given in Table 1.

ORIGINAL PAGE IS
OF POOR QUALITY

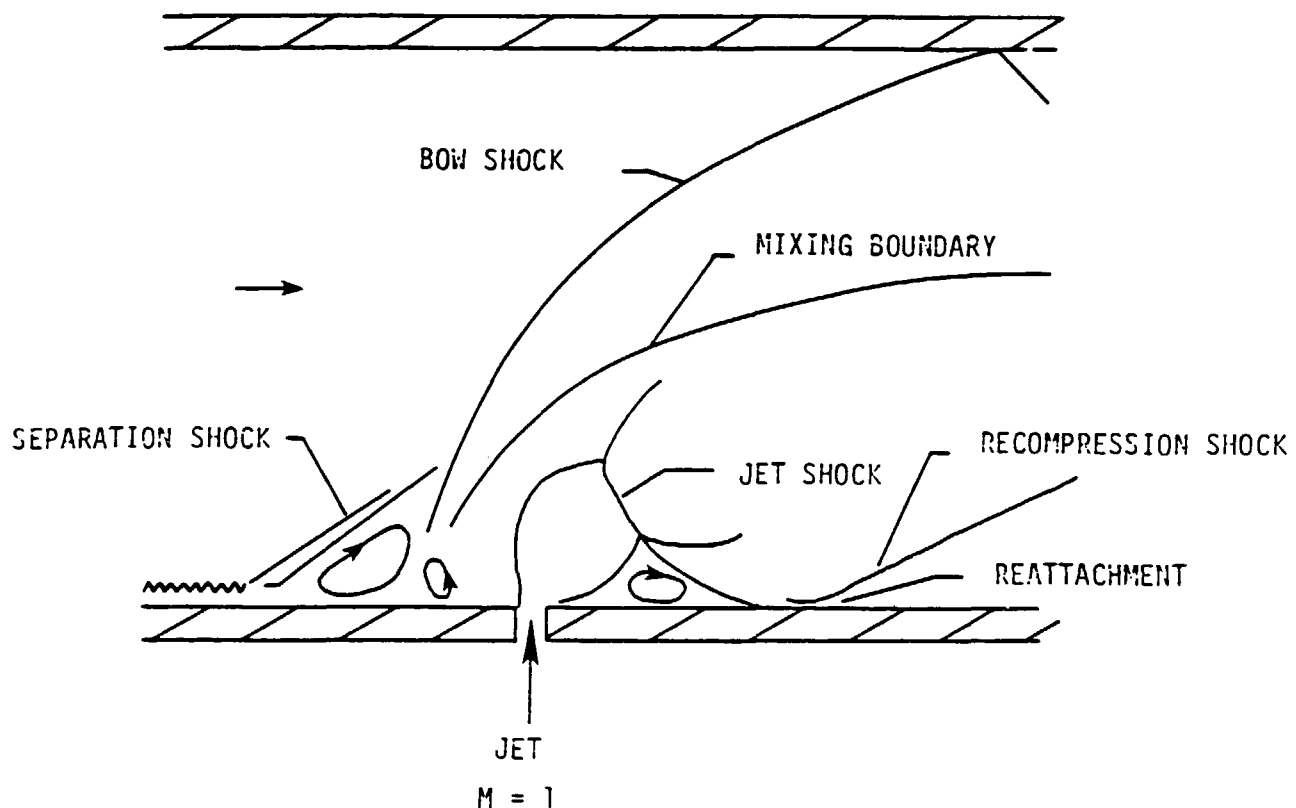


Fig. 1 Sketch of the aerodynamic features.

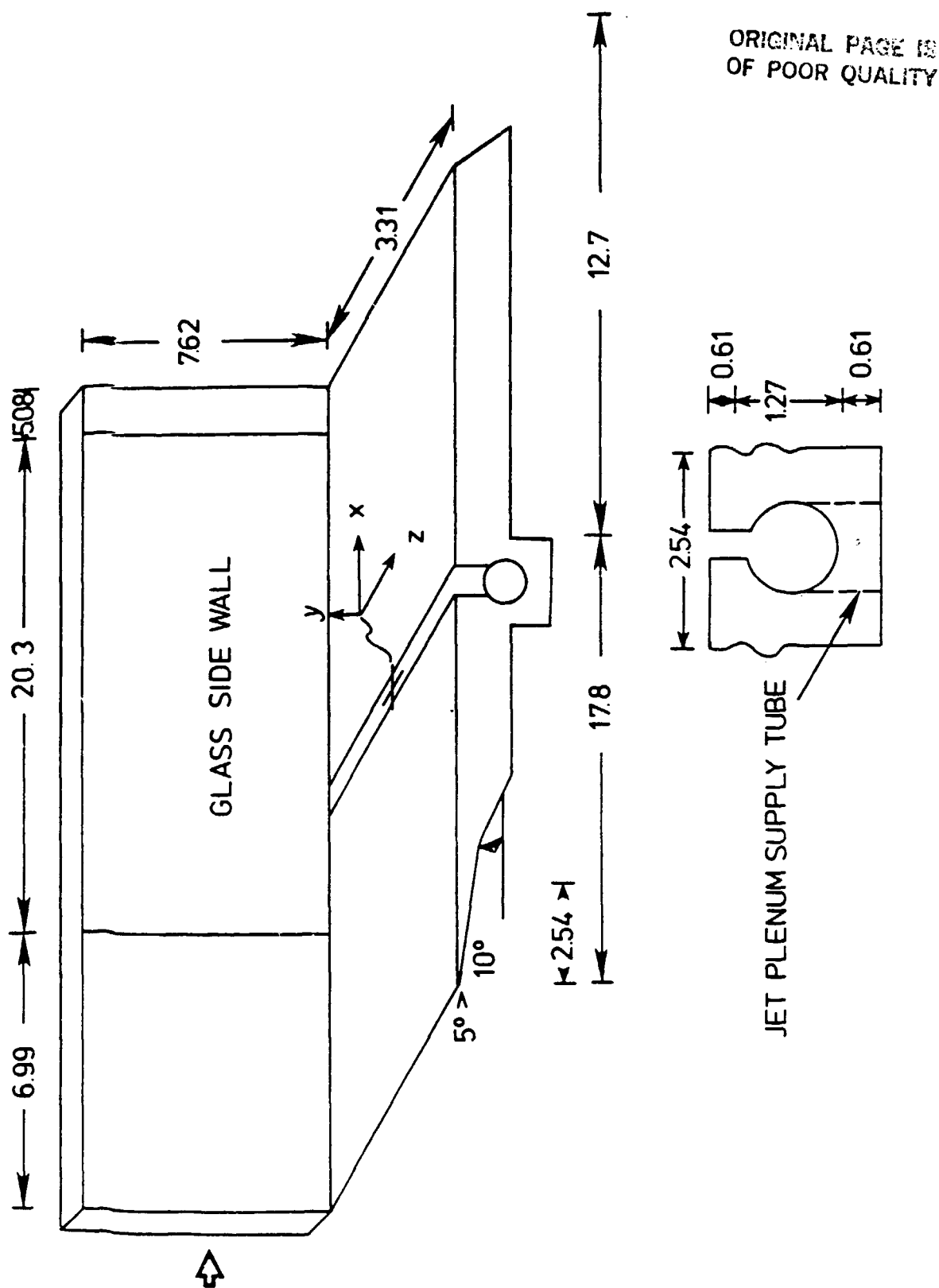
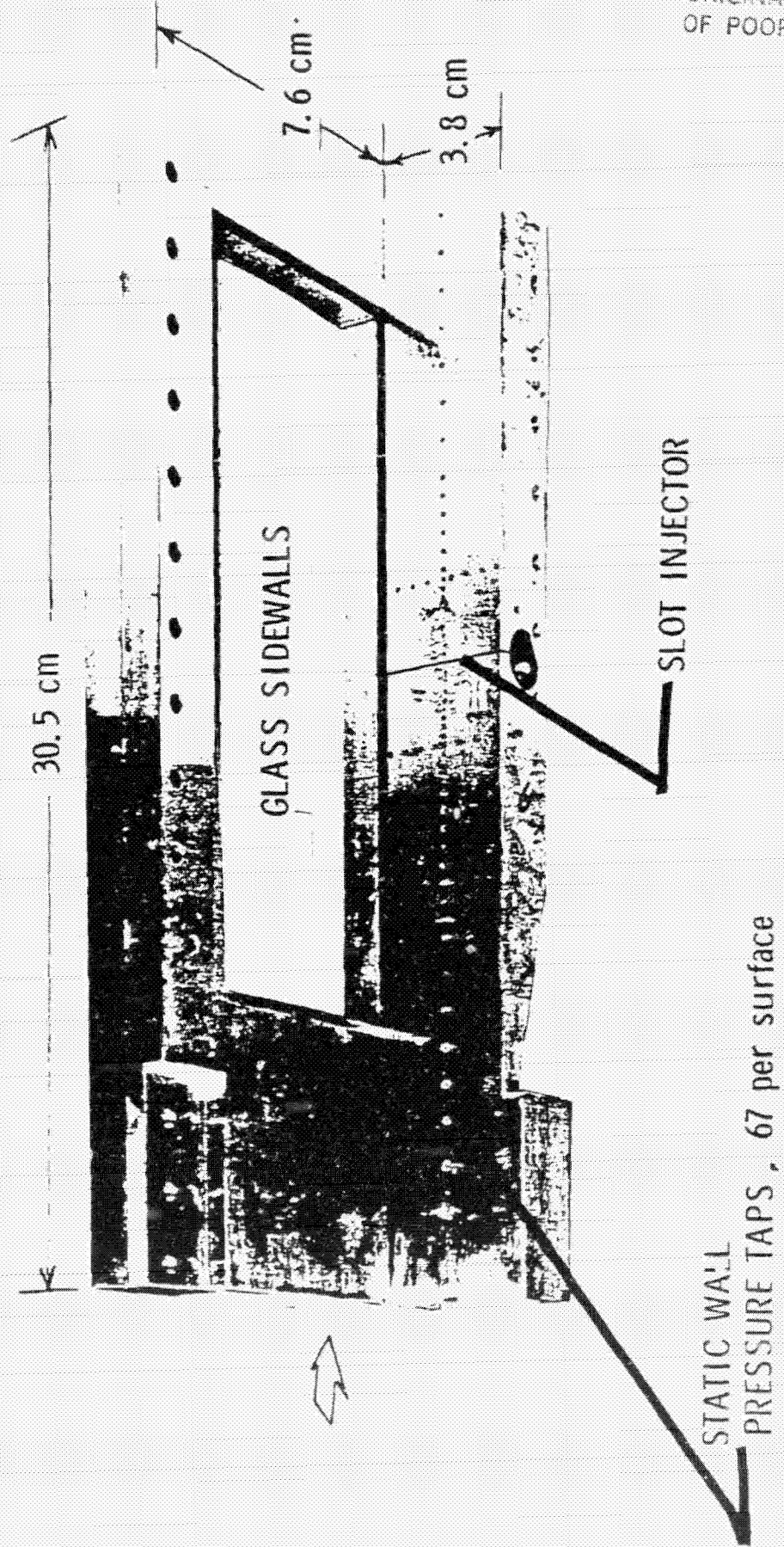


Fig. 2a. Model configuration: sketch of model, all dimensions in cm.



ORIGINAL PAGE IS
OF POOR QUALITY

Fig. 2b, Mode² configuration; photograph of model.

Table 1. Surface tap location * ORIGINAL PAGE IS
OF POOR QUALITY

For $b = 0.109$ and 0.056 cm				For $b = 0.039$ cm			
Upstream		Downstream		Upstream		Downstream	
x	z	x	z	x	z	y	z
-0.25	0	0.23	0	-0.25	0	0.25	0
-0.50	0	0.50	0	-0.50	0	0.47	0
-0.79	0	0.74	0	-0.78	0	0.73	0
-1.06	0	1.00	0	01.03	0	1.03	0
-1.28	0	1.27	0	01.28	0	1.24	0
-1.53	0	1.52	0	-1.54	0	1.51	0
-1.79	0	1.80	0	-1.79	0	1.77	0
-2.04	0	2.06	0	-2.04	0	2.02	0
-2.29	1.77	2.30	1.31	-2.29	1.77	2.28	1.31
-2.29	1.26	2.30	1.01	-2.29	1.26	2.28	1.01
-2.29	0.75	2.30	0.50	-2.29	0.75	2.28	0.50
-2.29	0.24	2.30	0	-2.29	0.24	2.28	0
-2.29	0	2.30	-0.26	-2.29	0	2.28	-0.26
-2.29	-0.52	2.30	-0.77	-2.29	-0.52	2.28	-0.77
-2.29	-1.02	2.30	-1.27	-2.29	-1.02	2.28	-1.27
-2.29	-1.53	2.30	-1.78	-2.29	-1.53	2.28	-1.78
-2.54	0	2.56	0	-2.57	0	2.53	0
-3.05	0	3.07	0	-3.07	0	3.04	0
-3.56	0	3.59	0	-3.58	0	3.55	0
-4.07	0	4.09	0	-4.09	0	4.05	0
-4.58	0	4.58	0	-4.59	0	4.56	0

* Zero z location is on centerline of model, dimensions in cm

ORIGINAL PAGE IS
OF POOR QUALITY

Table 1. Concluded.

For $b = 0.109$ and 0.056 cm				For $b = 0.039$ cm			
Upstream		Downstream		Upstream		Downstream	
x	z	x	z	x	z	x	z
-5.08	0	5.11	0	-5.11	0	5.07	0
-5.59	0.75	6.13	0	-5.61	0.75	6.09	0
-5.59	0	7.15	0	-5.61	0	7.10	0
-5.59	-1.54			-5.61	-1.54		
-6.10	0			-6.10	0		
-6.60	0			-6.63	0		
-7.10	0			-7.13	0		
-7.63	1.51			-7.64	1.51		
-7.63	0			-7.64	0		
-7.63	-0.77			-7.64	-0.77		
-8.64	0			-8.66	0		
-9.66	0			-9.68	0		
-10.46	0			-10.70	0		
-11.68	0			-11.71	0		
-12.69	0			-12.73	0		
-13.67	0			-14.00	0		
-15.26	0			-15.27	0		

The steel side walls of the model were modified to aid in spilling the nozzle side wall boundary layer and to permit surveys closer to the jet. Two solid stainless steel side walls were constructed with a 10° sharp leading edge and to overlap the injector plate by 0.32 cm. The model length was reduced by removing the last 5.08 cm of the model. The gap widths of the slot injector used were 0.039, 0.056, and 0.109 cm with a respective slot height to gap width aspect ratio of 16.3, 11.3, and 5.8.

The model was bolted flush atop an aluminum nozzle, with the model centered and square with the nozzle exit. The two-dimensional, Mach number 2.9 nozzle supplied the model with a constant air flow at a nominal total pressure of 2.07 MPa and an ambient total temperature of 300 K. Both were measured in a large supply section near the nozzle. An expected unit Reynolds number at these nominal conditions was 1.5×10^8 per meter in this blow down tunnel operation. The expected unit Reynolds number for the jet increased from 7.6×10^7 to 6.9×10^8 per meter with the jet pressure.

A schematic of the system for delivering the jet gas supply of either helium or nitrogen gas is shown in Fig. 3. The jet gas was delivered by a 1.27 cm stainless steel tubing from 0.054 m³ standard cylinders at an initial pressure of about 14 MPa. After an initial pressure regulating valve, an air operated pressure regulating valve was used to set the desired jet total pressure. Downstream, a standard turbine meter with a 19.1 cm long and 1.57 cm diameter flow straightening tube was used to determine the jet gas volumetric flow rate. Measured pressure and temperature at the turbine meter and

ORIGINAL PAGE IS
OF POOR QUALITY

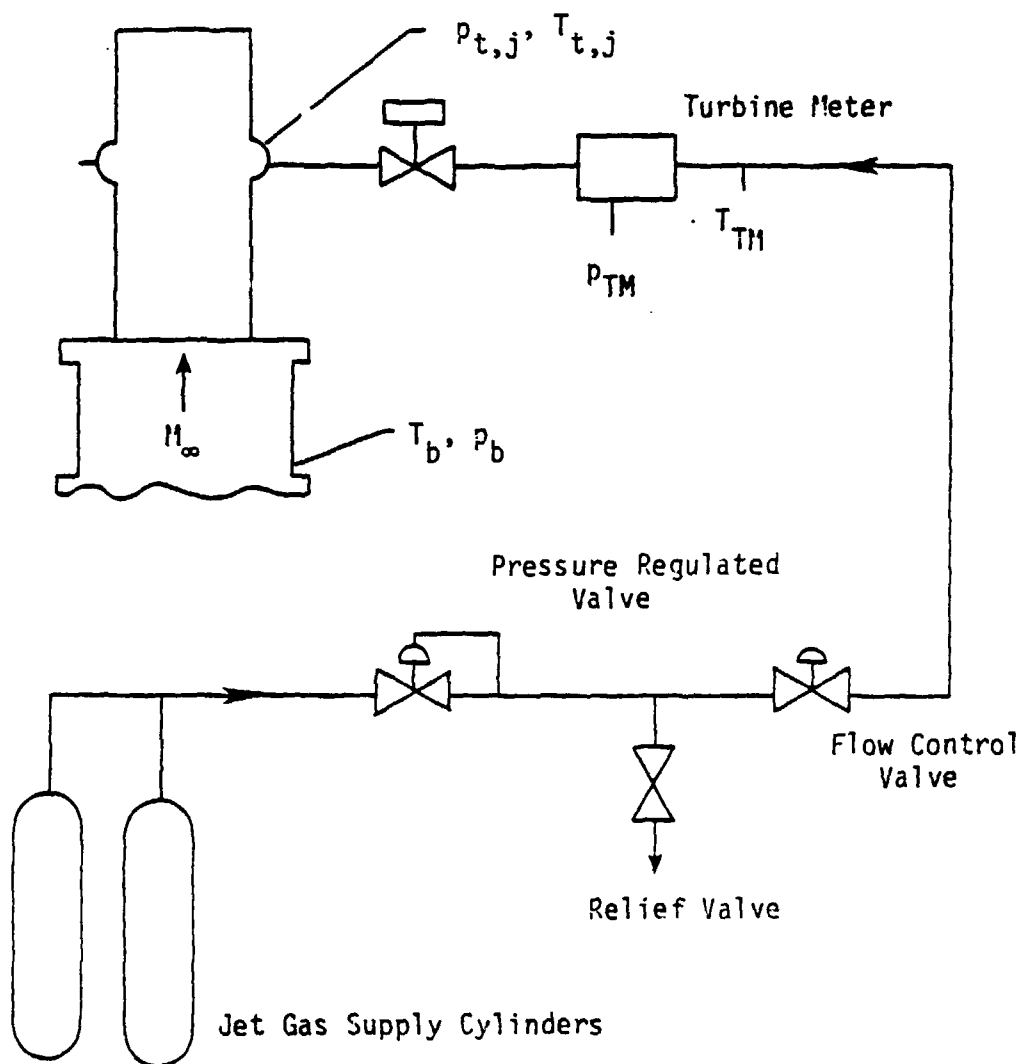


Fig. 3. Schematic of the jet supply.

flow straightening tube assembly were used to compute the jet mass flow rate. An identical system delivers the jet gas to the other jet plenum.

2.2 Instrumentation

2.2.1 Visual Method

Schlieren photographs were taken to examine the shock structure for the various jet strengths and injectant species. This single-pass schlieren system consisted of a mercury vapor lamp, two spherical mirrors, and a vertical knife edge. Reference wires were placed exterior to the flow for the photographs.

2.2.2 Probes

Instream surveys were made with either a six probe pitot rake or a six probe static rake. Details of the probe tips and installation into the probe rake can be seen in Fig. 4. More information about the short static probe can be found in a report by Pinckney [19]. The pitot probes (0.32 cm O.D.) were welded flush together to allow collection of gas samples near the injection surface. The static probes were spaced 1.02 cm tip to tip so that they would not interfere with one another. A support of adjustable height in back of each injector plate maintained the probes parallel to the undisturbed mainstream flow as they traversed the model vertically. A linear slide potentiometer-voltmeter system was used to monitor the first probe position from the injector plate. This system had an estimated accuracy of about 0.005 cm.

2.2.3 Gas Sampling and Analysis System

A schematic of the sampling system for one of the six possible

*Survey Probe
Probe Rake Assembly*

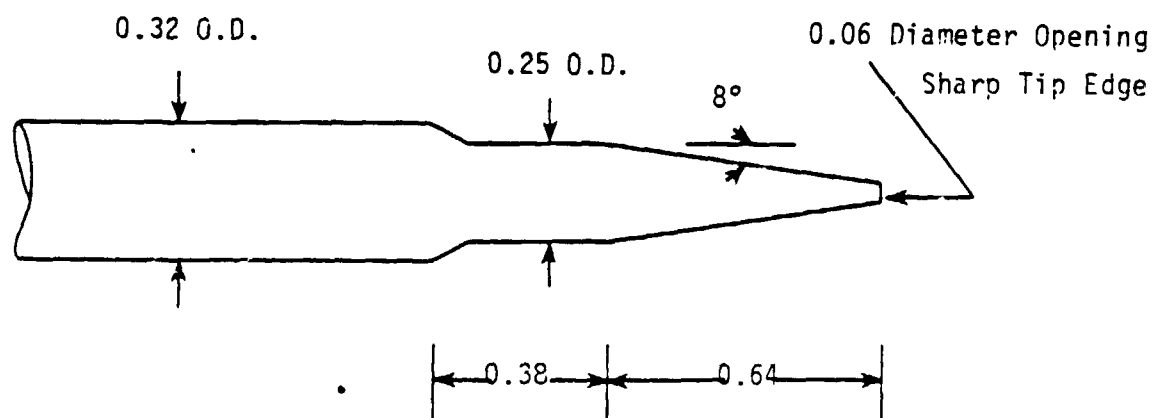
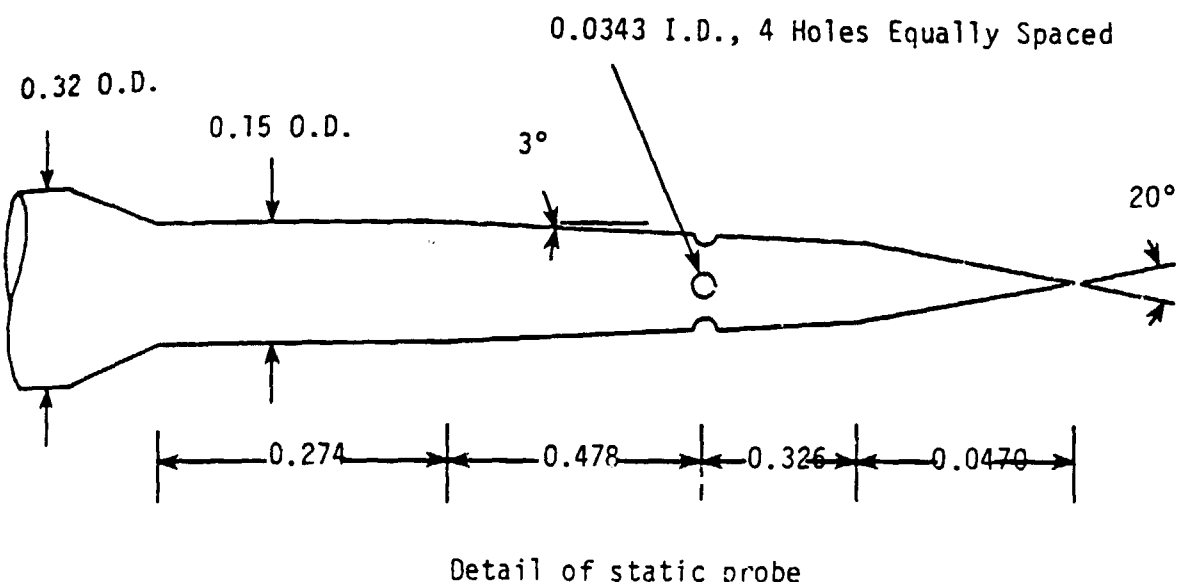
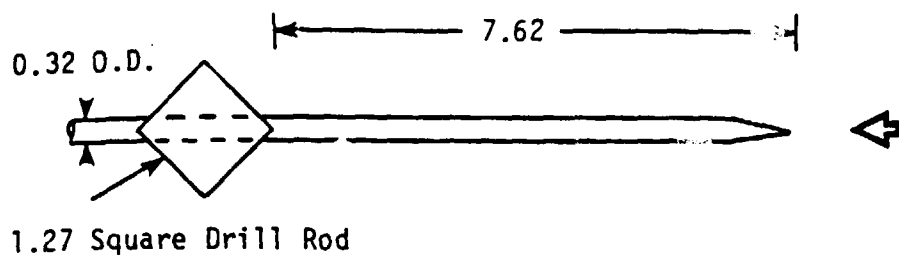


Fig. 4. Survey probe design and position in probe rake, all dimensions in cm.

sources is shown in Fig. 5. The system allowed individual collection and storage of six samples at one time in one of four sets of six sample collection bottles.

For sample collection, the system was first preevacuated. When sampling was desired, the probe side vacuum system was closed. Then, the appropriate valves were opened to allow the sample to establish flow through the collection bottles for about ten seconds. Next, a valve on the vacuum side of the sample bottle was closed. After a few seconds, a valve on the probe side of the sample bottle was closed to isolate the sample. This procedure was repeated for all four sets of sample bottles.

The samples were analyzed individually by a quadrupole mass spectrometer. To maintain a uniform analysis procedure an automatic sequencer was used to control sample delivery. After an evacuation, the sample collection bottle was briefly opened to fill the sample coil. Then by use of a downstream vent, the sample was delivered to the mass spectrometer system at room pressure. By using a controlled vacuum system the pressure at the mass spectrometer's porous plug entrance was kept at approximately 3.4 KPa. After establishing this condition, the analysis data were recorded for ten seconds. The mass spectrometer was calibrated with air, helium, and hydrogen individually prior to analyzing the collected samples.

2.2.4 Other Instrumentation

Wall static pressures were measured by using an Electronic Scanning Pressure system similar to that described by Trexler [20]. The measurements were made by using 0-10 KPa absolute range pressure transducers. The pressure measurements were accurate within

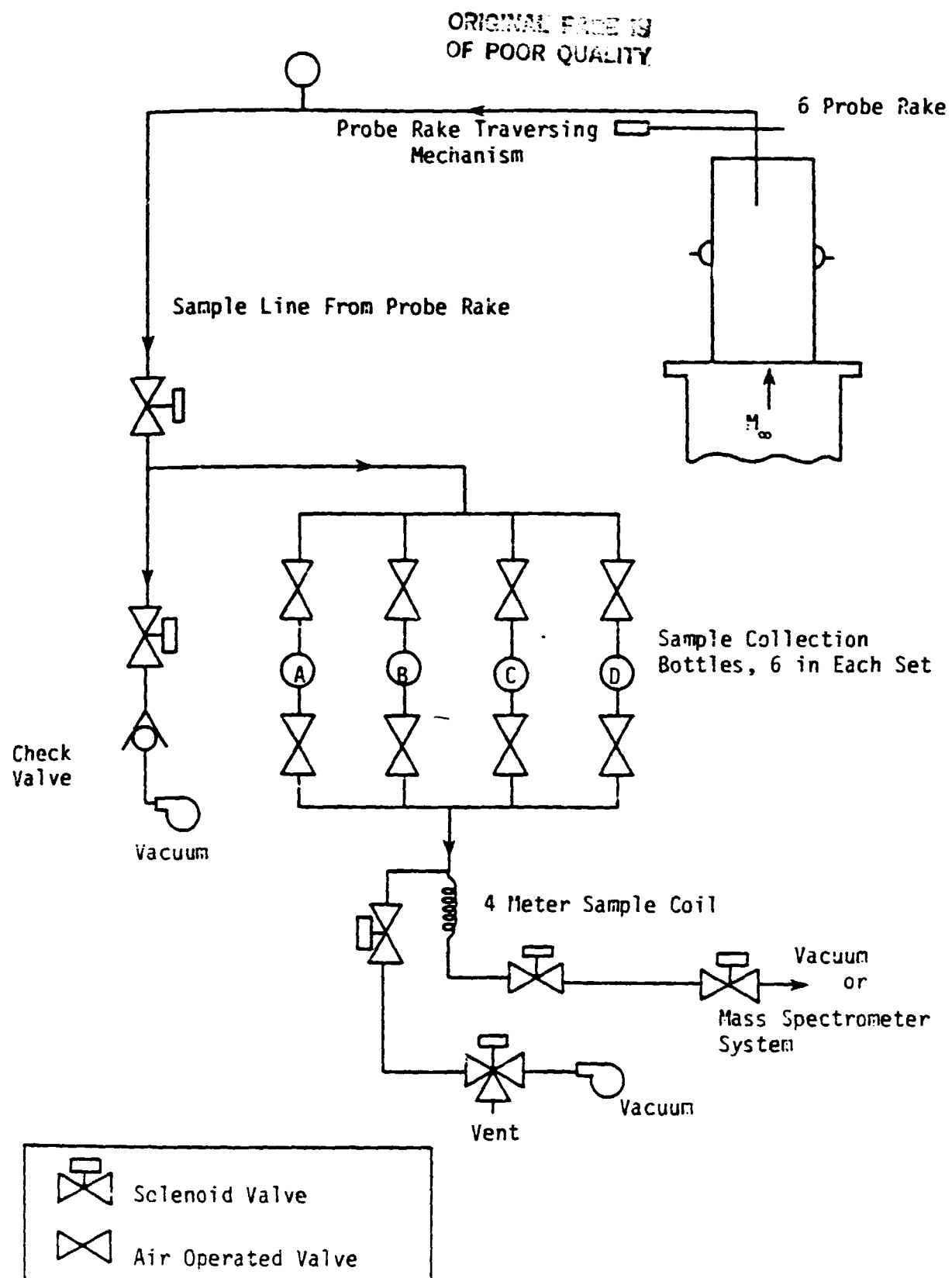


Fig. 5. Schematic of sample collection system.

0.25 percent of full scale. The tunnel and jet total pressures were measured by 3.45 MPa gauge range pressure transducers. All six pitot probe pressures were measured by 1.38 MPa gauge range pressure transducers. The static pressure measurements were made by 0.345 MPa or less absolute range pressure transducers. Standard copper constantan thermocouples were used to make the temperature measurements, and they were specified to be accurate within 1° C by the manufacturers. A two point calibration of the individual thermocouple was determined by use of a reference thermocouple and a known potential source.

2.3 Survey Procedure

Vertical surveys were made at the injector plate centerline at downstream locations of 34, 64, 68, 71, 114 jet gap widths for jet to mainstream static pressure ratios of 5 to 20. Pitot and static pressure surveys were made by recording the pressure from the appropriate probe rake at 4 to 5 locations across the duct. When the probe rake was moved to the desired location, a signal could be sent to a remote computer to record the data. The data were averaged over one second before being printed and stored. Analysis of several one second data records, spaced three seconds apart at the same test conditions, showed the one second average was sufficient to provide precise values. At selected locations near the injection wall, both pitot pressure and gas samples were collected for certain test conditions. Gas samples were collected from selected surface taps during static surveys. In general, gas samples were collected for a jet mainstream static pressure ratios of 10 to 20.

3. DATA REDUCTION

Data from separate pitot and static pressure surveys and the gas sample analysis (if collected) were combined to determine the local flow properties at each of the pitot probe locations for similar test conditions (i.e., same jet conditions and downstream location). The local flow properties were calculated at the pitot probe locations, since the pitot probes were used to collect instream gas samples. Since pitot and static data were recorded at different locations, the static pressures were calculated by a cubic spline interpolation at the pitot probe locations. Where gas samples were not collected, the local mixture composition was assumed to be that of air.

A mass spectrometer was used to determine the gas sample composition based on analysis of the major peak of nitrogen, helium, oxygen, and argon. During a ten second data collection period the peak height and the porous plug pressure were averaged after an equal and separate analysis interval for each constituent. These data and a calibration constant were used to determine the mole fraction of each constituent by an existing program [21].

The calibration constant for each constituent was calculated by subtracting the background peak height in a vacuum from the peak height observed for a known concentration of constituent and dividing by the product of the porous plug pressure and known concentration of constituent. In this and subsequent data reduction

the model fraction of the constituents of air were assumed to be 0.7803 nitrogen, 0.2099 oxygen, and 0.0098 argon. A linear Lever rule relationship was used to calculate the mole fraction of each constituent by again subtracting the background from the sample peak height and dividing by the product of the porous plug pressure and the calibration constant. Although a simple proportionality between the porous plug pressure and the peak height was assumed in the program, a nonlinear relationship really existed. This assumption caused a maximum error in the mole fraction of 0.004 for air. The mole fractions of N₂, O₂, and He were finally normalized by their sum to correct for drift in the analyzer.

In order to determine the mole fraction of air in each sample, the sample was considered to be a binary mixture of air and injectant. For helium injection, the calculation of the air mole fraction was made directly. For nitrogen injection, the mole fraction of air was determined from the increase in the nitrogen to oxygen ratio (N/O) above that of air

$$N/O = (X_{N_2}/X_{O_2})/(0.7803/0.2099)$$

where X_{N₂} and X_{O₂} are observed mole fractions of N₂ and O₂ respectively. The mole fraction of air is then found by

$$X_1 = 1 - (0.7803(N/O - 1))/(1 + 0.7803(N/O - 1))$$

Then, the mass fractions for air and injectant were determined using the molecular weight of dry air as 28.97, nitrogen as 28.00, and helium as 4.00.

From the mixture specific heat ratio, pitot pressure, static pressure, air mass fraction, and tunnel total pressure and temperature, the local mixture Mach number and the total (and injectant) mass flux were computed by using the equations for the one-dimensional isentropic flow of an ideal gas [22]. The mixture specific heat ratio was calculated by mass averaging the specific heats and gas constants for air and injectant gas. The value of the universal gas constant was taken as 28980 for air, 20787 for helium, and 29103 J/kg-mole K for nitrogen. The total and injectant mass fluxes were integrated by a trapezoidal rule method to examine the overall data quality. The discharge coefficient of the jet was determined from the turbine meter mass flow rate divided by the ideal jet mass flow rate. The turbine meter volumetric flow rate was found from a linear least squares curve fit to calibration data relating it to the turbine meter frequency. This was done over various segments of the fairly linear curve so that no significant error occurred in the calculation of the turbine mass flow rate. An error analysis of the Mach number and mass flux equations is given in Appendix A.

4. RESULTS AND DISCUSSION

Results of an experimental investigation of the interaction and mixing of a two-dimensional sonic jet, injected transversely into a Mach number 2.9 air mainstream, are discussed in this chapter. Test conditions included variation of the jet gap width (b), the jet-to-mainstream static pressure ratio (PR), and the injectant species of either helium or nitrogen. Tests were conducted for nominal values of PR of 5, 10, and 20 at gap widths of 0.039, 0.056, and 0.109 cm. Typical features of the flow were visualized qualitatively in schlieren photographs. Distributions of pressure and injectant mole fraction were obtained along the centerline of the injection wall. Profiles of static pressures, pitot pressures, and injectant mole fraction were obtained along the injection wall centerline at locations 1.9, 2.8, 3.8, 6.4, and 7.0 cm downstream of the jet. Scaling parameters, correlations, and empirical relations are presented for the surface distributions and vertical profiles. An examination of the nature of the jet parameters governing the flow was made from the data trends and empirical relationships.

The test conditions, jet mass flow rate (m_j), and discharge coefficient of the jet (C_d) are given in Table 2 for runs in which the surface pressure distributions were measured, and Table 3 for runs in which surveys of the downstream flow were made. Gas samples were collected from surface taps during static pressure surveys. The test conditions were found to vary less than 0.5 percent from the

Table 2. Test conditions for surface pressure distributions

Injectant	b (cm)	PR	P_b (MPa)	P_{TH} (MPa)	F (hz)	T_b (K)	$T_{t,j}$ (K)	\dot{m}_{TH} (kg/sec)	c_D	$P_{W,\infty}$ (kPa)
He	0.109	9.4	2.18	1.64	*	298	292	292	78	78
He	0.109	4.5	2.19	0.80	*	298	291	290	74	74
He	0.056	20.5	2.11	2.98	1279	288	288	0.044	0.95	69
He	0.056	10.3	2.11	1.50	1261	288	284	0.022	0.95	70
He	0.056	5.0	2.09	0.73	1254	287	283	0.011	0.95	70
He	0.039	20.4	2.11	2.97	1035	297	294	292	0.031	0.94
He	0.039	9.1	2.10	1.32	1010	298	293	292	0.013	0.92
He	0.039	5.4	2.08	0.78	968	298	292	0.008	0.88	71
N ₂	0.109	10.2	2.11	1.55	707	298	288	0.089	0.85	73
N ₂	0.109	4.8	2.09	0.72	702	289	286	0.041	0.85	72
N ₂	0.056	19.8	2.10	2.62	438	292	281	278	0.093	0.88
N ₂	0.056	9.9	2.12	1.35	427	293	278	274	0.047	0.88
N ₂	0.056	5.2	2.05	0.69	421	292	278	274	0.024	0.88
N ₂	0.039	19.7	2.09	2.58	359	295	292	288	0.066	0.92
N ₂	0.039	9.7	2.10	1.28	368	298	293	291	0.034	0.94
N ₂	0.039	5.0	2.10	0.67	363	299	293	292	0.017	0.93
										71

CLOUDS INDICATE
OF POOR QUALITY

* overranged frequency meter

Table 3. Mean test conditions for the downstream surveys.

Injectant	b (cm)	PR	x (cm)	p_b (MPa)	p_{TM} (MPa)	F (Hz)	T_b (K)	$T_{t,j}$ (K)	m_{TM} (kg/sec)	c_0
He	0.056	20.0	1.9	2.12	2.92	1284	291	290	0.043	0.95
He	0.056	20.0	3.8	2.10	2.91	1284	295	290	0.043	0.95
He	0.056	21.4	6.4	2.11	2.94	1306	302	297	0.044	0.90
He	0.039	20.2	2.8	2.11	2.93	1025	296	297	0.029	0.92
He	0.109	9.5	7.0	2.09	1.65	*	300	296	0.043*	1.00*
He	0.056	9.8	1.9	2.10	1.43	1263	292	284	0.021	0.95
He	0.056	10.1	3.8	2.09	1.46	1267	294	286	0.022	0.95
He	0.056	9.9	6.4	2.11	1.44	1292	303	293	0.021	0.96
He	0.039	9.4	2.8	2.11	1.37	997	297	295	0.014	0.90
He	0.109	4.6	7.0	2.11	0.81	*	200	294	0.021*	1.00*
He	0.056	4.9	1.9	2.14	0.72	1258	293	283	0.011	0.95
He	0.056	5.1	3.8	2.11	0.75	1264	294	286	0.011	0.96
He	0.056	4.8	6.4	2.12	0.71	1286	303	293	0.010	0.96
He	0.039	5.1	2.8	2.11	0.75	945	297	294	0.007	0.84

ORIGINAL PAGE IS
OF POOR QUALITY* over ranged frequency meter i.e., m_{TM} is found from the jet conditions and for $c_0 = 1.00$

Table 3. Concluded.

Injectant	b	p _R	x	p _b	p _{TM}	F	τ _b	τ _{t,j}	τ _{TM}	c _D
	(cm)	(cm)	(MPa)	(MPa)	(Hz)	(K)	(K)	(kg/sec)		
N ₂	0.056	19.7	1.9	2.12	2.63	442	292	280	0.094	0.89
N ₂	0.056	19.9	3.8	2.11	2.64	440	296	285	0.093	0.88
N ₂	0.056	20.5	6.4	2.11	2.73	449	297	287	0.096	0.89
N ₂	0.039	18.8	2.8	2.11	2.49	366	297	294	0.064	0.93
N ₂	0.109	9.7	7.0	2.19	1.52	710	300	290	0.087	0.85
N ₂	0.056	10.0	1.9	2.12	1.33	436	291	277	0.047	0.88
N ₂	0.056	10.0	3.8	2.10	1.32	428	296	280	0.046	0.86
N ₂	0.056	1.01	6.4	2.10	1.34	443	297	283	0.047	0.89
N ₂	0.039	9.9	2.8	2.12	1.32	362	296	292	0.034	0.92
N ₂	0.109	4.6	7.0	2.18	0.72	704	300	288	0.041	0.85
N ₂	0.056	5.0	1.9	2.10	0.66	430	291	278	0.023	0.87
N ₂	0.056	5.1	3.8	2.09	0.67	422	295	281	0.023	0.85
N ₂	0.056	4.9	6.4	2.11	0.65	437	297	285	0.023	0.87
N ₂	0.039	4.9	2.8	2.11	0.65	355	297	291	0.017	0.91

ORIGINAL PAGE IS
OF POOR QUALITY

mean survey value given in Table 3. The actual jet pressure ratios were close to the desired nominal values ($PR = 5, 10,$ and 20). In general, the discharge coefficient of the jet varies between 0.84 and 0.95 .

4.1 Visual Data

The basic flow features are visualized by schlieren photographs, and typical results are shown in Figs. 6 and 7. Figure 6 shows the flow features produced by helium injection at several jet pressures. A separation shock, bow shock, and recompression shock are typical features produced by the jet disturbance. A small jet plume is observed near the injector surface for the larger jet pressure ratios. Weak shocks of about 1° turning angle originate at the leading edge of the injection wall. A fixed set of external reference lines aid in observing the effects of increasing the jet pressure. As the jet pressure increases, the origin of the separation shock moves upstream while maintaining a nearly constant angle of 32° . Also, the bow shock increases in initial curvature and location in the upstream region. Increasing the PR produces several notable effects on the downstream flow features. The bow shock is displaced further away from the injector surface and the angle of the linear portion of the bow shock increases slightly (from 29° to about 32°). The recompression shock angle (about 21°) appears to be almost a Mach line; however, the location of the shock does not seem to be influenced by the change in PR. As a result of the larger bow shock angle, the two shocks diverge further downstream. At the same downstream location, the separation distance between the shocks increases as PR increases. This result is due to the bowshock's

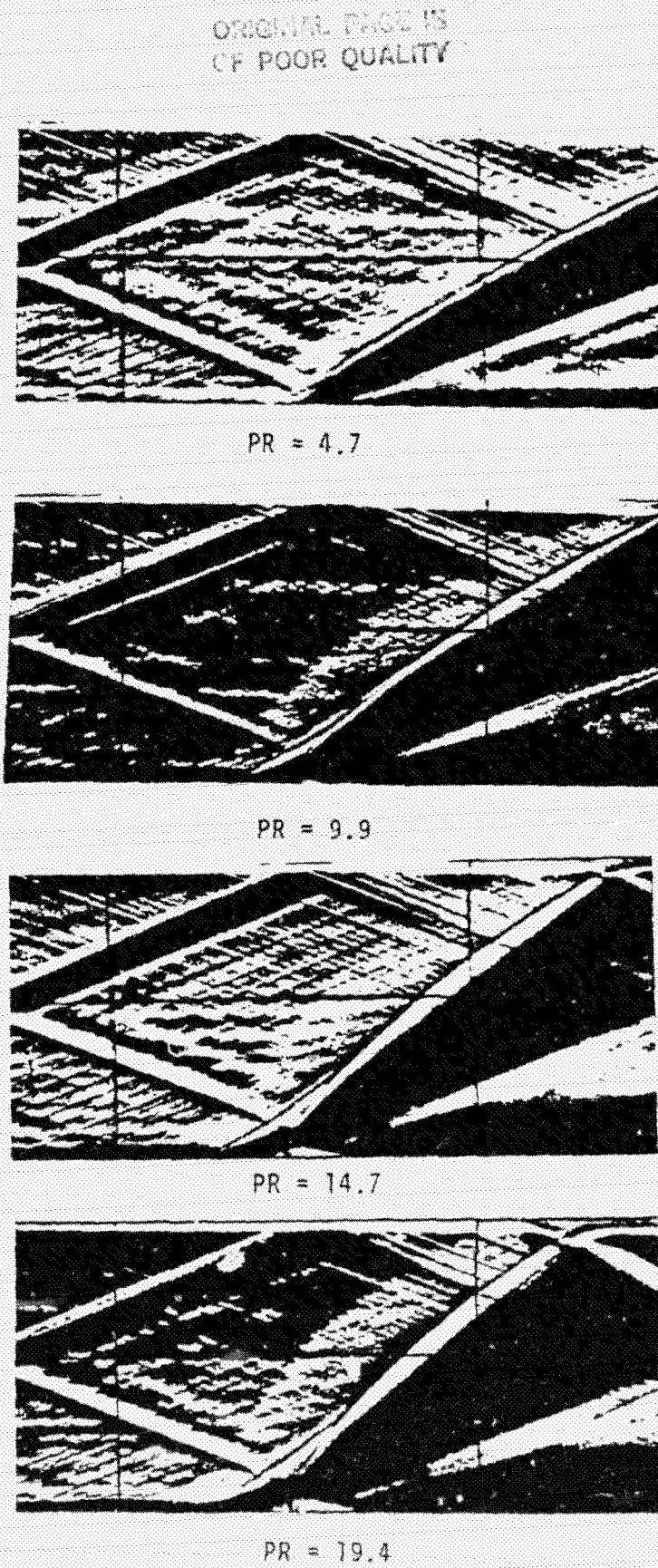


Fig. 6. Schlieren photographs for helium injection,
 $b = 0.043$ cm.

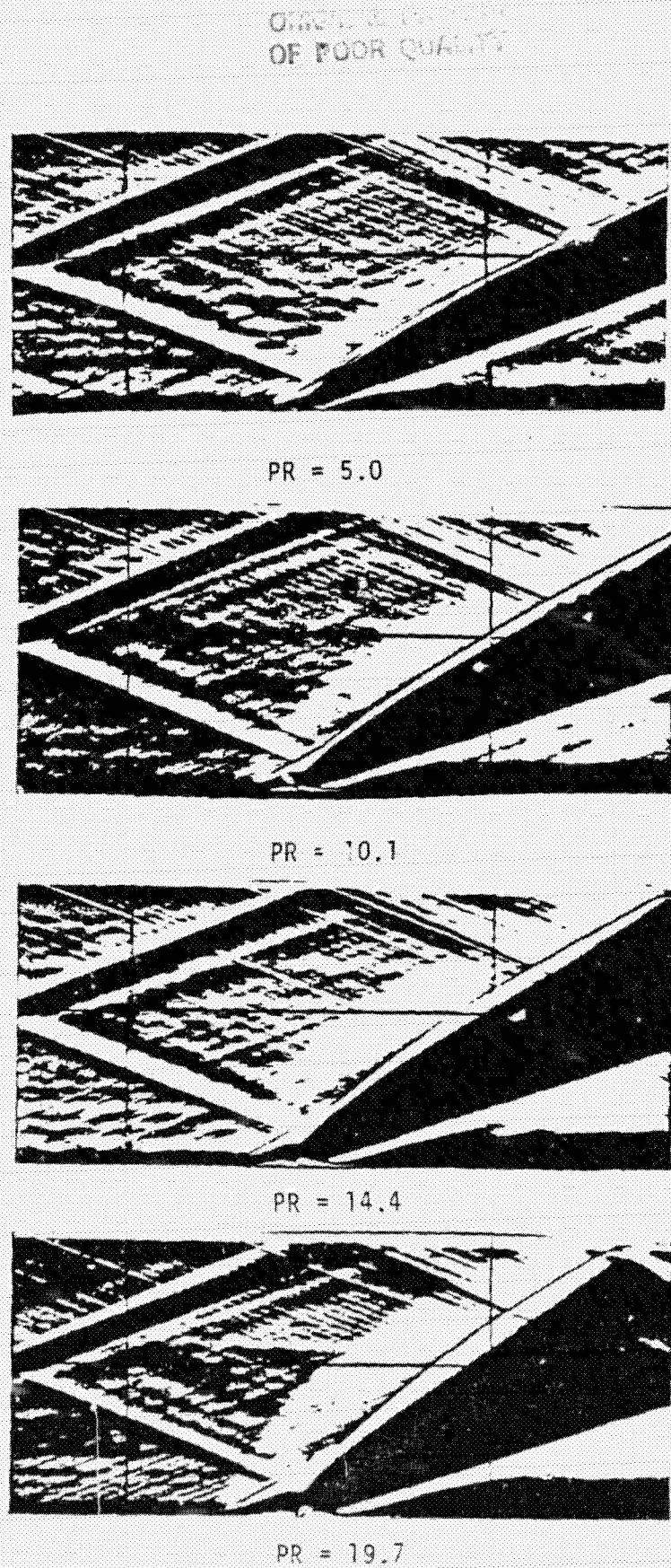


Fig. 7. Schlieren photographs for nitrogen injection,
 $b = 0.043 \text{ cm}$.

increased initial curvature and shock angle in the linear region. Similar results are observed for nitrogen injection in Fig. 7, although the flow field disturbance produced is smaller for nitrogen injection at the same PR.

Similar flow features were observed for air injection into an unconfined flow by Sterret and Barber [2]. For air injection, Werle et al. [10, 11] calculated a nearly constant separation shock turning angle (13.4°) at various jet strengths using an oblique shock wave theory. Thayer [1] observed that helium injection produced a larger disturbance than nitrogen injection at the same PR. These past investigations showed results similar to that noted in this study, although they were conducted for unconfined flow at higher values of PR.

4.2 Surface Pressure Distributions

The surface pressure distribution data is presented in Figs. 8 and 9. In each figure, the surface pressure is nondimensionalized by the surface pressure from the first surface tap (the value of which is given in Table 2), so as to account for possible changes in the tunnel supply conditions. As shown in Fig. 2, the right hand coordinate system is centered at the jet in such a way that the distance increases positively moving downstream from the jet. The surface location is nondimensionalized by the jet gap width.

Typical features for the surface pressure distributions are shown for a weak helium jet in Fig. 8a. Upstream the surface pressure increases from unity between about $x/b = -45$ to the first pressure plateau at $x/b \approx -28$. Closer to the jet, the surface pressure rises to a second plateau at $x/b \approx -5$. A low pressure

region extends from immediately downstream of the jet to a region of rapid pressure rise at $x/b \approx 12$. The surface pressure reaches a peak pressure at $x/b \approx 25$ and then slowly decreases approaching unity. These features are the result of the blockage and deflection of the supersonic mainstream by the jet expansion plume. The blockage of the flow is large enough to cause an adverse pressure gradient to separate the upstream boundary layer. The separation of the boundary layer results in the formation of a separation shock, a recirculation region, and a bow shock. The upstream surface pressure features are a consequence of the separation shock. Downstream of the jet, the rapid expansion of the flow over the jet plume causes a low pressure downstream recirculation region. Near the location of the reattachment of the boundary layer, the surface pressure rises to a peak pressure. Then, it slowly returns to a value near unity since the recompression shock lies upstream of where the boundary layer reattaches. Similar trends (and features) are noted for nitrogen injection in Fig. 8b, although the helium injection case produces a larger flow field disturbance.

Analogous results in surface pressure data were noted for helium and nitrogen injection for strong jet strengths in an unconfined flow [12]. These much stronger jets produced a larger more distinctive upstream second pressure plateau region, which was associated with separation of an upstream turbulent boundary layer [2], and is noted in results of this study because of the large mainstream Reynolds number (5.6×10^7 per meter) of the present investigation. Since analogous flow features were noted between the unconfined and confined flow data the empirical relations developed

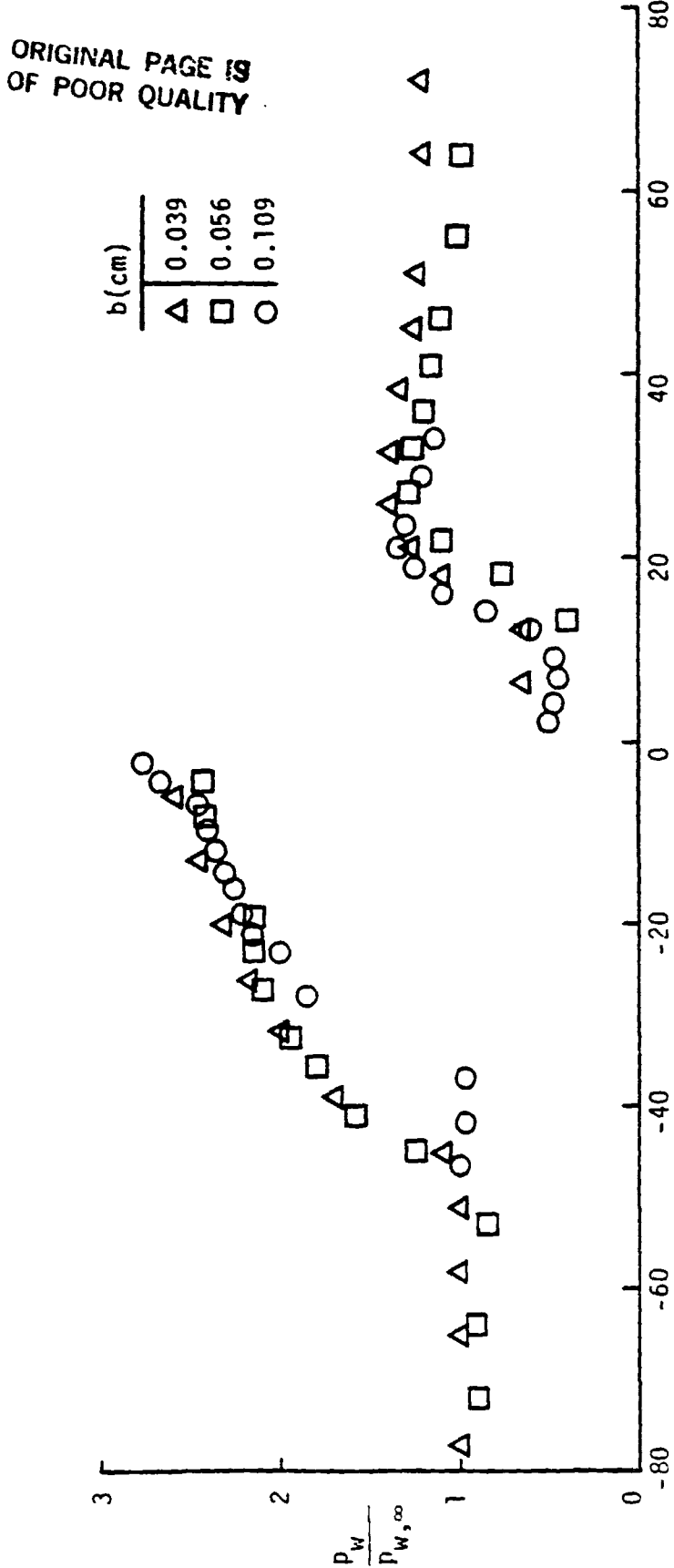


Fig. 8a. Surface pressure distribution correlation: PR = 10, helium injectant.

ORIGINAL PAGE IS
OF POOR QUALITY

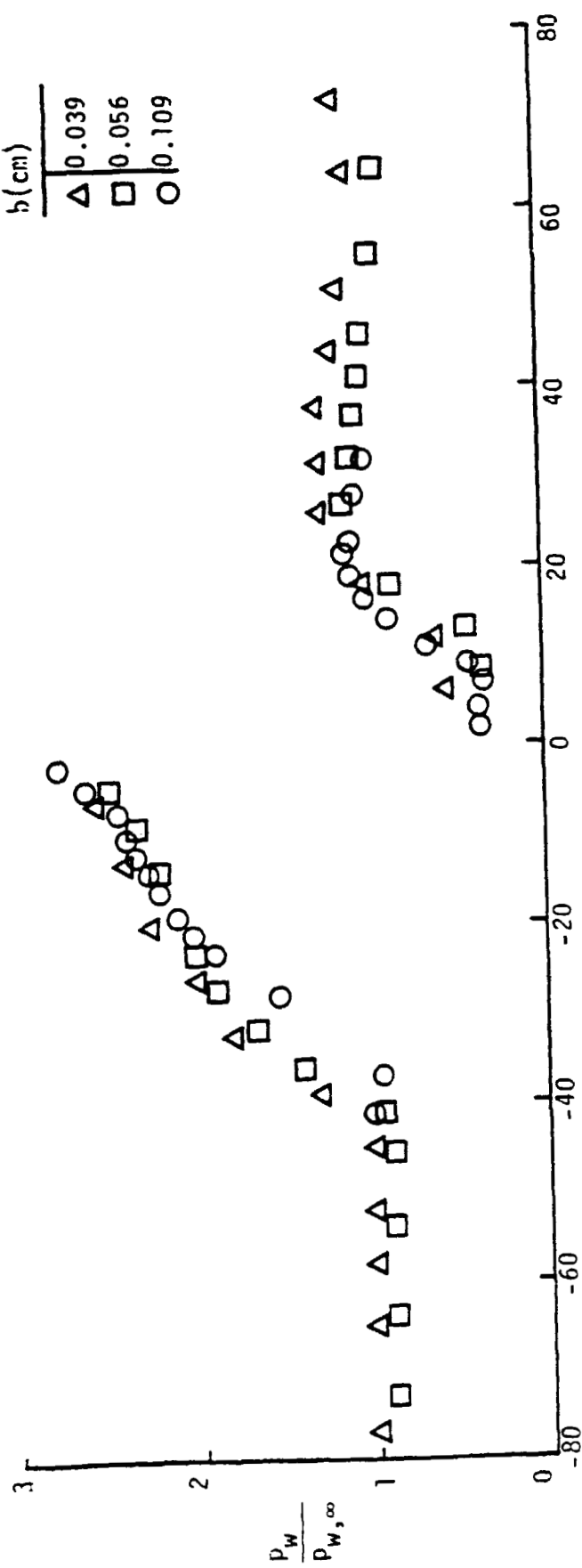


Fig. 8b. Surface pressure distribution correlation: PR = 10, nitrogen injectant.

ORIGINAL PAGE IS
OF POOR QUALITY

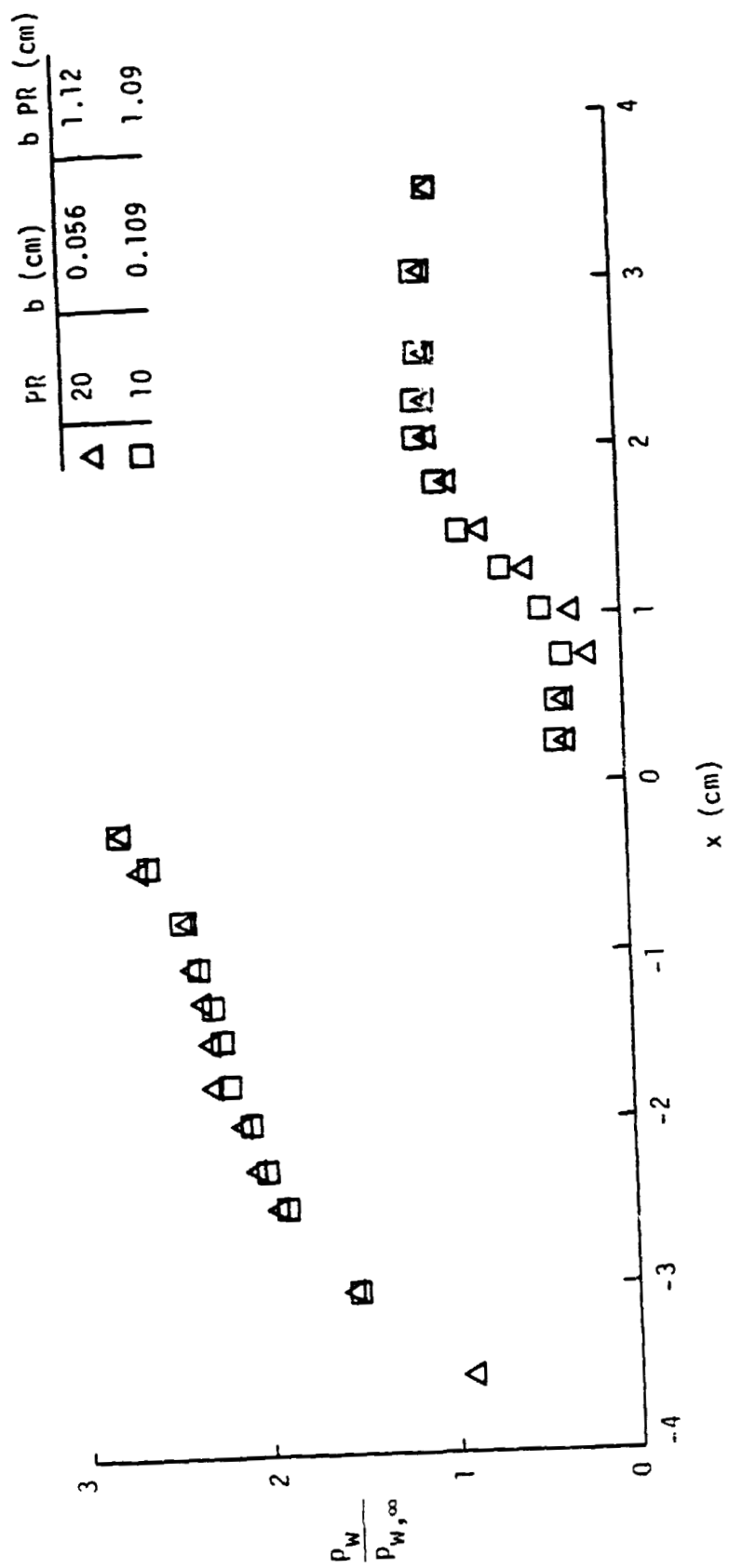


Fig. 8c. Surface pressure distribution correlation: $b_{PR} = 1.1 \text{ cm}$, nitrogen injectant.

for unconfined flows should be useful in examining also the results of this study.

Correlations of the surface pressure data are presented for a particular injectant species in Figs. 8. The effects of varying only the gap width on the surface pressure distributions are indicated for a helium jet in Fig. 8a. A good correlation of the data is found by scaling the surface locations by b . Therefore, a change in the size of b directly affects the size of the surface pressure distribution. For the largest b ($b = 0.109$ cm), the reduced locations of the upstream separation and downstream reattachment of the boundary layer may be due to three-dimensional effects. This effect is not so pronounced for the nitrogen injection case presented in Fig. 8b, for which the upstream separation distance is smaller. In spite of the early initiation of the upstream pressure rise for $b = 0.109$ cm, a good agreement is observed in the plateau region. Another good correlation is observed by comparing data at similar values of (b PR) in Fig. 8c for nitrogen injection. Notice, the surface locations are not scaled for this comparison. Similar trends were noted also in other results obtained in this study, since the sonic injectant flow out of the jet is for an adiabatic condition and ideal gas. Both methods for correlating the data are representative of the change in the jet momentum.

The effects of increasing the jet pressure on the surface pressure distribution are presented for a helium jet in Fig. 9a. The surface pressure disturbance increases with increasing PR. The surface pressure distribution features are not altered in general except for the presence of a second pressure plateau at about $x/b =$

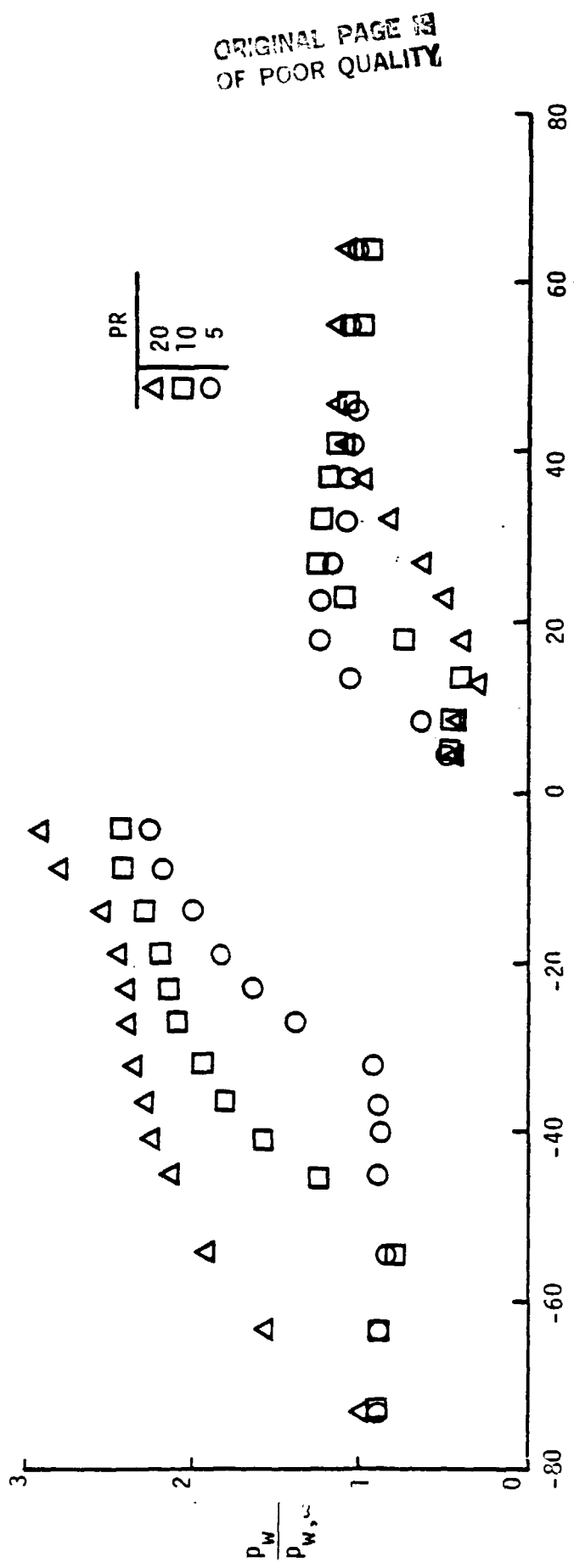


Fig. 9a. Effect of pressure on the surface pressure distribution, $b = 0.056 \text{ cm}$ helium injectant.

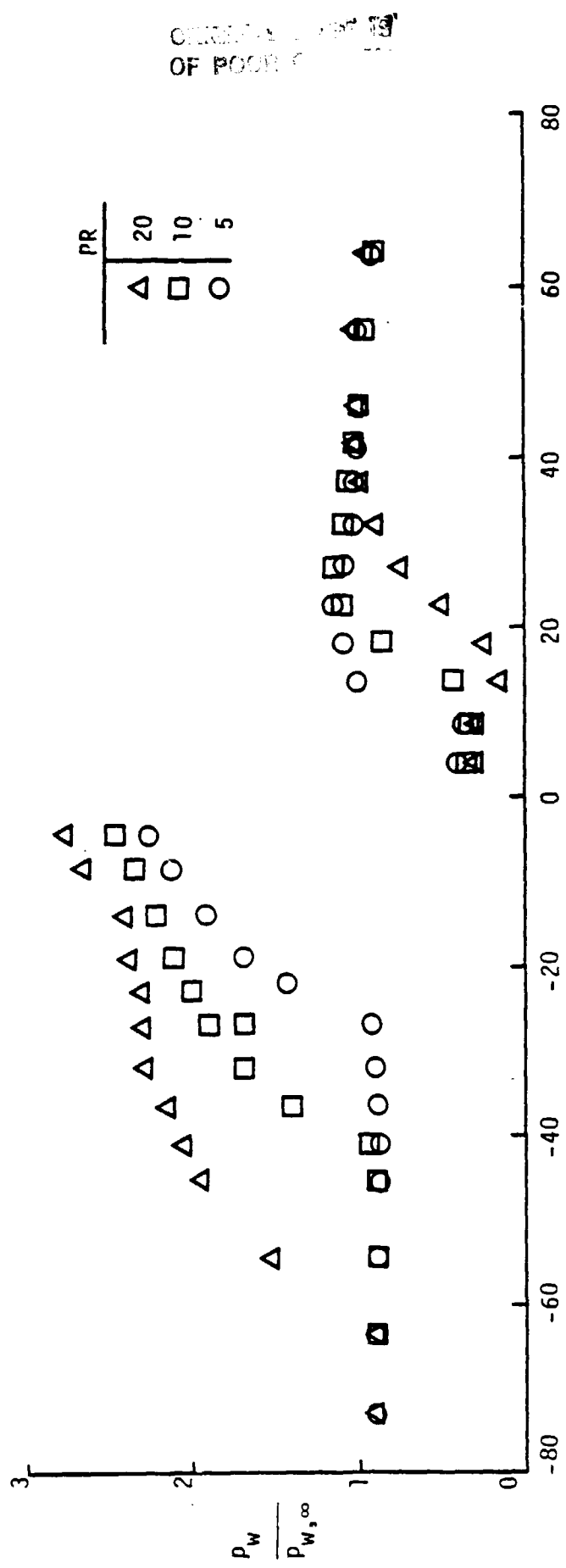


Fig. 9b. Effect of jet pressure on the surface pressure distribution, $b = 0.056$ cm; nitrogen injectant.

-10 for PR = 20. Figure 9b presents analogous data trends for nitrogen injection. As noted earlier, the disturbance is smaller for nitrogen injection.

It has been noted in previous investigations [12, 23] that the upstream pressure rise occurs before the actual separation of the turbulent boundary layer. Thayer [12] defined the separation distance as the location ($x_{1.5}$) at which $p_w/p_{w,\infty} = 1.5$. The same approach has been taken in this investigation due to the lack of a simple and accurate method of determining the actual point of separation.

In the past investigations for unconfined flows, $x_{1.5}$ was related to the jet parameters by a power law relationship and by a linear relationship. Thayer [12] correlated the dependence of $x_{1.5}$ on b and the jet strength. This is expressed by a power law relationship as

$$x_{1.5}/b = B \left(p_{t,j}/p_\infty \right)^C \quad (4.1)$$

where the quantity B is dependent on the injectant and free stream densities and free stream Reynolds number. The value of C was found to be 0.77 for helium, hydrogen, and nitrogen. A simple linear relationship was developed by Werle et al. [10] to express the jet shock height (h_s) in terms of the jet parameters and pressure acting about the jet plume (p_{plume}) as

$$h_s = 0.7 \gamma_j M_j b \left(p_j/p_\infty \right) / \left(p_{plume}/p_\infty \right) \quad (4.2)$$

where $p_{\text{plume}}/p_\infty$ is defined to be 2.8 (the second surface plateau pressure). This relationship can be expressed in terms of $x_{1.5}$ for this investigation as

$$x_{1.5} = 1.4 \gamma_j b PR \quad (4.3)$$

Both correlations were applied to the available data for $x_{1.5}$.

Correlations for $x_{1.5}$ with the jet parameters are presented in Fig 10. A separate least squares curve fit is shown for data from the largest gap width ($b = 0.109$ cm) due to the previously noted early separation. A good correlation is provided by the power law relationship as shown in Fig. 10a. The exponent for the data (0.67 for $b = 0.039$ and 0.056 cm, and 0.80 for $b = 0.109$ cm) is near the value determined by Thayer for Eq. (4.1). A better correlation is shown in Fig. 10b and is given by the linear relationship

$$x_{1.5}/b = B \gamma_j PR + C \quad (4.4)$$

The slope for the least squares fit of the data (1.5 for $b = 0.039$ and 0.056 cm, and 1.8 for $b = 0.109$ cm) is almost the value determined from Werle's relationship. For a constant width sonic jet, Eq. (4.4) relates $x_{1.5}$ to the relative change in jet momentum($\gamma_j b PR$).

Correlations of the surface pressure (p_w) distributions by $x_{1.5}$ are presented in Fig. 11 for $b = 0.056$ cm. Figure 11a presents the results of offsetting the surface locations by $x_{1.5}$ and shows that the surface pressure distributions are well correlated into a single

ORIGINAL PAGE IS
OF POOR QUALITY

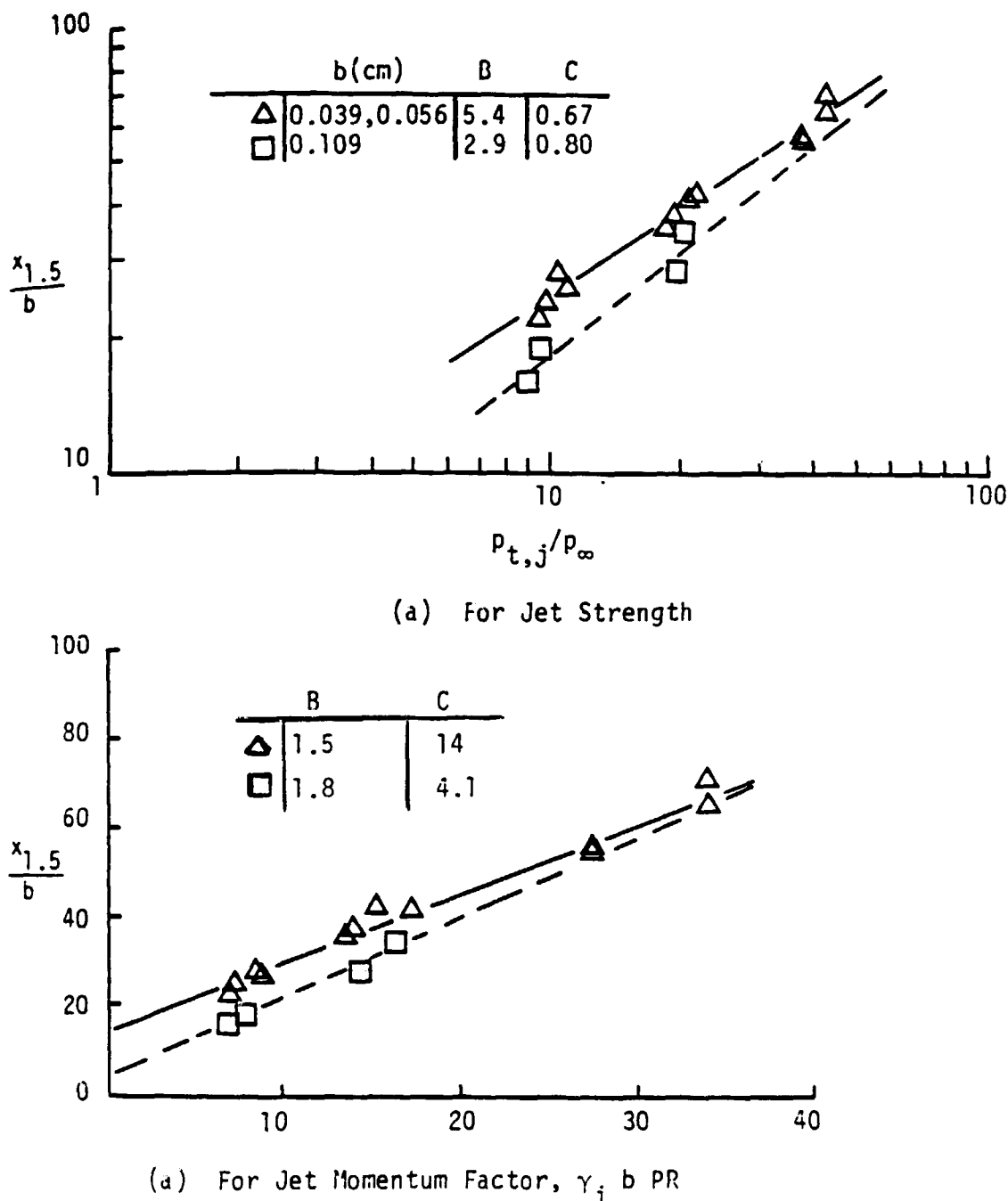


Fig. 10. Dependence of $x_{1.5}$ on the jet parameters for helium and nitrogen.

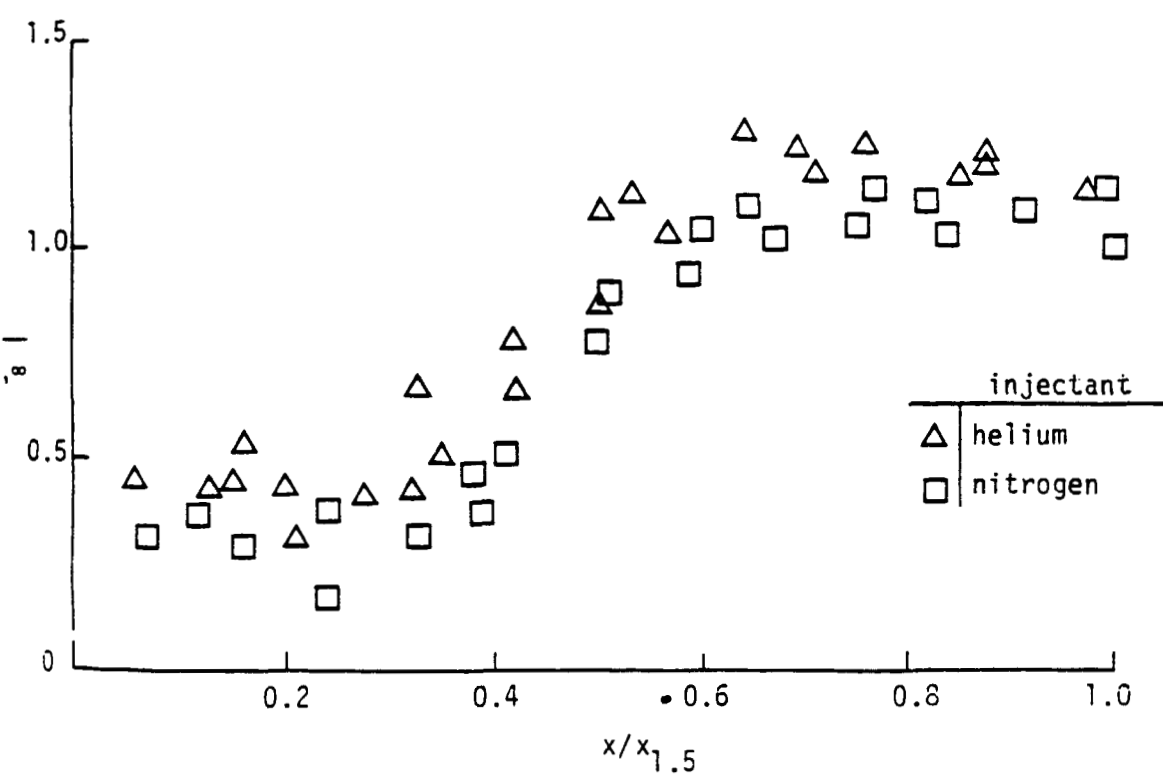
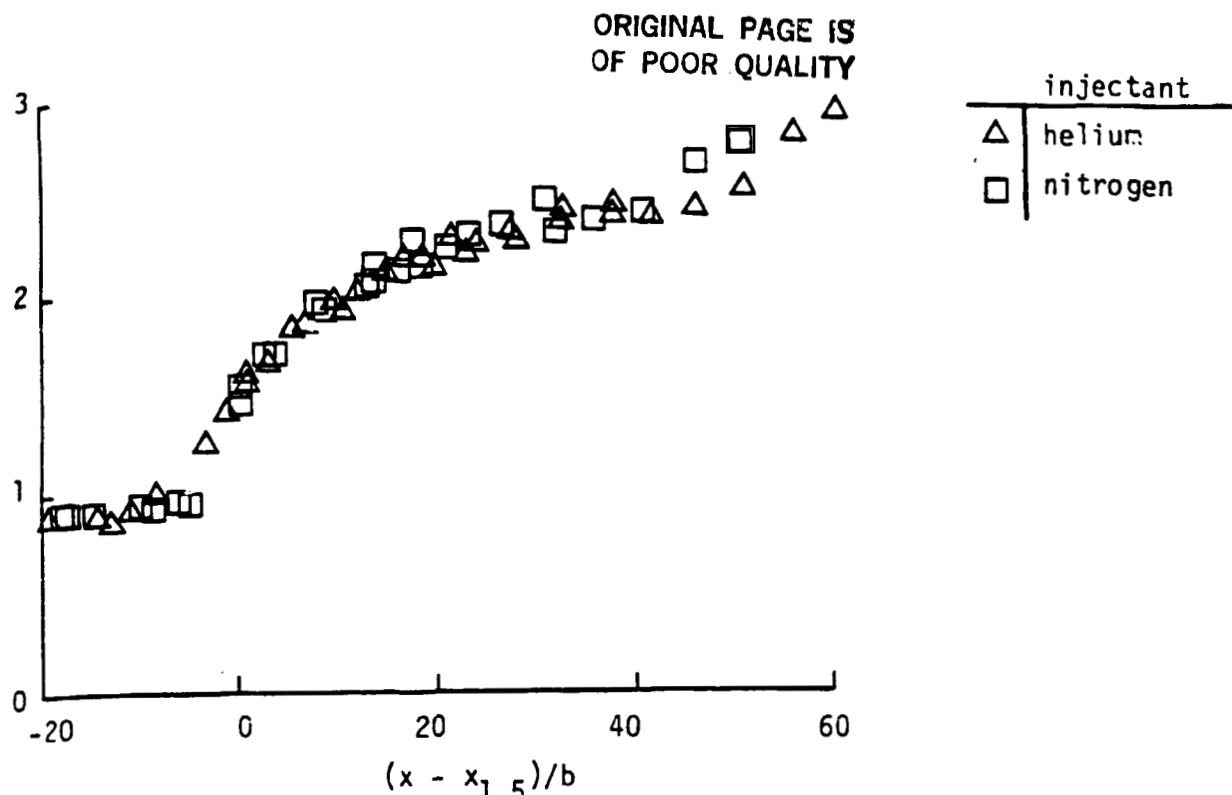


Fig. 11. Correlation of surface pressure distributions by $x_{1.5}$, $b = 0.056$ cm.

distribution by this method. A reasonable mean value for the first plateau pressure is observed to be $p_w/p_{w,\infty} \approx 2.4$ at $(x - x_{1.5})/b \approx 30$.

The second plateau pressure (about $p_w/p_{w,\infty} \approx 2.8$) is located at $(x - x_{1.5})/b \approx 55$. No dependence on the injectant species is noted in the figure. The downstream surface distributions rise from a region of fairly constant low pressure at $x/x_{1.5} \approx 0.37$ to a peak pressure at $x/x_{1.5} \approx 0.65$ (Fig. 11b). In general, the downstream pressure is slightly higher for helium injection. Also, the downstream scatter is not related to the jet pressure used. Some-what analogous results were found by Werle et al. [11] using the jet shock height; this air injection investigation exhibited a similar scatter in the downstream region. Thus, a good single distribution is obtained for either the upstream or downstream surface pressures based on $x_{1.5}$, which is related to the jet parameters (and jet momentum) by Eq. (4.3). This correlation may not be applicable to the case of large values of the gap width because of the early upstream separation.

The surface pressure features have been described and related to the jet parameters. The surface pressure disturbance is controlled by the relative jet momentum ($\gamma_j b PR$). A single upstream or downstream distribution is obtained by using $x_{1.5}$ to correlate the data. This quantity is found to be linearly dependent on the relative jet momentum. For a particular injectant species, the surface pressure data for various gap widths are related by scaling the surface location by b . Also, data compared at the same value of ($b PR$) are correlated well for unscaled locations. In general, the surface pressure disturbance increases with the relative jet

momentum.

4.3 Surface Mole Fraction Distributions

Surface injectant mole fraction (X_j) distributions are presented in Figs. 12 and 13. Samples of the gas mixture near the surface are collected through surface taps along the injection wall centerline. Typical features of the surface X_j distributions are shown for helium injection in Fig. 12a. The upstream injectant species spread extends ahead of the location of $x_{1.5}$ (i.e., $x/b = -60$). The value of X_j rises to a plateau at $x/b = -40$. Closer to the jet (at $x/b = -25$), X_j increases almost linearly. Downstream of the jet, a region of low concentration (and highly scattered data) extended to about $x/x_{1.5} = 0.35$ (i.e., $x/b = 18$). This is the location where the low downstream pressure region terminates. Then X_j increases rapidly to a peak value near the location associated with boundary layer reattachment at $x/x_{1.5} = 0.65$ (i.e., $x/b = 27$). A gradual decrease in concentration occurs further downstream. Analogous trends are noted for nitrogen injection in Fig. 12b; however, the local concentration is much smaller than for helium injection.

For this two-dimensional flow, it would be expected that a high concentration of injectant species would occur in the recirculation region downstream of the jet. However, this trend is not exhibited in the results presented in Figs. 12a and b. Entrained air or three-dimensional effects may account for the low concentration of injectant species in the recirculation region downstream of the jet. In this region, a large scatter in data is noted for different gap widths. Further downstream, however, the results compare favorably. Therefore, entrained air is probably the cause for the

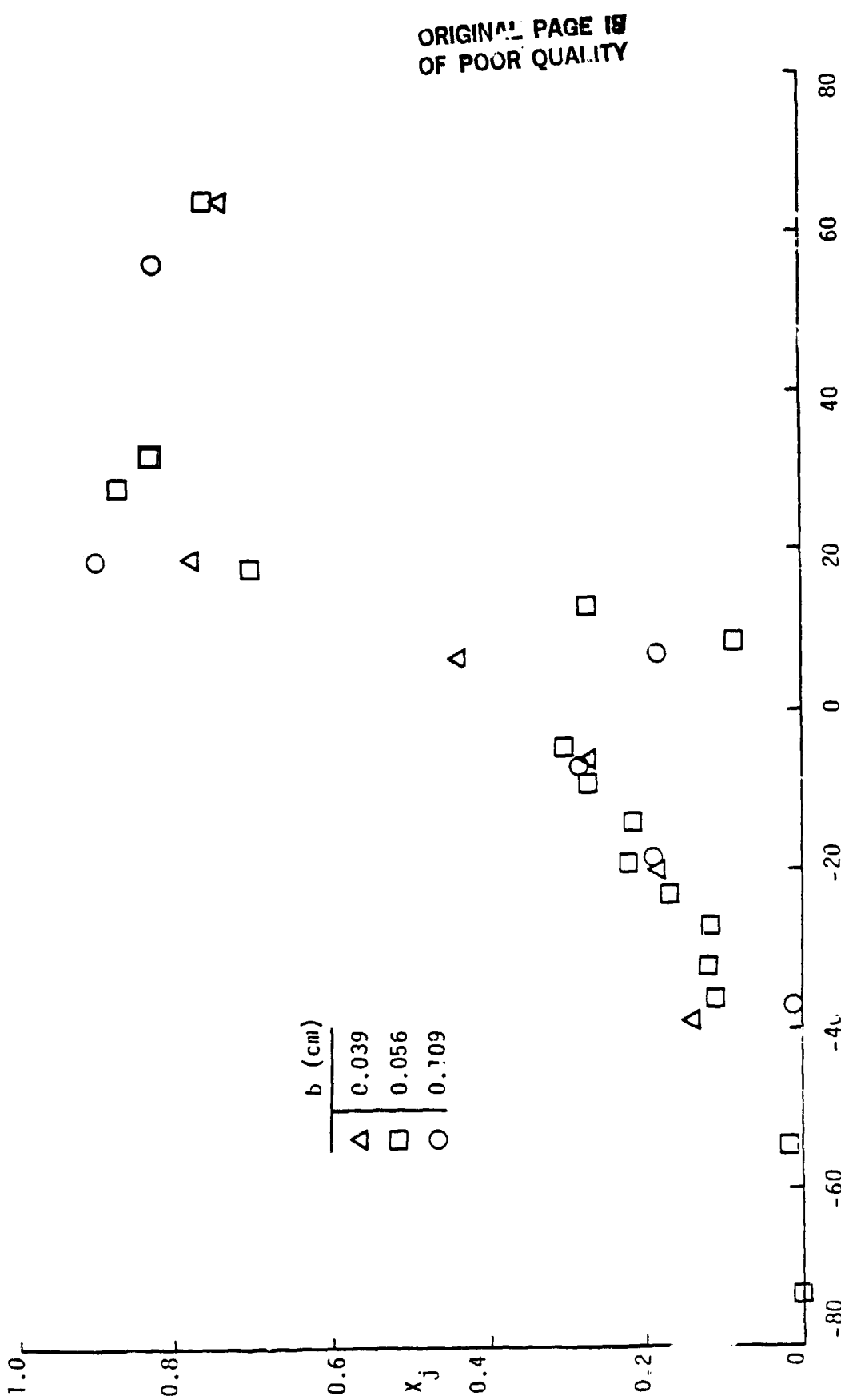


Fig. 12a. Injectant mole fraction surface distribution correlation: $PR = 10$, helium injected.

ORIGINAL PAGE IS
OF POOR QUALITY

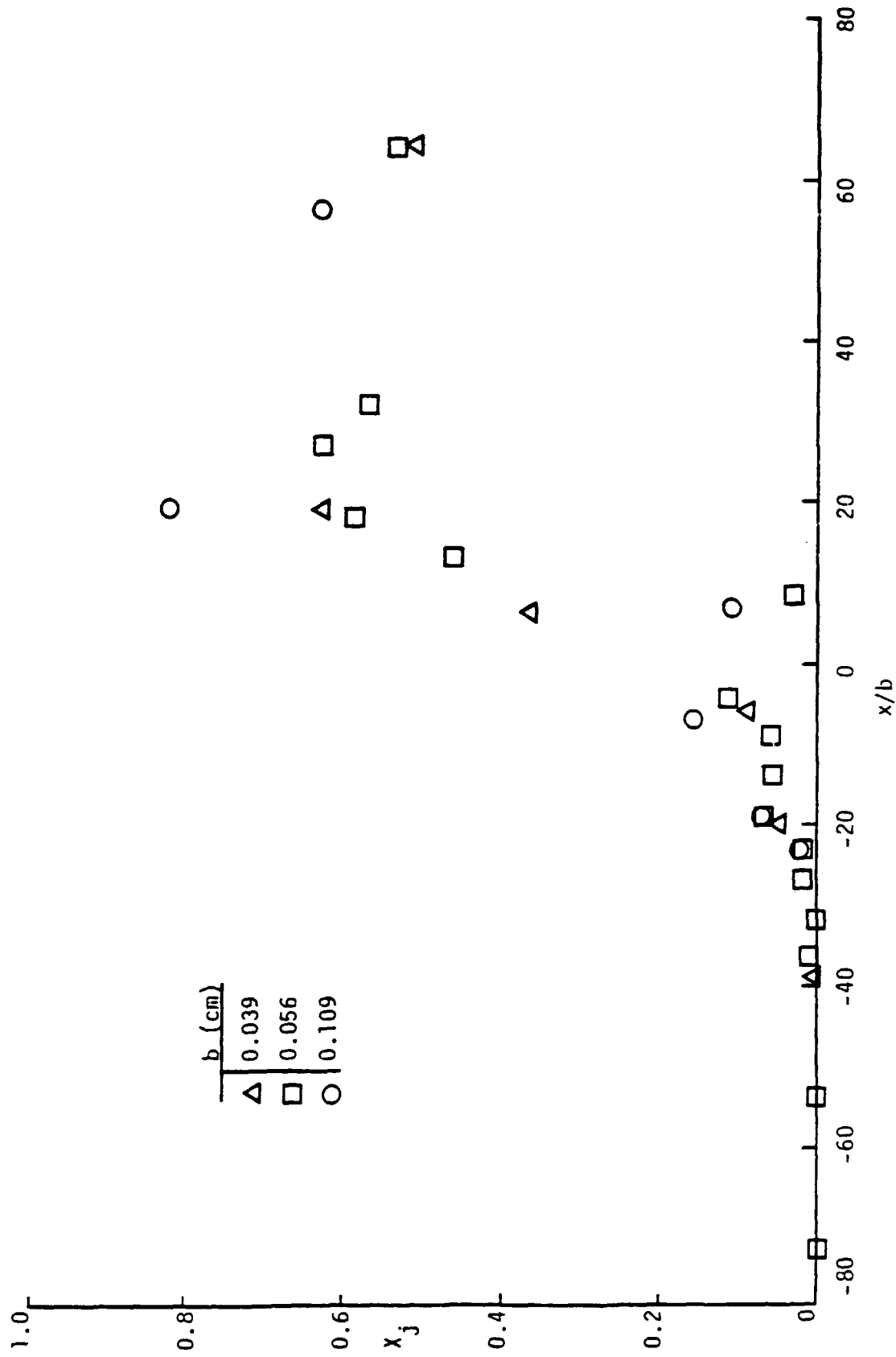


Fig. 12b. Injectant mole fraction surface distribution correlation: $PR = 10$, nitrogen injectant.

data scatter.

The results presented in Fig. 12 also provided a method for correlating the data for various values of b and PR. The effects of varying only the gap width on the surface distribution of X_j are presented for a helium jet in Fig. 12a and for a nitrogen jet in Fig. 12b. Both figures indicate good correlations of the data by scaling the surface locations by b . A good correlation is observed by comparing data at similar values of b PR in Fig. 12c for nitrogen injection. Note that the surface locations are not scaled for this comparison. Both methods of correlating the data demonstrate the direct dependence of the X_j distributions on the relative jet momentum. Unlike the surface pressure distributions, Figs. 12a and b show large differences in local values of X_j between the helium and nitrogen injection cases. As such, this would not allow a simple correlation of the composition data for different injectant species by the jet parameters.

The effects of doubling the jet pressure on the surface distributions of X_j are shown for a helium jet in Fig. 13a. The jet strength has only slight effects on the X_j distributions except for extending the regions of influence. The increased upstream recirculation region results in an increase in the upstream penetration of injectant. Boundary layer reattachment occurs further downstream of the jet as does the location of the maximum concentration. Figure 13b presents similar trends in the data for nitrogen injection. In these results a slightly larger value of X_j is seen throughout the upstream region for PR = 20. Again the helium concentrations at same x locations and jet conditions are much larger than the

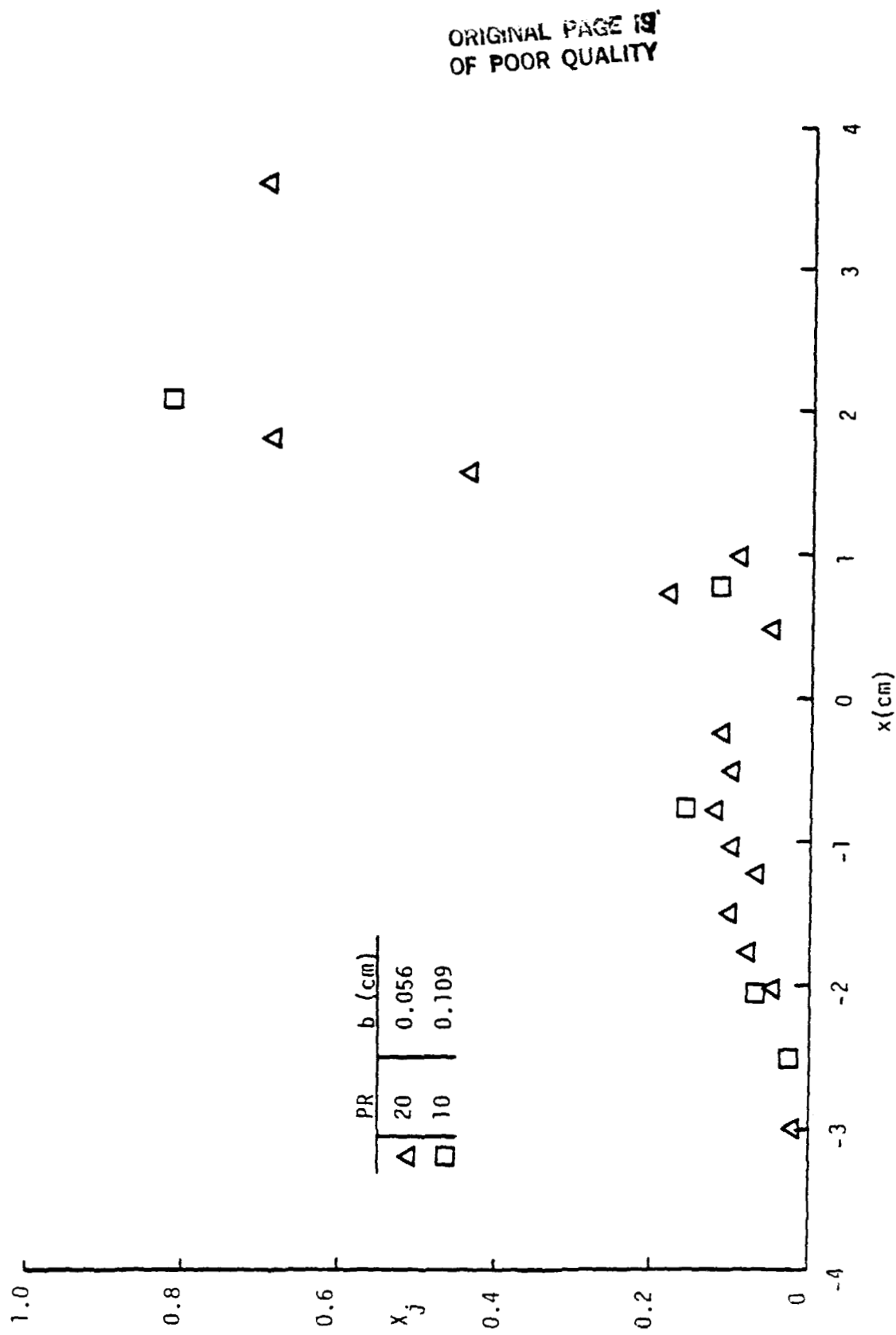


Fig. 12c. Injectant mole fraction surface distribution correlation: b $PR = 1.1$ cm,
nitrogen injectant.

ORIGINAL PAGE IS
OF POOR QUALITY

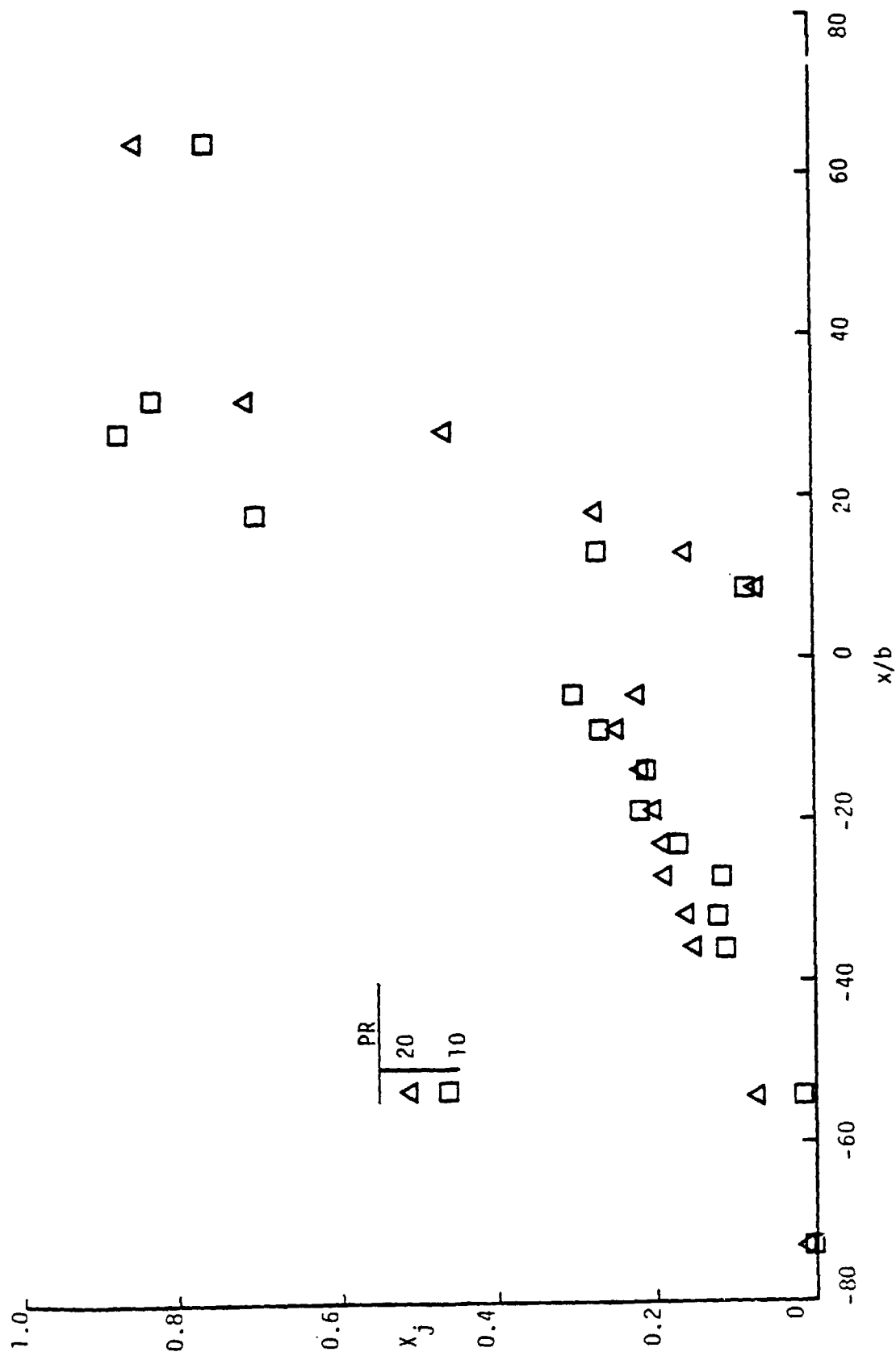


Fig. 13a. Effect of jet pressure on the surface mole fraction distribution, $b = 0.05$ cm;
helium injectant.

ORIGINAL PAGE IS
OF POOR QUALITY.

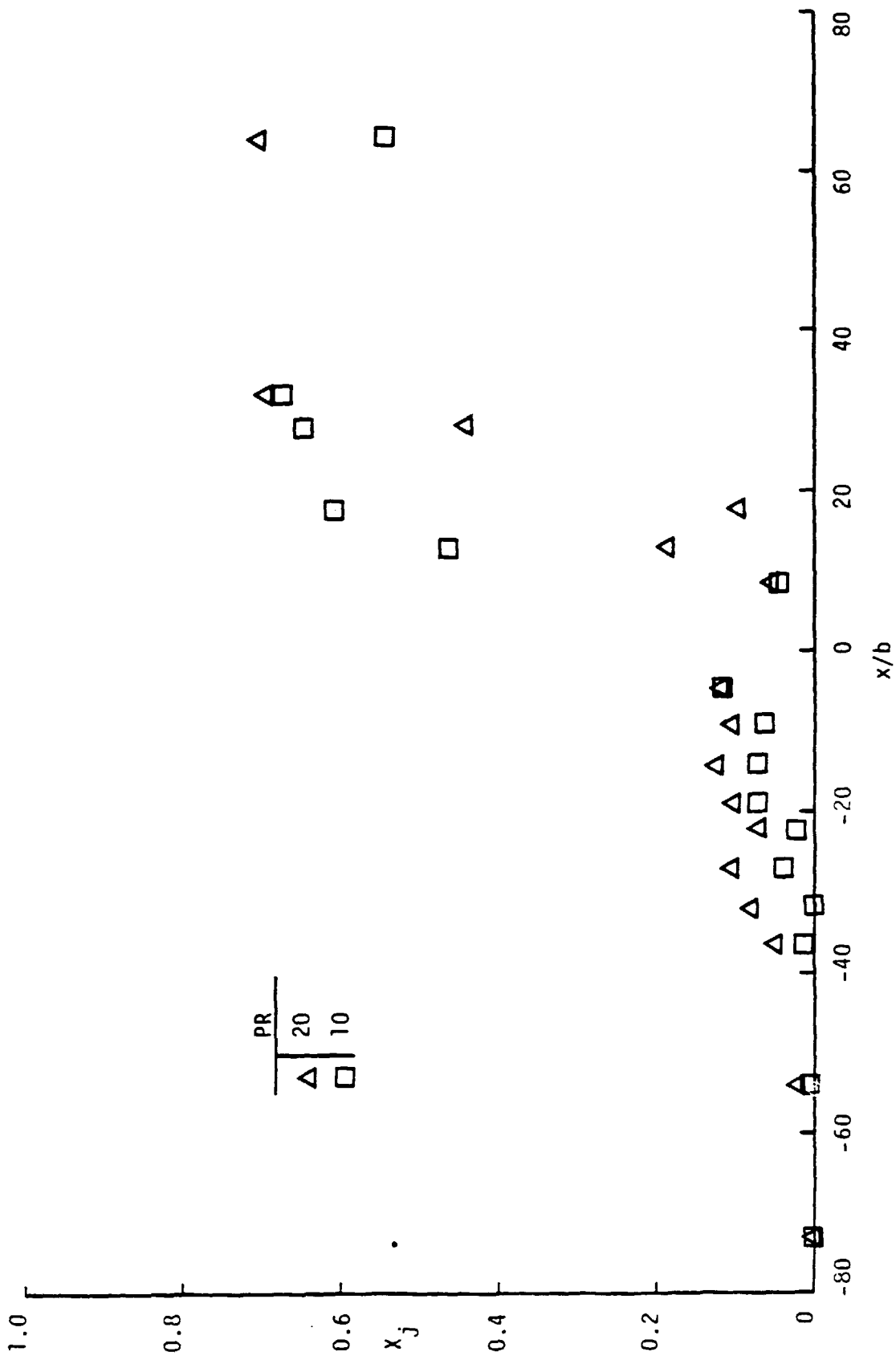


Fig. 13b. Effect of jet pressure on the surface mole fraction distribution, $b = 0.05$ cm;
nitrogen injectant.

nitrogen distributions.

The only other upstream surface X_j data reported in the published literature were for helium and nitrogen jets in unconfined flows for high jet strengths [12]. These results are significantly different from the findings of this investigation. These results indicate an upstream plateau region in which the concentration is nearly constant. Also, the plateau X_j values were over 40 percent larger in the previous investigation. The reason for the differences in the distribution data is assumed due to the much larger jet strengths and the different mainstream flow conditions used in the previous study.

The surface injectant mole fraction distributions have been described and related to the jet parameters. The surface distribution of X_j is shown to be controlled by the relative jet momentum for a particular injectant species. Therefore, the relative magnitude of b and PR determine the distribution of X_j along the surface. Surface X_j distributions could not be correlated reasonably by $x_{1.5}$. Doubling the jet strength produced only slight differences in the distributions except for extending the regions of influence.

4.4 Static and Pitot Pressure Profiles

Profiles of static pressure profile data from surveys of downstream flows are presented in Figs. 14-16; pitot pressures are nondimensionalized by the tunnel supply pressure (p_b), whose mean values are given in Table 3 for each test condition survey location. The individual values of the supply pressure never varied from the mean value by more than 0.5 percent. Surveys were made at the downstream locations of $x = 1.9, 3.8$, and 6.4 cm for $b = 0.056$ cm.

Also, surveys were made at $x = 2.8$ cm for $b = 0.039$ cm and at $x = 7.0$ cm for $b = 0.109$ cm. All of these surveys are made along the center line of the injection surface (i.e., $z = 0$).

Many features of the pressure profiles can be related to the visual observations of section 4.1 and downstream surface pressure distributions presented in section 4.2. As discussed in section 4.1, there is a strong downstream bow shock above a weak recompression shock. As such, the pressure would increase to a maximum at the bow shock and increase upon crossing the recompression shock. Recovery of the flow behind the recompression shock was indicated by the downstream surface pressures in section 4.2. The vertical distance between the two shocks increases for locations further downstream or for the same location with larger values of PR. The recompression shock location is not influenced by varying PR. Finally, the schlieren photographs and surface pressure data indicate that a larger disturbance is produced by helium injection than nitrogen injection.

Typical static pressure profile trends are presented in Fig. 14 for $PR = 10$ at $x/b \approx 70$. It is noted that for helium injection, the recompression shock occurs at about $y/b = 30$. Between the injection surface and the recompression shock, the static pressure recovers to the undisturbed mainstream value of $p/p_b = 0.032$ (for the Mach number flow of 2.9). Upon crossing the recompression shock, the static pressure decreases to a minimum value. Then it increases in a linear fashion to a maximum pressure at $y/b \approx 70$ (the location of the bow shock). Thus, the fairly linear pressure rise between the shocks indicates a region of large expansion fan. The relatively

broad region of maximum pressure is representative of the bow shock location. This effect is produced by the interaction of the bow shock with static pressure probe geometry (i.e., the 0.77 cm between the probe tip and pressure port). Above the bow shock the static pressure returns to the expected undisturbed value at $y/b \approx 81$. From oblique shock theory, the bow shock angle was calculated by using the static pressure values and was found to be 20° . Similar trends in results are noted for nitrogen injection. However, the locations of both the recompression shock and the bow shock are higher by $y/b \approx 7$ for helium injection. Their effects are relatively small. As such, the injectant species has a small effect on the static pressure variation.

For a particular injectant species, Figs. 14a and b present a method for correlating the data for various values of b and PR for either helium or nitrogen injection. A direct dependence is observed for the static pressure profile on the gap width in Fig. 14a for either injectant. A very good agreement is observed for data at similar values of $b \times PR$ and x -location in Fig. 14b for helium injection. Note that the vertical locations are unscaled in the figure. The shock locations are slightly elevated for $b = 0.109$ cm due to the different downstream profile locations (i.e., $x = 6.4$ cm for $b = 0.056$ cm and $x = 7.0$ cm for $b = 0.109$ cm). Analogous results are observed for nitrogen injection. Both methods of correlating the data demonstrate the direct dependence of the downstream static pressure disturbance on b and PR (i.e., the relative jet momentum).

Typical downstream development of the static pressure profiles

ORIGINAL PAGE IS
OF POOR QUALITY

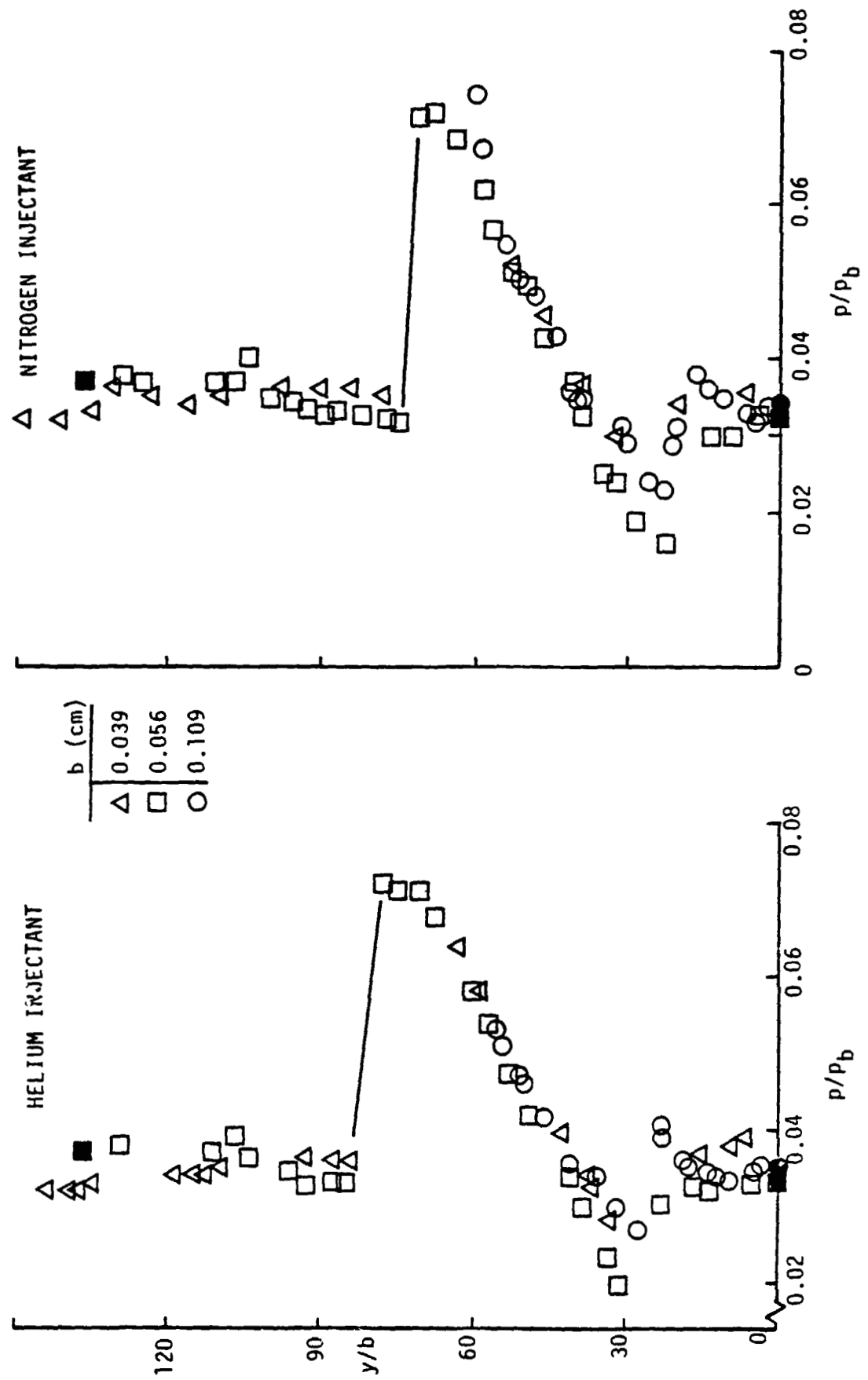


Fig. 14a. Nondimensional static pressure profile correlation: $PR = 10$, $x/b = 70$.

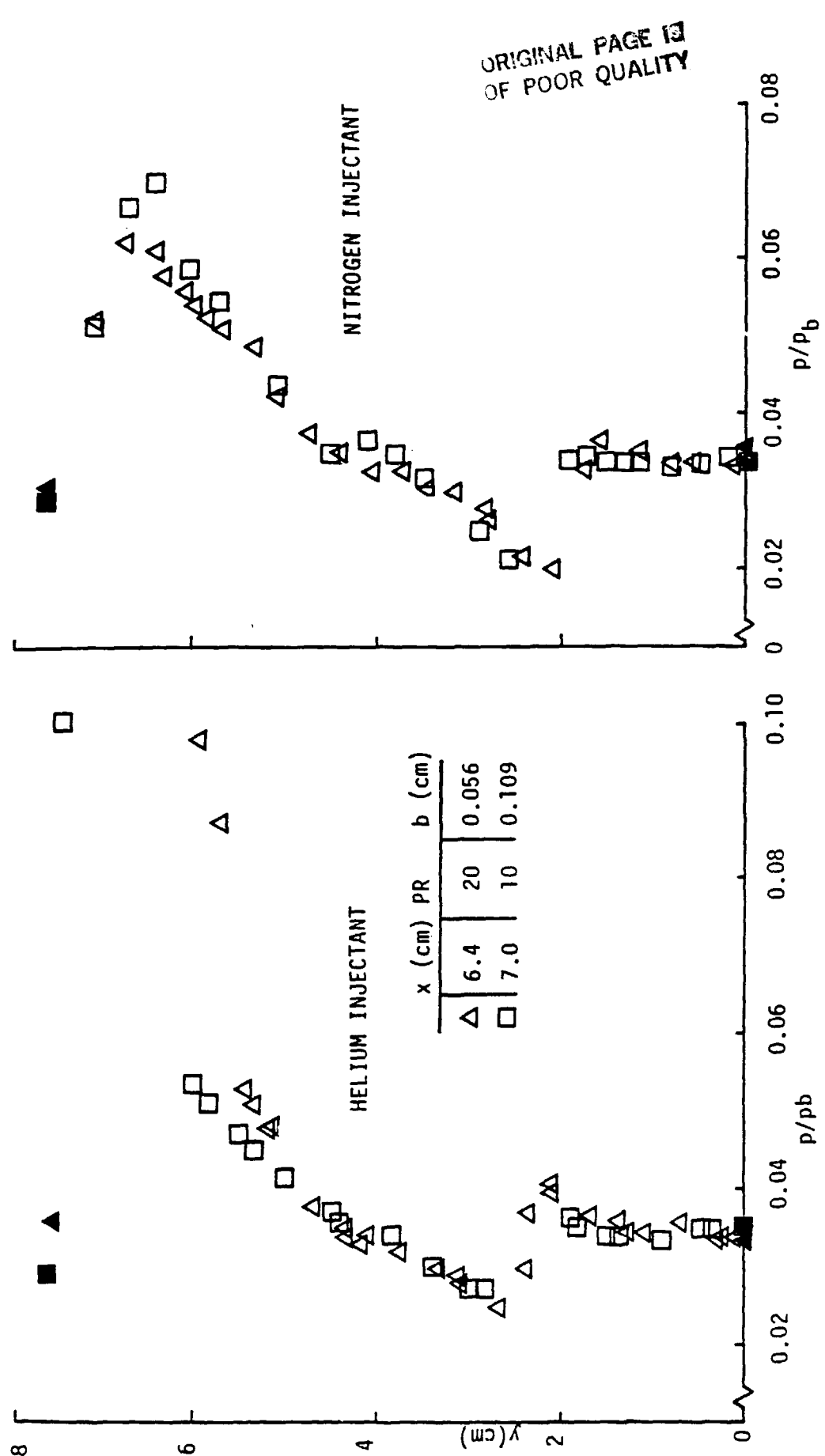


Fig. 14b. Nondimensional static pressure profile correlation: b PR = 1.1 cm.

are shown in Fig. 15 for $PR = 10$. For helium injection, the changes in pressure across the recompression shock and bow shock are reasonably independent of the downstream profile location. Therefore, almost constant shock turning angles would be obtained by oblique shock theory. The bow shock turning angle was found to be approximately 11° , and the recompression shock turning angle was between -6° and -8° . As a result, the two shocks diverge from one another further downstream. Also, the slope of the linear pressure rise increases from approximately 600 (at $x/b = 34$) to 900 (at $x/b = 114$). Analogous results are observed for the nitrogen injection case.

Typical effects of increasing PR are shown by the static pressure profiles at $x/b = 68$ in Fig. 16. The nominal values of PR used are 5, 10, and 20. For helium injection, the recompression shock is at a constant vertical location of $y/b = 30$. At this location, the pressure approaches a minimum value of $p/p_b = 0.018$ for $PR = 20$. In the region between the shocks, the slopes of the pressure rise are almost identical. The bow shock location and shock strength increases with PR. For increasing values of PR, the bow shock turning angles were found to be 9° , 11° , and 13° . Note that the static pressure data from different profiles agree very well after the bow shock locations. Therefore, the flow beyond the shock is not affected significantly by the flow field disturbance produced by the jet. Analogous results are observed for nitrogen injection. The slope of the linear pressure rise between the shocks had a mean value of 820 with a variance of less than 12 percent. This variance is independent of the injectant species.

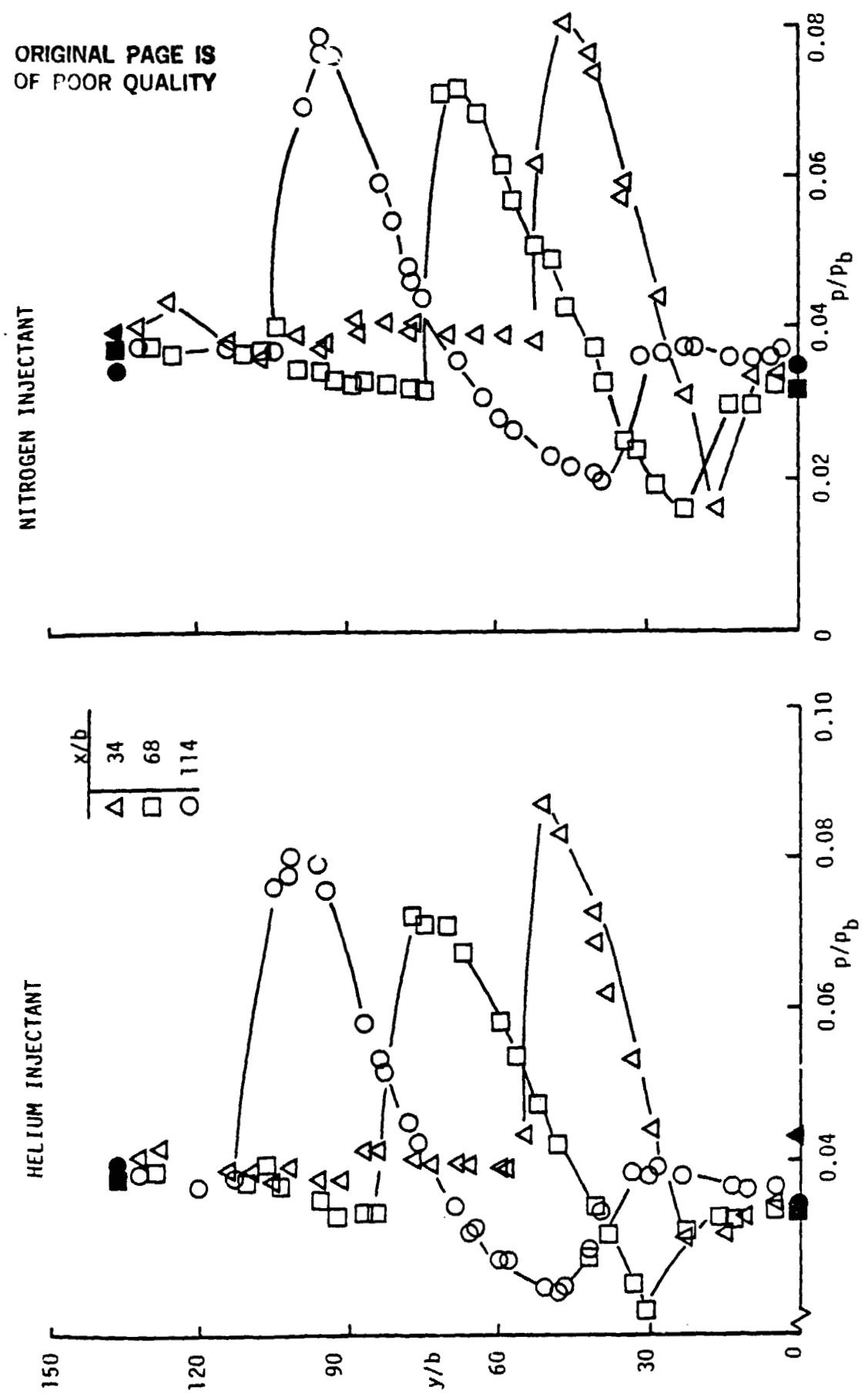


Fig. 15. Effect of downstream location on the static pressure profiles, $PR = 10$, $b = 0.056$ cm.

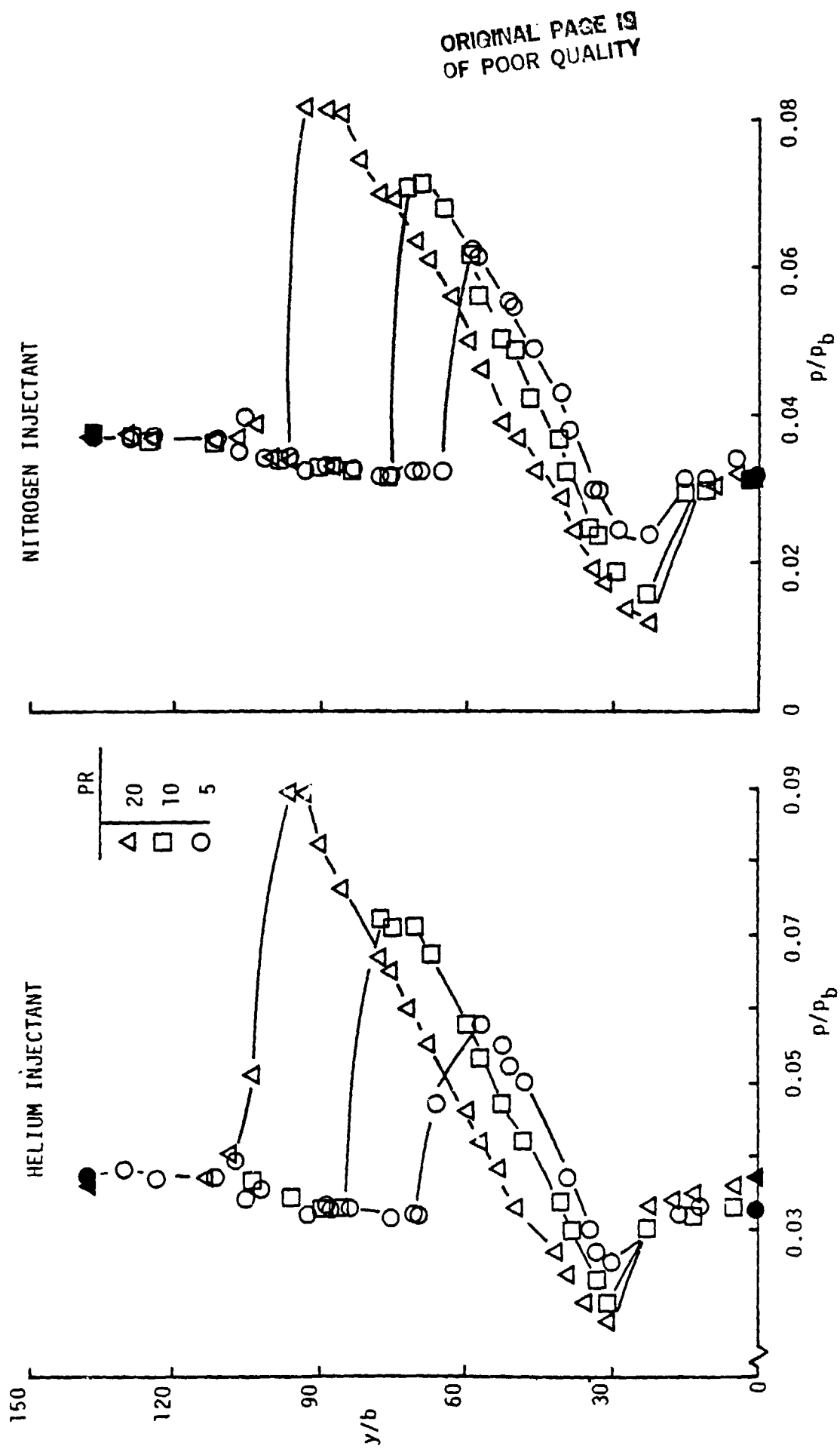


Fig. 16. Effect of jet pressure on the static pressure profiles, $x/b = 68$, $b = 0.05 \text{ cm}$.

In general, the static pressure profiles are almost independent of the injectant species. The two notable exceptions, however, are the higher recompression shock and bow shock locations and the lower minimum pressure associated with the recompression shock for helium injection. Below the recompression shock and above the bow shock, the static pressure is approximately the value expected in the undisturbed mainstream. However, a nearly linear rise in static pressure occurs from the minimum value at the recompression shock to a maximum value at the bow shock location. This phenomenon is probably the result of a region with a large downstream expansion fan.

The distance between the two shocks increases with the value of b and PR and with downstream location, although the shock angles are apparently independent of the downstream after $x/b = 34$. For a particular injectant species, the downstream static pressure disturbance is directly related to the change in b and PR (i.e., the relative jet momentum). The data exhibit only a slight dependence on the injectant species; therefore, a simple correlation of the data for either injectant species could not be formulated based on the jet momentum.

The pitot pressure profiles are presented in Figs. 17-19. These data are for jet conditions and downstream locations analogous to those presented in the static pressure profiles. Therefore, analogous results would be expected for the same downstream locations except in the boundary layer region.

The typical trends in the pitot pressure profiles are shown in Fig. 17a for helium and nitrogen injection. These trends are very similar to those discussed previously for the static pressure

profiles including the linear pressure rise between the shocks. A notable exception is in the boundary layer regions. The solid symbols indicate the surface pressure. On the wall opposite the jet the boundary layer has a thickness of less than 0.03 cm. Similar values of the boundary layer thickness were calculated using the one-seventh power velocity distribution law [24]. The injection wall boundary layer is indicated by the rapid pressure rise from the surface to a constant value of approximately $p_t/p_b = 0.36$, which corresponds to the pitot pressure in the undisturbed mainstream. The boundary layer extends to about $y/b = 20$ for helium injection and to $y/b = 13$ for nitrogen injection. Thus, the boundary layer thickness is increased for helium injection by $y/b = 7$ (a similar increase was noted for the shock locations). For helium injection, the minimum and maximum pitot pressures are increased by $p_t/p_b = 0.03$. Note that the bow shock region is not broadened in the pitot pressure profiles; this effect may be attributed to the bow shock interaction with the probe geometry.

As previously discussed, the direct dependence of the downstream pressure field on the changes in b and PR is shown by the pitot pressure profile comparisons in Fig. 17a for various values of b and in Fig. 17b for various values of b PR. For a particular injectant species, the good correlation of the data represents its direct dependence on the change in the relative jet momentum.

Typical downstream development of the pitot pressure profiles is presented for $PR = 7.0$ in Fig. 18. For helium injection, the boundary layer thickness does not increase significantly further downstream. The change in pressure upon crossing either shock is

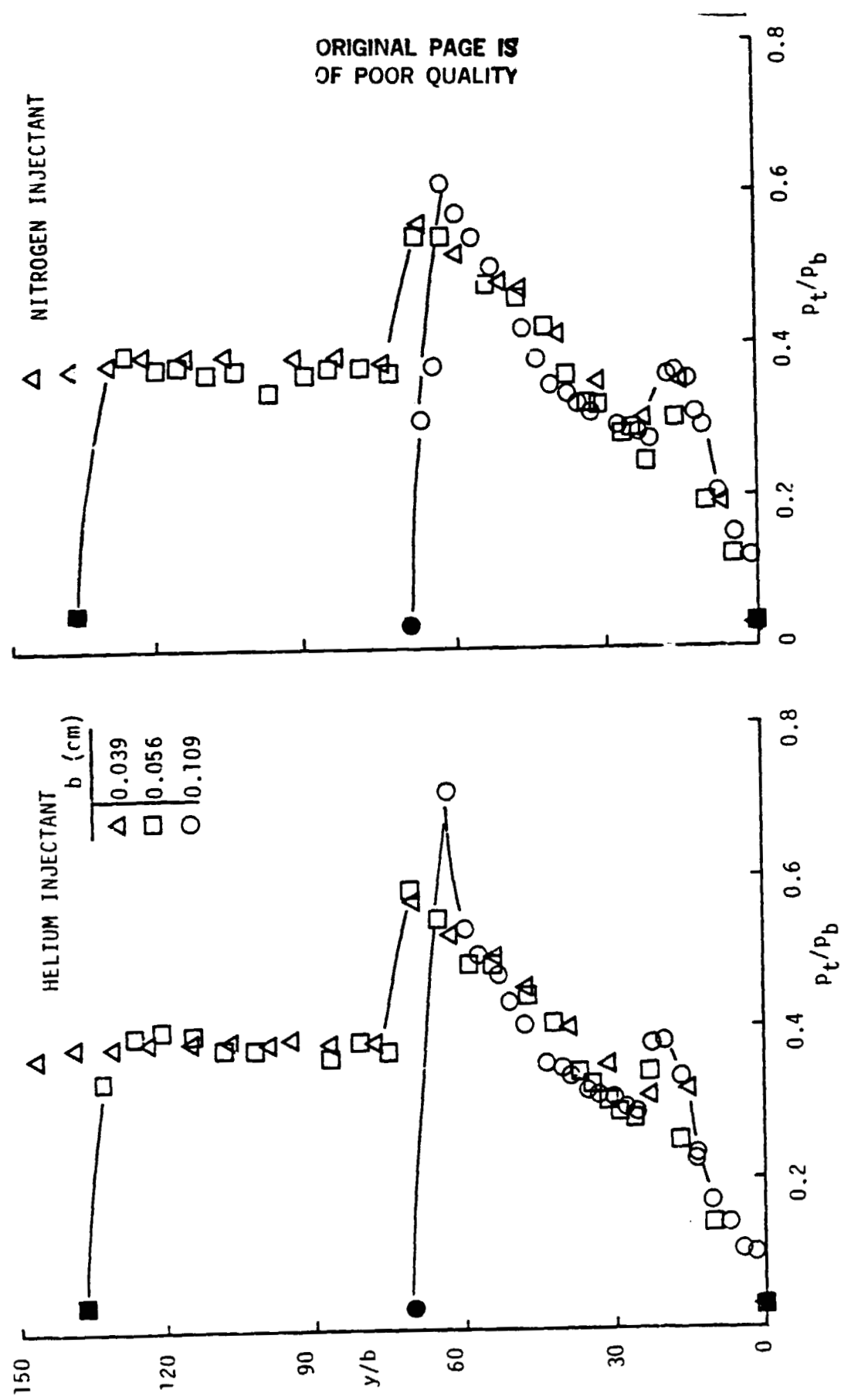


Fig. 17a. Nondimensional pitot pressure profile correlation: $PR = 10$, $x/b = 68$.

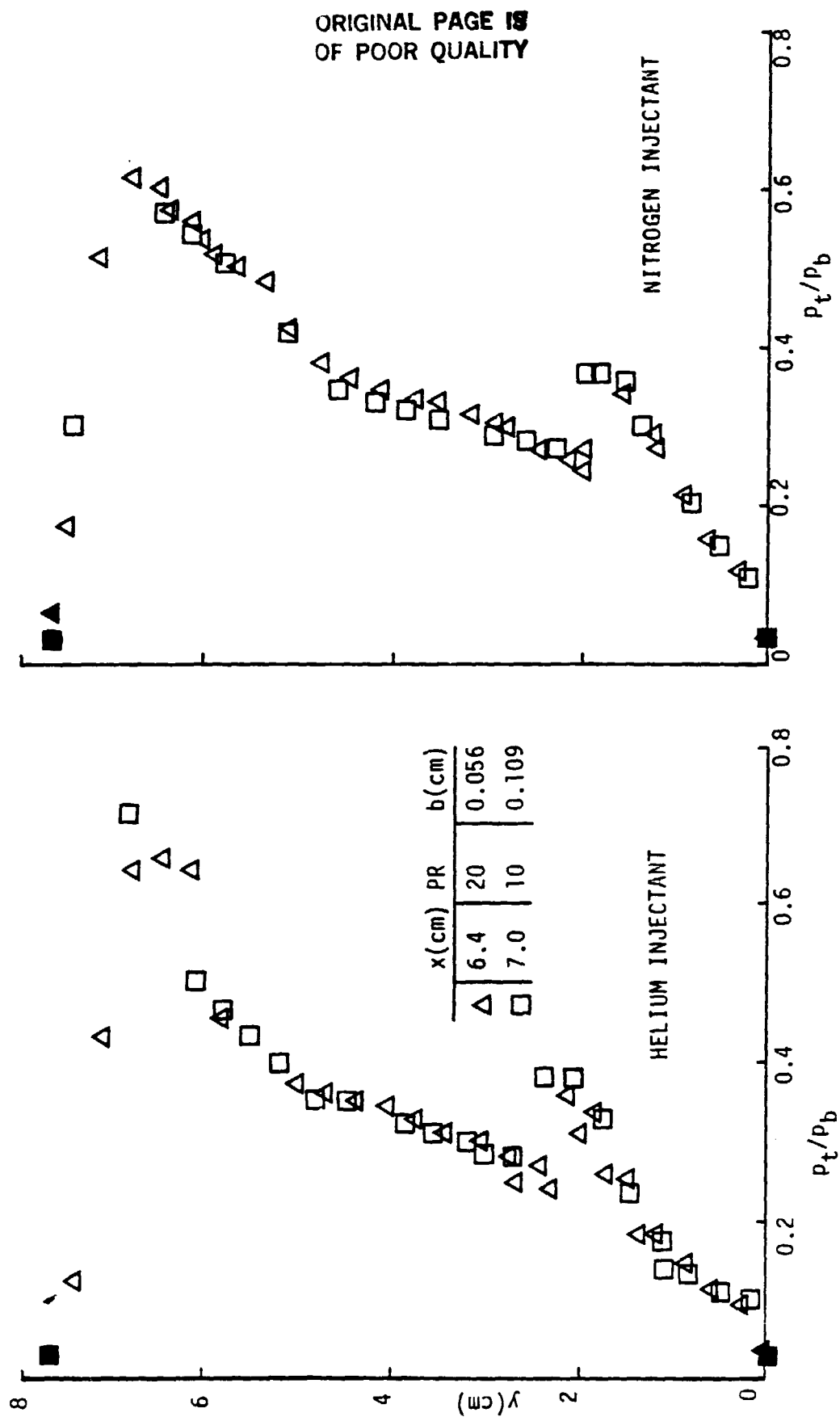


Fig. 17b. Nondimensional pitot pressure profile correlation: b PR = 1.1 cm.

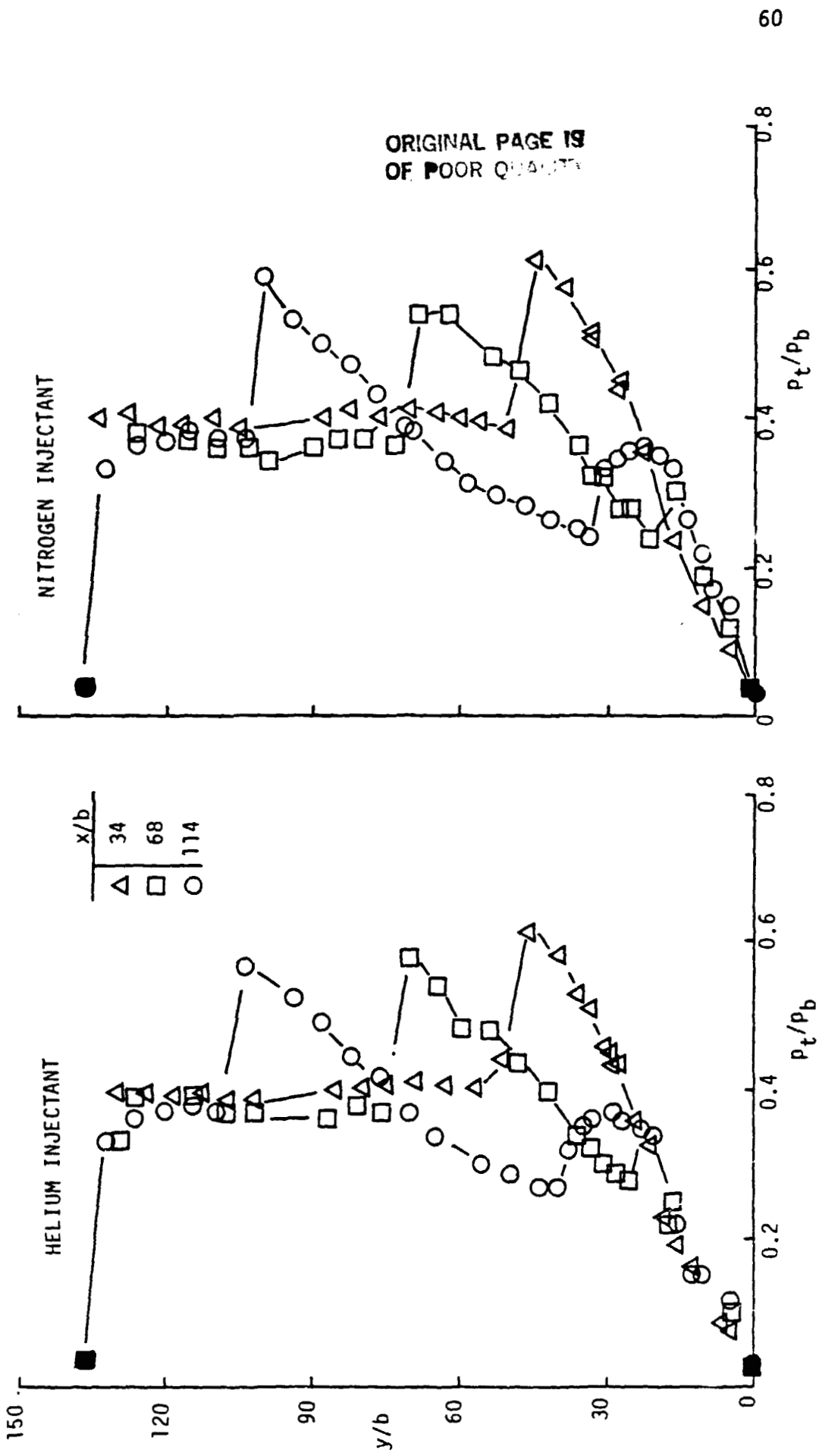


Fig. 18. Effect of downstream location on pitot pressure profiles, $PR = 10$, $b = 0.056$ cm.

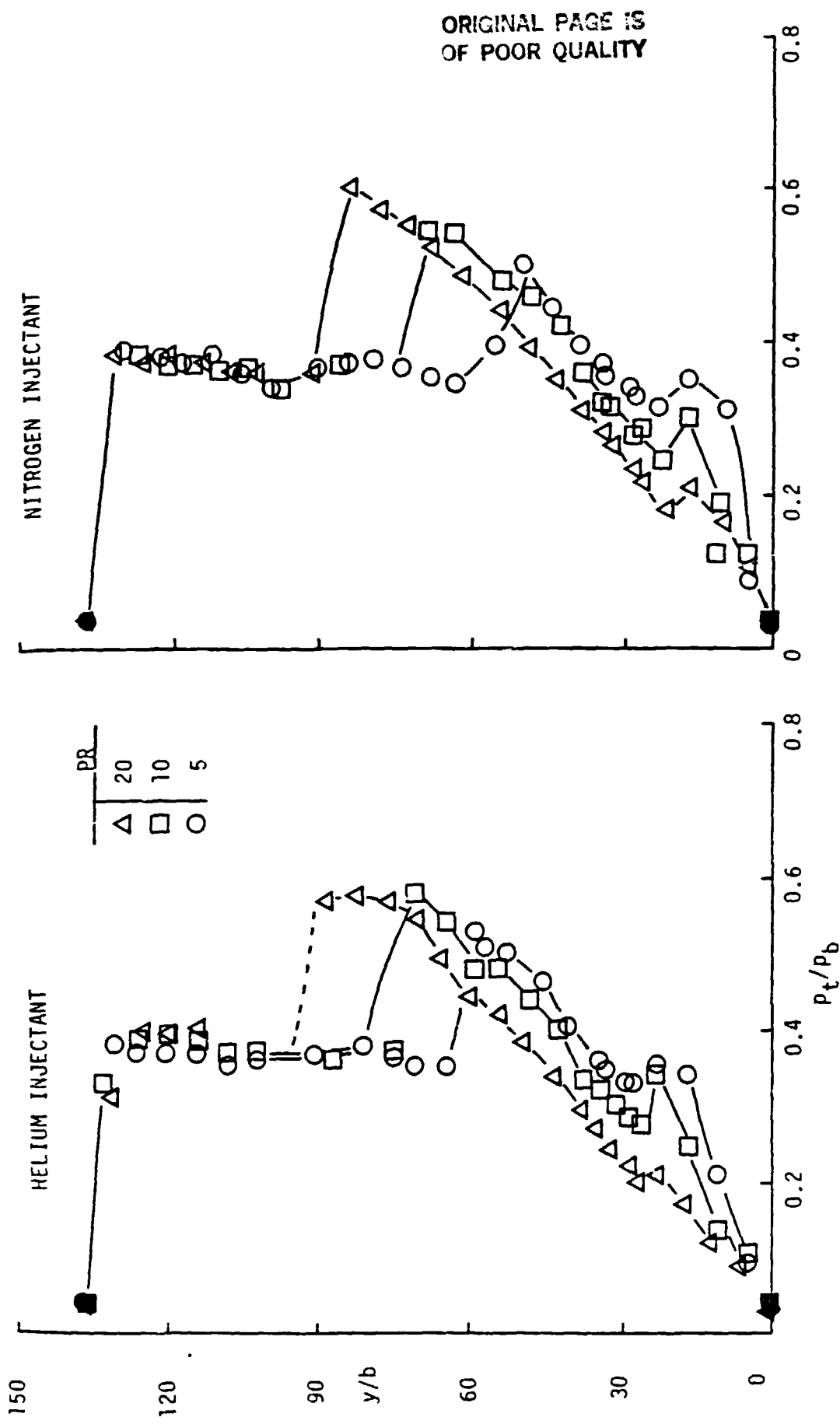


Fig. 19. Effect of jet pressure on the pitot pressure profiles, $x/b = 68$, $b = 0.056$ cm.

independent of the downstream location. Similar results are noted for the nitrogen injection data.

Typical effects of increasing PR on the pitot pressure profiles are shown at one downstream location ($x/b = 68$) in Fig. 19. From the helium injection profiles, the boundary layer thickness increases with PR. The other effects on the data trends were discussed earlier for the static pressure data. Analogous results are observed in the pitot pressure data for nitrogen injection.

Results presented in this section show an analogous trend in static and pitot pressure data. However, there is one exception, the boundary-layer region indicated in the pitot pressure data. The boundary layers thickness increases with PR, but not significantly with the downstream location along the injection surface. From both the static and pitot pressure data correlations, it is noted that the downstream pressure field disturbance is directly related to the changes in relative jet momentum for a particular injectant species. Also, the disturbance is slightly increased for helium injection.

4.5 Mole Fraction Profiles

The trend in injectant mole fraction (X_j) profiles is shown in Figs. 20-22 for different downstream locations and jet conditions. The X_j data was determined from gas samples collected by the pitot probes. The X_j values less than 0.02 should be considered pure air, since the analyzer error was about two percent. To aid in examining the data trends, the vertical axis (i.e., the y-location) is expanded three-fold larger than used for pressure profiles. However, the distance between X_j values is less than 0.3 cm (diameter of pitot probe body). The X_j data presented are for the

same downstream locations (and jet conditions) are used in the pressure profile figures.

Typical trends in the X_j profiles are presented in Fig. 20a. For helium injection, the injectant mole fraction decreases from a maximum at the surface. The X_j profile resembles one side of a Gaussian distribution curve. A reasonable exponential least squares fit was found for this data, as discussed later in this section. The injectant is seen to penetrate the flow to about $y/b = 18$. For nitrogen injection, the values of X_j are smaller and penetration distance extends to $y/b = 15$.

For a particular injectant species, Figs. 20a and b present a method for correlating the data for various values of b and PR. As with pressure profile data, the X_j profile data are directly affected by the changes in b (Fig. 20a) and b PR (Fig. 20b). Also, these methods of correlating the data are applicable equally to either the helium or nitrogen injection case.

The typical effects of the downstream location on the X_j profiles are shown in Fig. 21. For helium injection, the profiles are unaffected by the increase in the downstream location. However, a slight decrease in X_j values is noted near the surface at $x/b = 114$. Analogous results are seen for the nitrogen injection case. From the results presented in these figures (and results obtained for PR = 20 at $x/b = 34$), the downstream mixing profiles are observed to be fully developed by the location of the boundary-layer reattachment.

The effects of increasing PR on the downstream mixing are shown in Fig. 22 for $x/b = 68$. The values of X_j and the penetration height (defined as location where $X_j = 0.02$) increase with PR for

ORIGINAL PAGE IS
OF POOR QUALITY

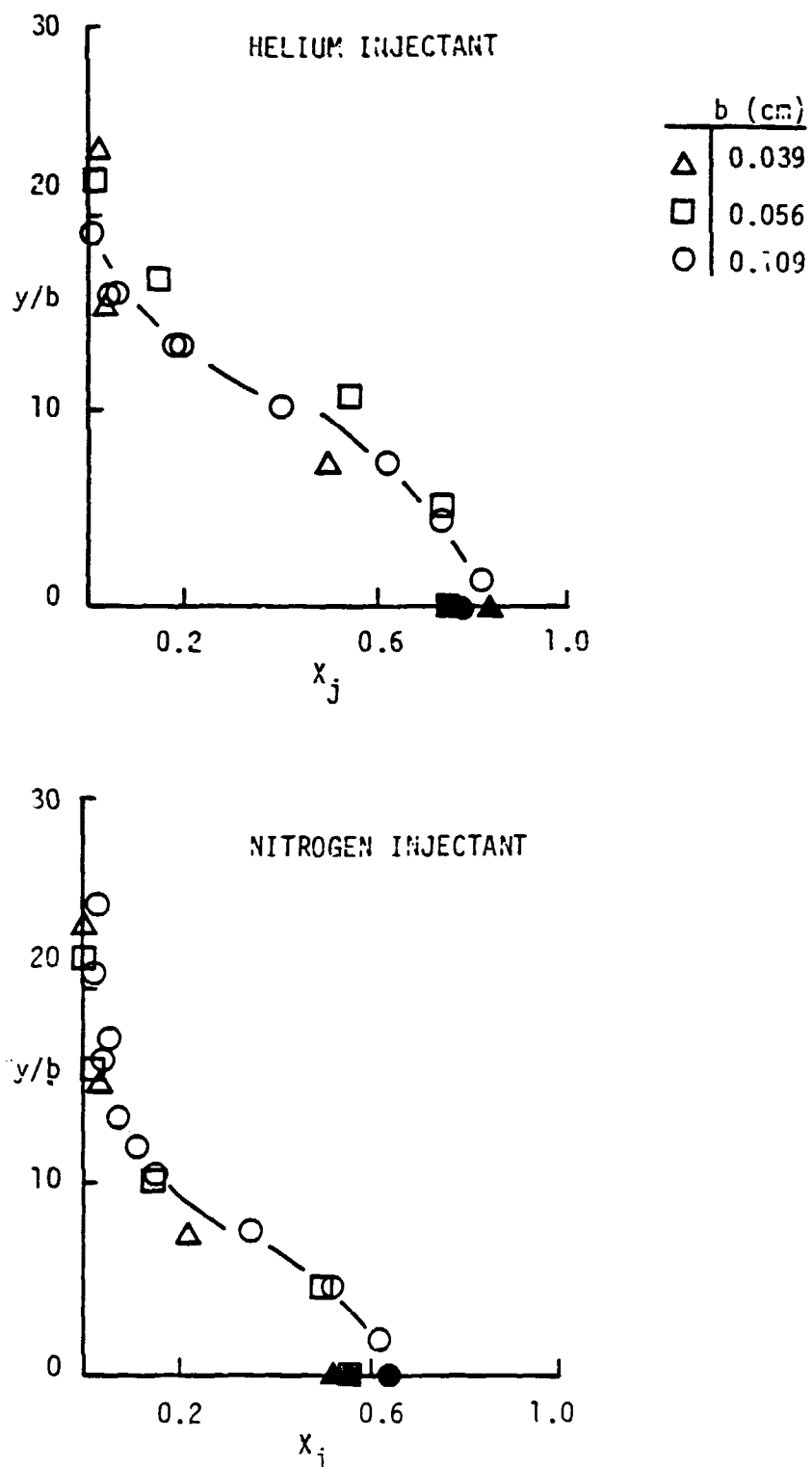


Fig. 20a. Injectant mole fraction profile correlation:
PR = .10, $x/b = 68.$

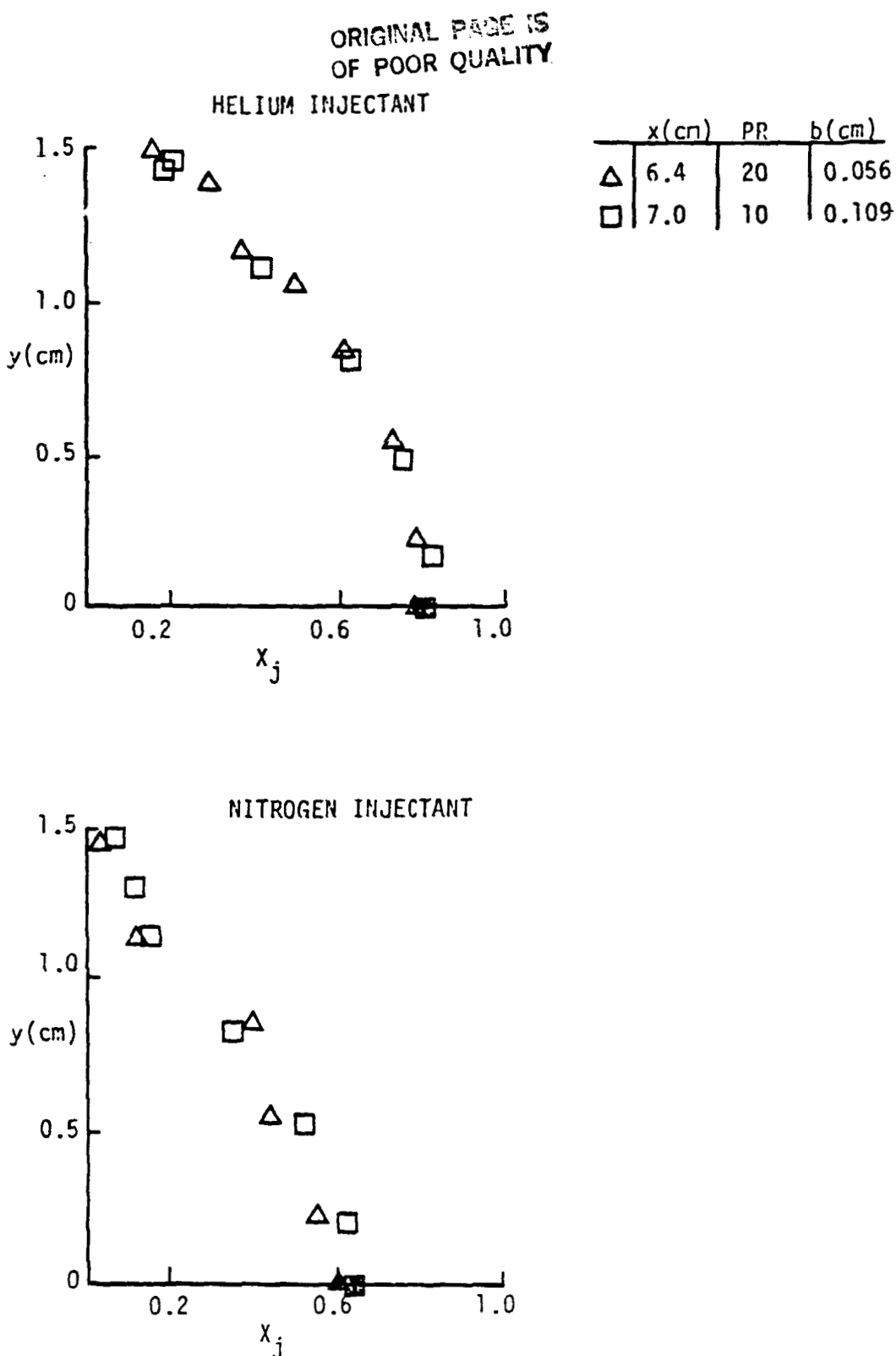


Fig. 20b. Injectant mole fraction profile correlation:
 b PR = 1.1 cm.

ORIGINAL PAGE IS
OF POOR QUALITY

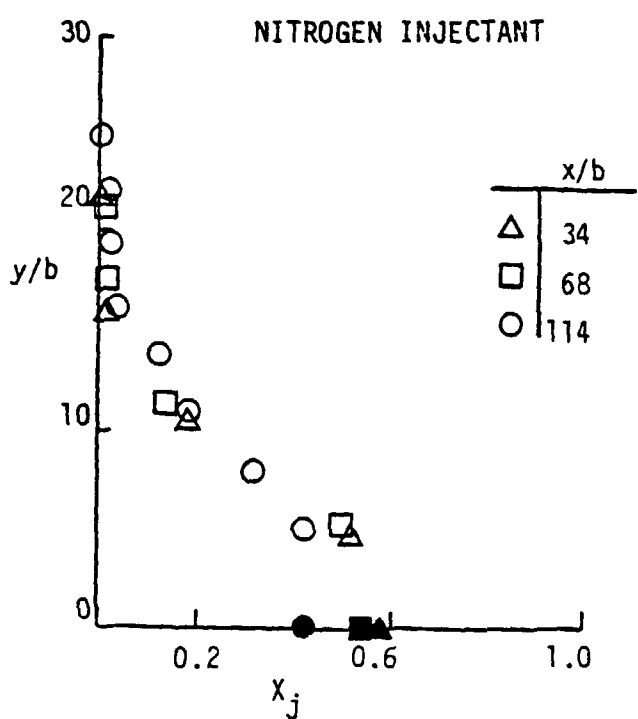
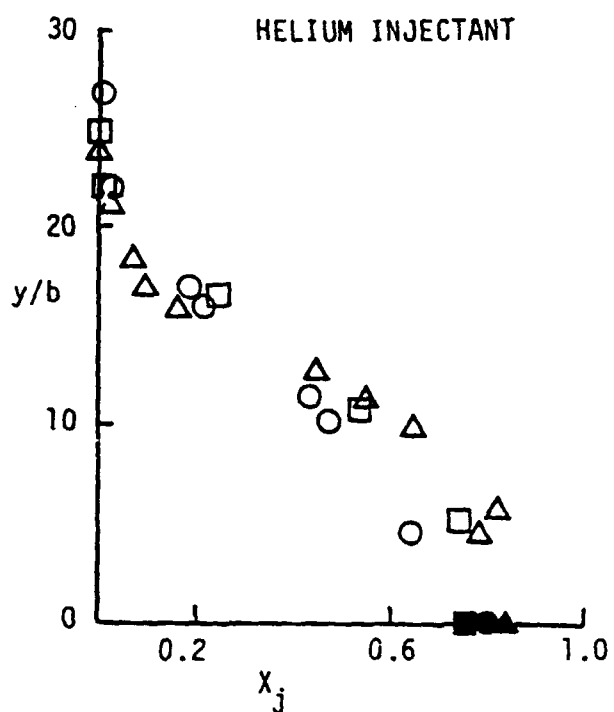


Fig. 21. Effect of downstream location on injectant mole fraction profiles, PR = 10, $b = 0.056$ cm.

helium injection. Also, the general shape of the profile is affected by increasing PR, especially further away from the injection surface.

Analogous effects are noted for the nitrogen injection profiles. For the three-dimensional case, Rogers [4] fitted similar concentration profiles with a Gaussian-type exponential curve fit. For the two-dimensional case, the equation is of the form

$$x_j/x_{j,wall} = \exp\{-a[(y/b)/(y/b)]^B\}_{x_j = 0.02} \quad (4.5)$$

For both injectants, the penetration height can be approximated by

$$y/b(x_j = 0.02) = 2 x_{1.5} \tan \quad (4.6)$$

where $x_{1.5}$ can be found from the relative jet momentum ($\gamma_j b$ PR) using Eq. (4.3). The separation shock deflection angle (θ) is found to be 12.8° from the first surface plateau pressure. A good correlation is shown in Fig. 22 for a particular injectant species and jet pressure, and the least squares fit is given by the exponential relationship of Eq. (4.5). The exponent, (B) is seen to increase with the jet pressure; however, no general relationship was found between the jet parameters and the coefficients A or B. Although the X_j profiles are very much dependent on the injectant species and jet pressure, the penetration height is directly related to the changes in relative jet momentum.

The downstream profiles of X_j have been examined for the typical effects of downstream locations and variation of the jet para-

ORIGINAL PAGE IS
OF POOR QUALITY

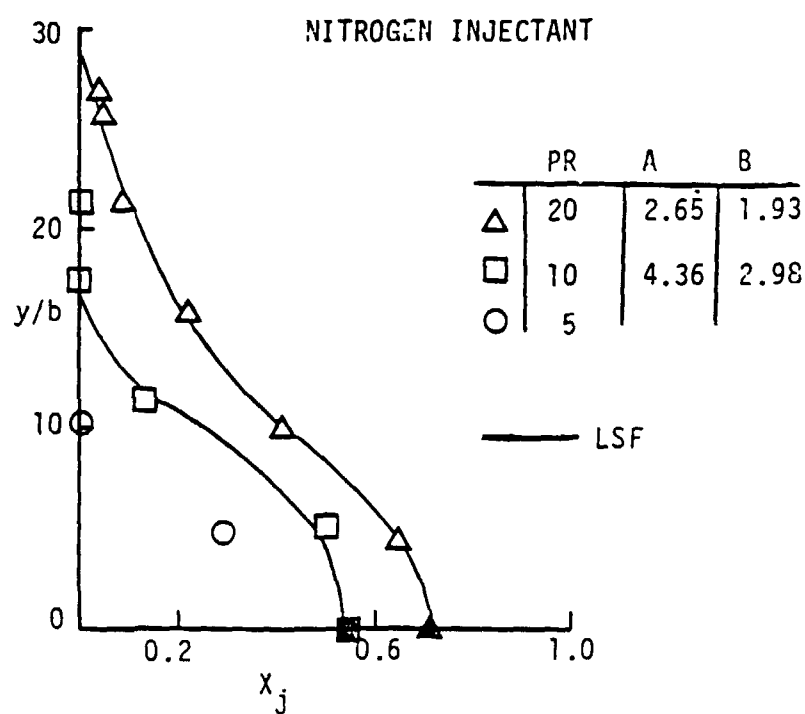
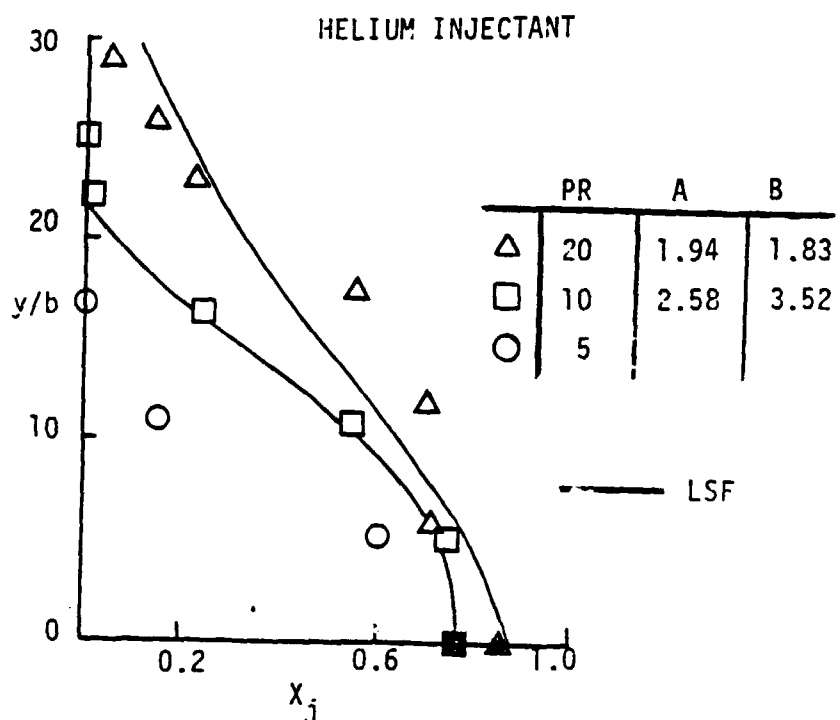


Fig. 22. Effect of jet pressure on injectant concentration profiles, $x/b = 68$, $b = 0.056$ cm.

meters. In general, the concentration decreases further away from the injection surface. The profiles are fully developed before the location of boundary layer reattachment ($x/x_{1.5} = 0.65$). Also, there is only a slight amount of mixing further downstream. Increasing PR causes an increase in the size and shape of the profiles. Although the helium injection profiles are larger than nitrogen injection profiles at analogous jet conditions due to the smaller molecular weight, the downstream penetration height can be determined from the same linear relationship for either injectant. The penetration height is directly related to the relative jet momentum and upstream separation distance. For a particular injectant species, the downstream mixing is directly effected by changes in b or the relative momentum.

4.6 Mass Flux Profiles

The downstream mass flux profiles were examined to provide additional insight into the overall data quality. The injectant mass flux profiles are shown for PR = 10 and 20 in Figs. 23. The results of trapezoidal rule integration of the mass flux profiles are shown in Fig. 24a for the total mass flow rate and in Fig. 24b for the jet mass flow rate. The mass flux was determined from the mean tunnel conditions, the pitot pressure, the air mass fraction, and the interpolated static pressure. The small values of mass flux at the surface ($y = 0$) values result from the variation in the surface pressures between the pitot and static surveys. The effect of these nonzero values is to increase the integrated mass flux by less than one percent. The integration of the mass flux profiles was performed by a trapezoidal rule method.

The typical trends of the injectant mass flux profiles are shown in Figure 23a for helium injection. Note that the solid symbols represent the surface values. The mass flux increases to a maximum value at about $y/b = 7$ and then decreases to zero at about $y/b = 23$. In general, the profile is fully developed by the first downstream location. The effects of doubling the jet pressure are shown in Fig. 23b. Doubling the jet pressure increases the maximum mass flux location to $y/b = 30$ while decreasing the value of the maximum mass flux. For nitrogen injection in Figs. 23b and 23c, similar trends of the data can be seen. The maximum mass flux appears to be larger and occurs closer to the surface ($y/b = 5$) than for the helium injection case. In Fig. 23d, doubling the jet pressure produces similar trends as noted for the helium injection case. Also, the penetration height is about $y/b = 30$ for the nitrogen injection case.

The injection mass flux profiles are fully developed by $x/b = 34$. The broadened profiles are a result of seemingly random data scatter and not due to increased downstream mixing. At the same value of PR, both injectants have the same upper limit of injectant mass transport. Also, over half of the injected mass is transported below $y/b = 10$.

An analysis of the measurement errors effecting the mass flow rate calculations is given in Appendix A. The indicated errors influence local values only by a few percent at most. However, the integrated injectant mass flow rate could have a 20 percent error due to turbulence effects [25].

A measure of the overall data quality is shown at the actual

OPINION OF THE
OF POOR QUALITY

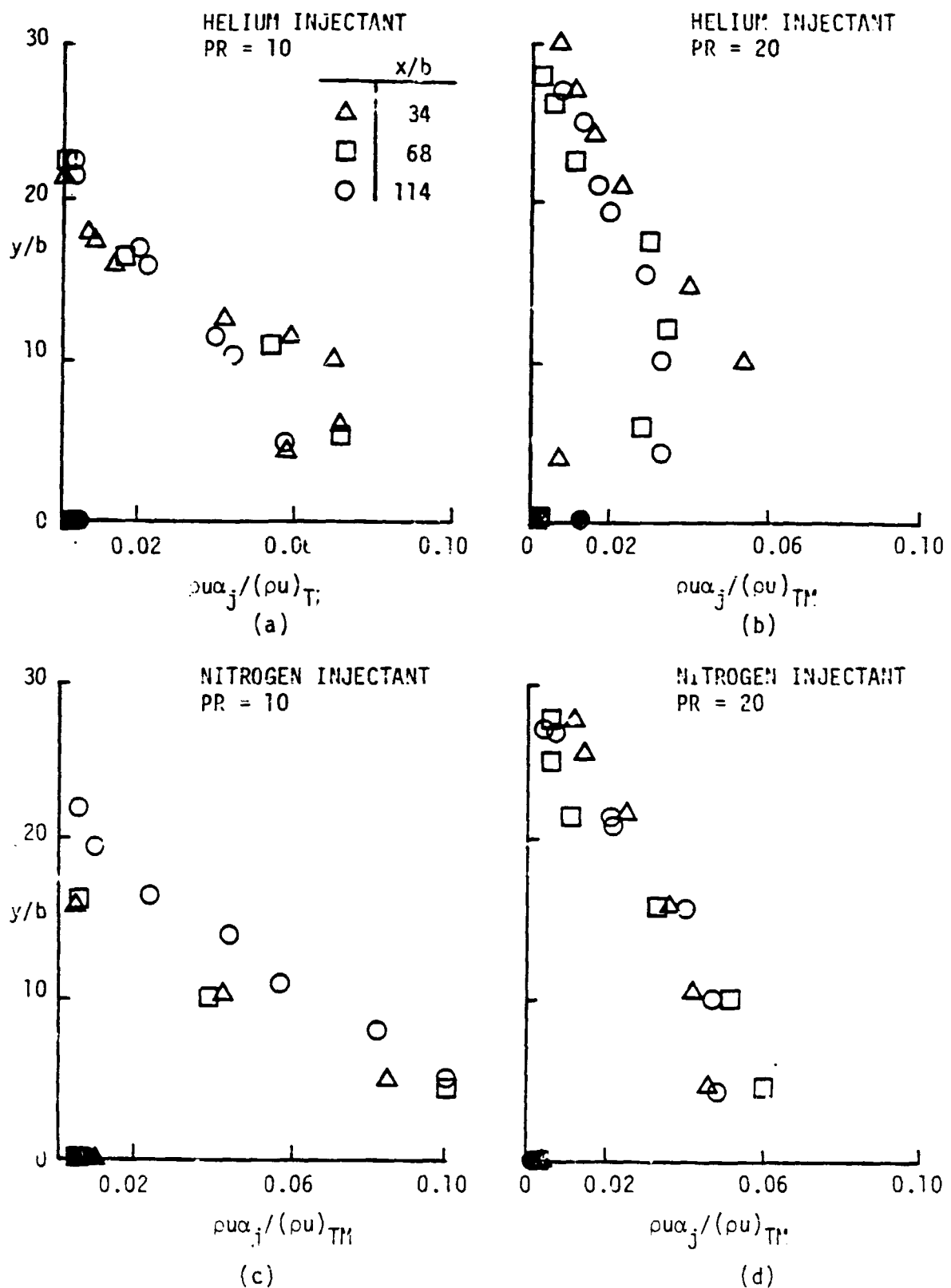


Fig. 23. Injectant mass flux profiles, $b = 0.056$ cm.

downstream locations in Fig. 24a, where the integrated mass flux is determined by integrating vertically at the tunnel centerline, nondimensionalized by the tunnel and turbine meter mass flow rates is shown. The tunnel mass flow rate is found from the mean tunnel conditions given in Table 3. Therefore, the ideal nondimensionalized value will be unity for a two-dimensional flow with no measurement errors. The nondimensionalized mass flow rate decreases almost uniformly from 1.1 at $x = 1.9$ cm to a value of almost 1.0 at $x = 6.4$ cm. The larger error values closer to the jet are probably due to the larger pressure gradients, since the slope of the pressure-rise between the shocks was observed to be influenced mostly by the downstream location in Sec. 4.4. The mass flow rates are found not to be significantly affected by the jet pressure or injectant species. The good quality of the data is demonstrated by these results.

The injectant mass flow rate variation with downstream location and jet parameters is shown in Fig. 24b. In general, the indicated data quality is better for the larger values of PR for either injectant species. Generally, the error is less than 20 percent and is attributed to turbulence effects. Therefore, the data quality is considered good except for the helium injection case at $x = 2.8$ cm and for $PR = 10$.

The injectant mass flux profiles have been characterized and examined. Despite the apparent data scatter in these profiles, the integrated results demonstrate the good overall data quality in this region. The integrated total mass flow rates indicate the good overall data quality and two-dimensionality for this investigation.

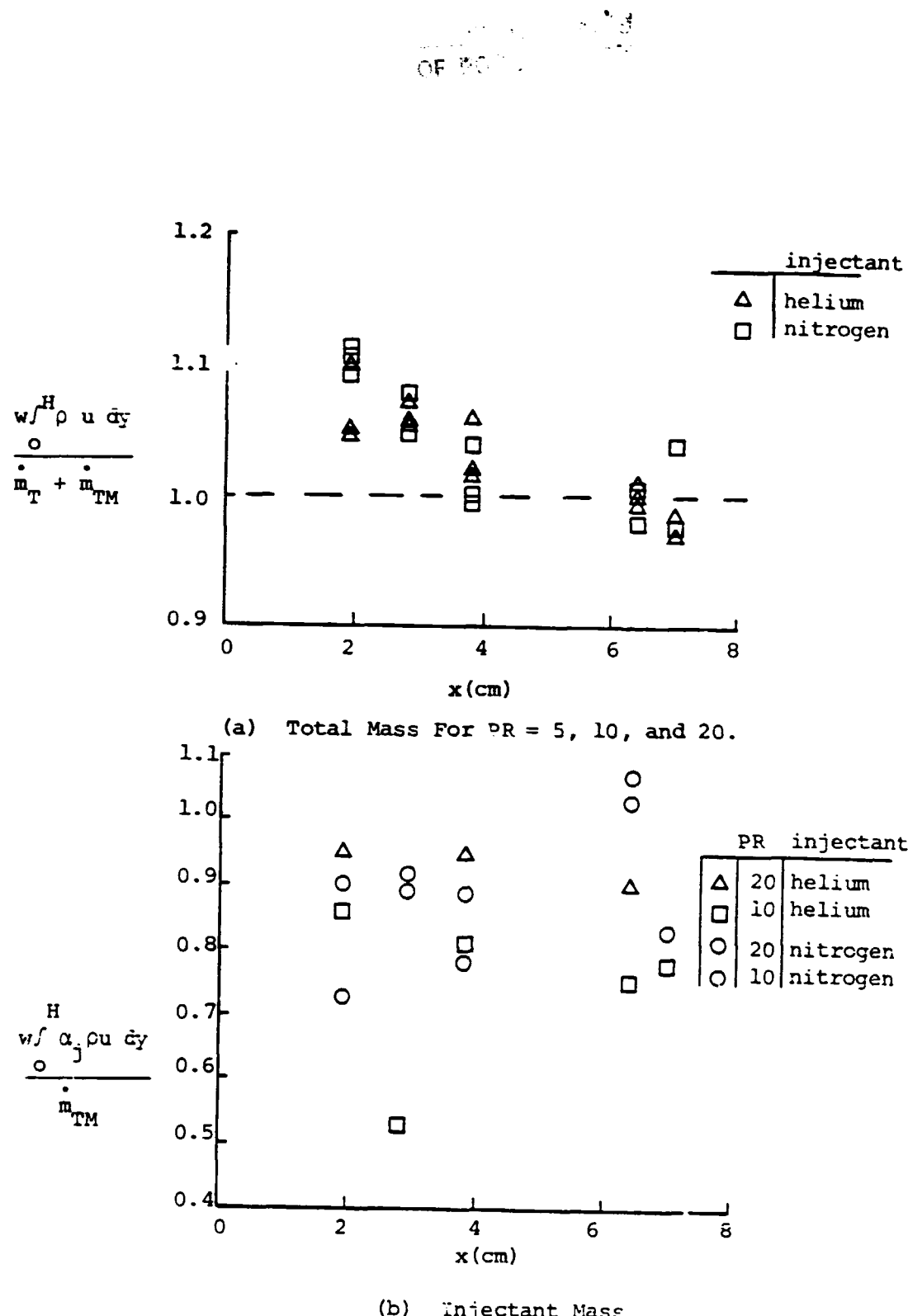


Fig. 24. Integrated mass flux variation with downstream survey location.

5. COMPARISON OF THEORY WITH DATA

As discussed in Chap. 4, the transverse jet interaction with a confined supersonic flow produces a complex mixing and interaction phenomena. The complexity of the flow field would make an analytical model very useful for parametric studies for SCRAMJET engine design. A three-dimensional code is not available at present; however, a two-dimensional code exists to examine this type of flow. The data presented in Chap. 4 are useful in establishing the validity of the existing analysis. In this chapter, a comparison will be made between the data and code developed for similar flows.

5.1 Model for Theoretical Investigation

Drummond has developed a two-dimensional elliptic flow theory to describe this complex flow field [3]. The code solves the discretionary form of the full Navier-Stokes equations using a time-split McCormack scheme [26]. A coordinate transformation by Smith and Weigel is used to concentrate the grid near the injector in both the horizontal and vertical axes [27]. Complete description of this computational model is available in the cited references. This computational model was used to obtain theoretical results by using the appropriate conditions for the present experimental model.

Theoretical results were obtained for three separate cases to examine the effects of varying the injectant species and jet pressure. These were for nitrogen injection with PR = 10 and for helium injection with PR = 10 or 20. The other jet conditions used

were a total temperature of 300 K, $b = 0.056$ cm, and a Mach number of 1.00. The inlet conditions used were a total temperature 300 K, a total pressure of 2.07 MPa, and a Mach number of 2.90 for air flow. The results for all three cases were allowed to advance in time to a steady state solution. However, small oscillations were noted in the results. These are similar to the small oscillations at frequencies less than 50 Hz noted in the previous experimental studies for analogous flows [28-30].

5.2 Comparisons of Results for Surface Distributions

Comparisons of the surface pressure data with the theoretical results are shown in Figs. 25. The coordinate system and nondimensional parameters used for the comparisons are the same as given in Chap. 4. For nitrogen injection, the results are compared in Fig. 25a for $PR = 10$. The results show that the initiation of upstream separation occurs earlier in the data ($x/b = -35$) than the theoretical results ($x/b = -30$). The data and theoretical results compare well after $x/b = -23$, the location near the initiation of the first plateau pressure region. A small drop in the surface pressure is observed for the theoretical results very near the jet ($x/b = -3$). A similar decrease in the surface pressure (very near the jet) was noted in the air injection investigation by Sterrett and Barber [2]. Downstream of the jet, the agreement is good aside from the following two exceptions. The theoretical results show the initiation of the downstream pressure rise at an earlier location ($x/b = 8$) than the data ($x/b = 13$). Also, the theory does not predict the downstream peak pressure observed in the data at $x/b = 27$. Therefore, the turning of the flow associated with boundary

ORIGINAL PAGE IS
OF POOR QUALITY

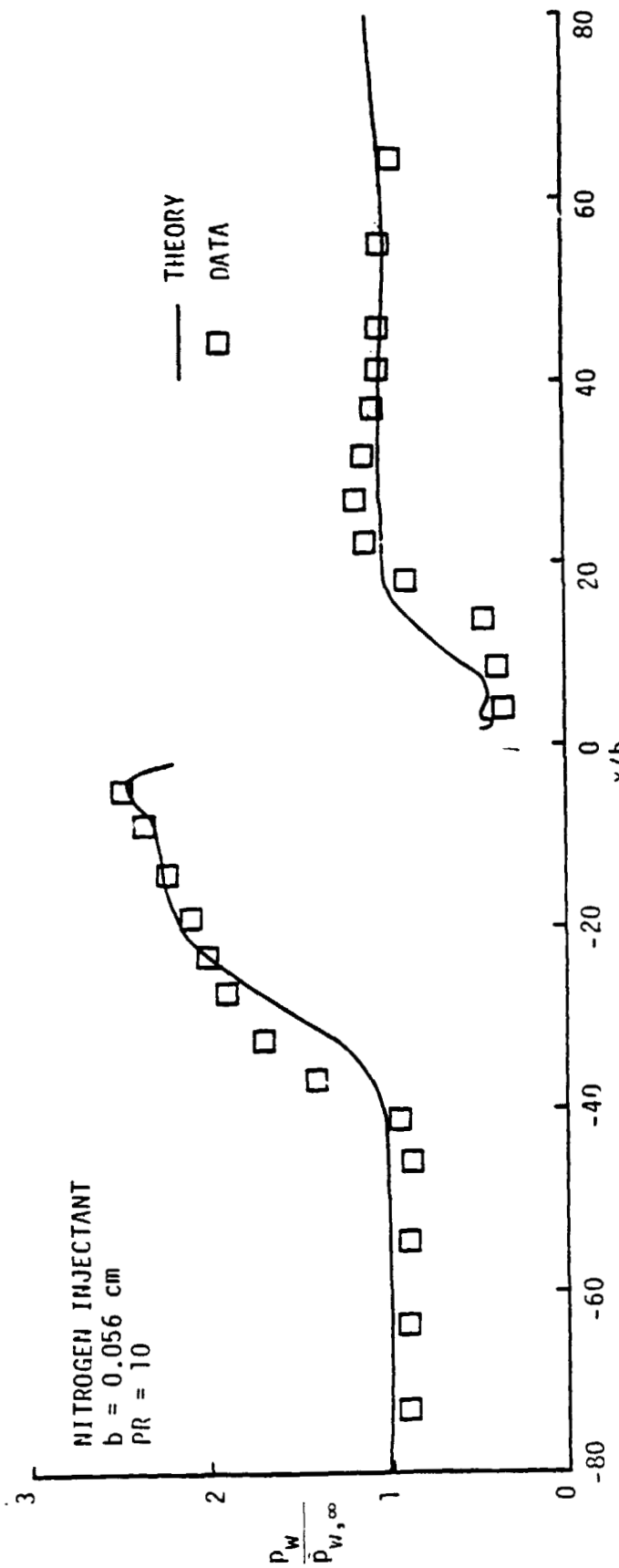


Fig. 25a. Comparison of surface pressure distributions, $b = 0.056 \text{ cm}$: nitrogen injectant.

ORIGINAL PAGE IS
OF POOR QUALITY

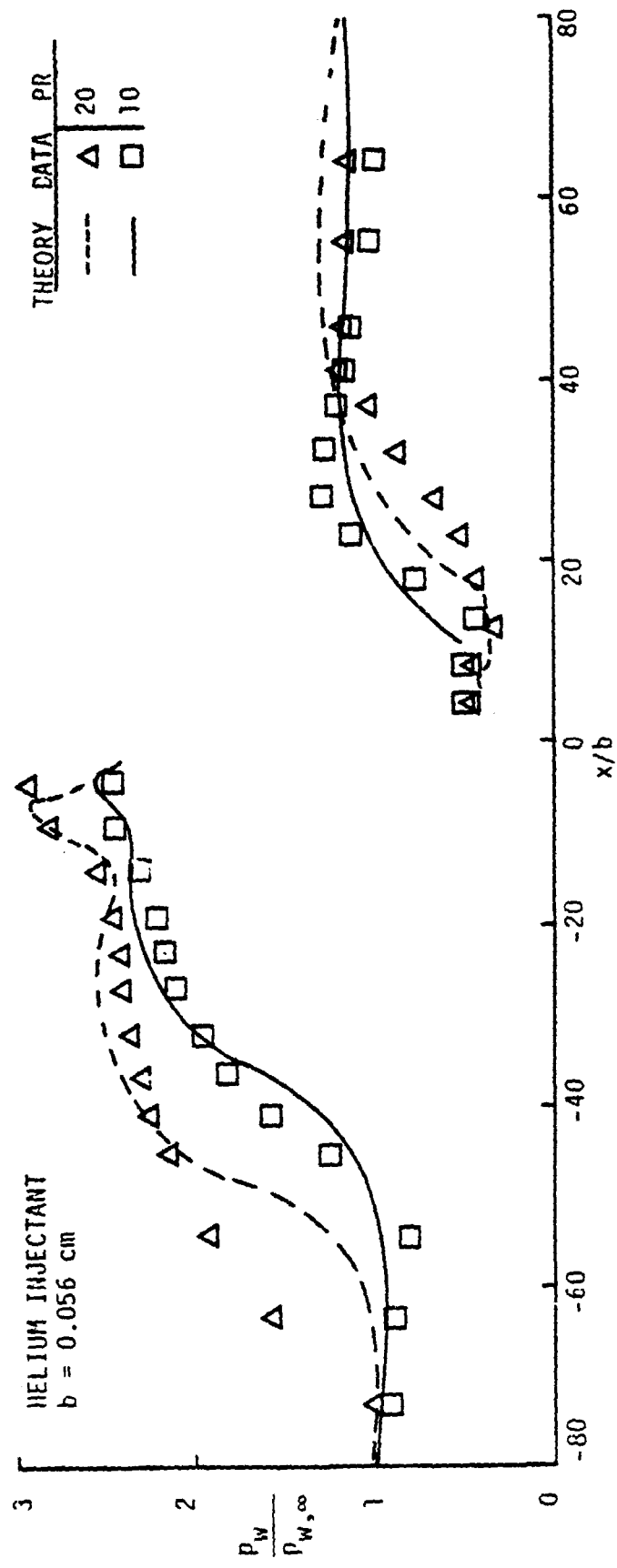


Fig. 25b. Comparison of surface pressure distributions, $b = 0.056 \text{ cm}$: helium injectant.

layer reattachment is not properly predicted by the code. For helium injection, a similar comparison with data is seen in Fig. 25b for PR = 10. In the same figure, doubling the helium jet pressure produces a larger pressure on the surface. Therefore, the comparison appears to be of poor quality, although the trend is analogous to that noted for PR = 10 cases. In general, the theoretical results compared well with the data. However, the code underpredicts the location of the boundary layer separation and the beginning of the downstream pressure rise and does not show the existence of the downstream peak pressure.

Comparisons between data and theoretical results for the surface injectant mole fraction (X_j) are shown in Figs. 26. For nitrogen injection, Fig. 26a shows a poor comparison with data. The theoretical results agree well with the location of the upstream injectant spread ($x/b = -31$). Thereafter (in the upstream region), the code predicts trends similar to the data, but it indicates much larger concentrations. The first X_j plateau occurs at $x/b = -20$ and ends at about $x/b = -8$ for both theory and data, also the value of X_j is seen to increase closer to the jet. In the plateau region, the theory predicts a value of X_j approximately 2.5 times larger than the data ($X_j = 0.08$). Downstream, the agreement between data and theoretical results is poor. The low values of X_j indicated by data in the downstream recirculation region are probably due to entrained air or three-dimensional effects. As such, one would not expect a good agreement between the data and theory in this region. Note that both theory and data show a similar trend in X_j values downstream of the recirculation region ($x/b = 28$). In

general, the code predicts a surface distribution of X_j similar to that found in the data, but the theory overpredicts the concentration. This difference could be due to the sample collection system, collecting samples a significant distance above the injectant surface. This off-surface sample collection would lower the value of X_j in the data. To determine this, theoretical results for a small-constant height above the injection surface ($y = 0.13$ and 0.27 cm) were also compared with data in Fig. 26a. It is noted that in the upstream region, the penetration is greatly underpredicted by the theory for $y = 0.13$ cm at $x/b = -22$ and for $y = 0.27$ cm at $x/b = -14$. For either distribution, the concentration increases over the data's plateau region. The results, therefore, indicate that the off-surface sample collection would cause the concentration to increase without a plateau region. However, a plateau region does exist for the data. Thus, only theoretical results for the surface are considered for comparisons with the data.

Comparison between data and theory are shown in Fig. 26b for helium injection. For $PR = 10$, the upstream plateau region extends from about $x/b = -38$ to -25 for the data and from $x/b = -21$ to -10 for the theoretical results. For $PR = 20$, the upstream lead occurs at about the same location ($x/b = -60$) for the data and results. Also, the upstream plateau region extends from about $x/b = -36$ to -14 for the data and from $x/b = -35$ to -13 for the results. After the plateau region, the values of X_j increase closer to the jet. A sample collection problem most likely caused the low value at $x/b = -4$ for $PR = 20$. The trends in the data are represented well by the code for the $PR = 20$. The trends in the data are

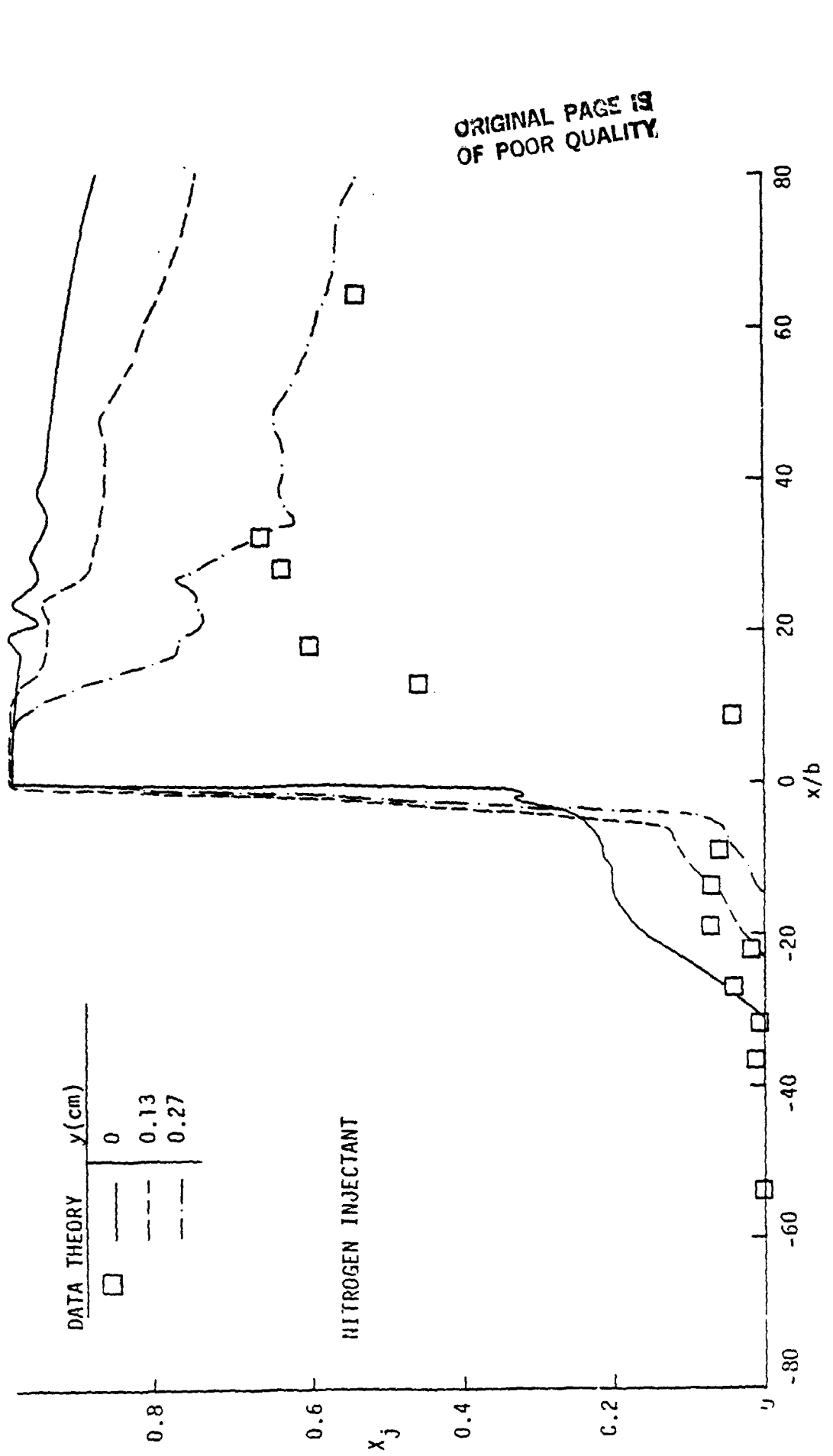


Fig. 26a. Comparison of injectant mole fraction surface distributions, $b = 0.056 \text{ cm}$:
nitrogen injectant.

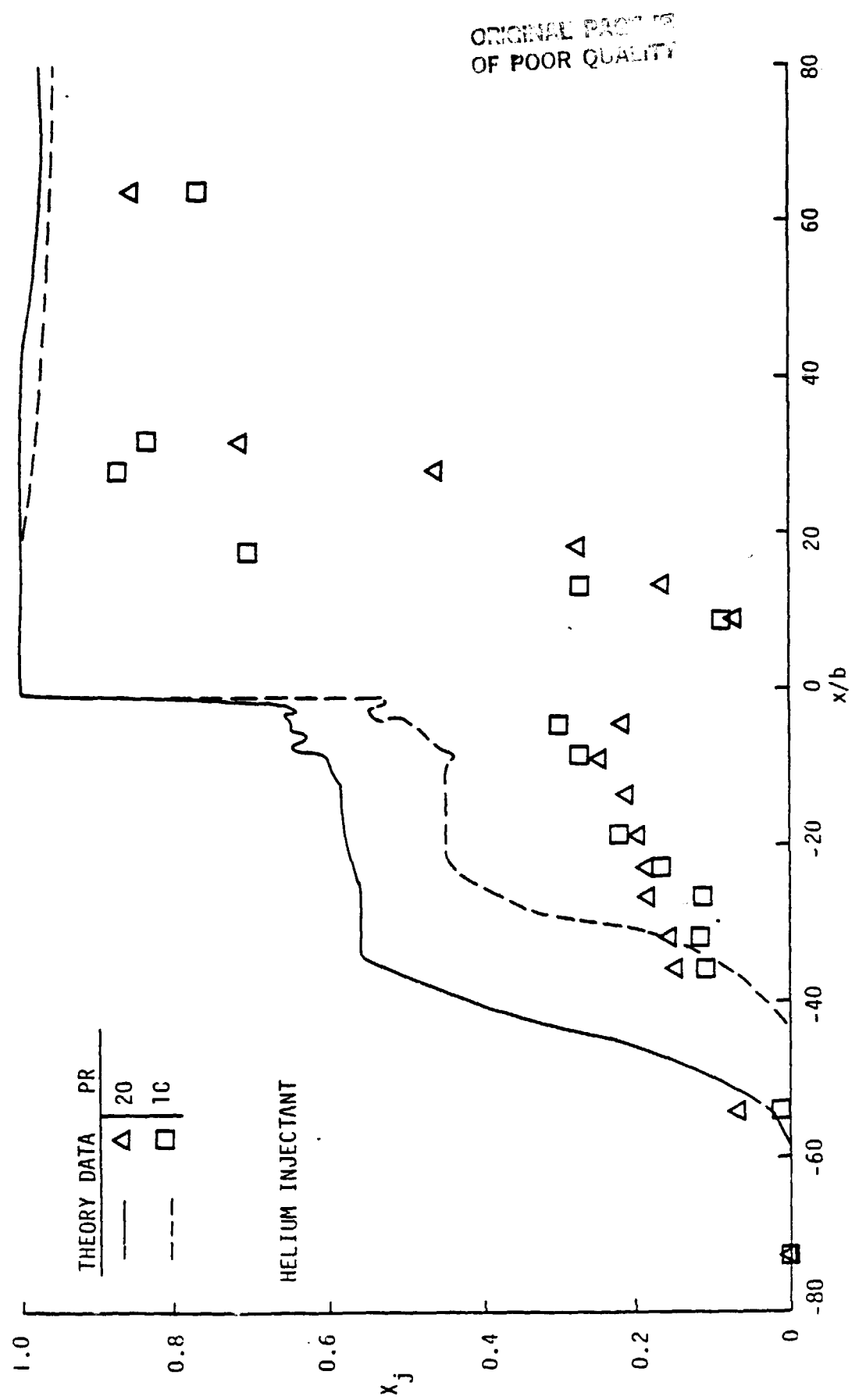


Fig. 26b. Comparison of injectant mole fraction surface distributions, $b = 0.056$ cm; helium injectant.

represented well by the code for the PR = 20 case and in fair agreement for the PR = 10 case. A valid downstream comparison cannot be made for reasons previously discussed for the recirculation region. Further downstream, the code correctly predicts the trend of decreasing concentration but overpredicts the values.

In general, the code correctly predicts the trends of the injectant mole fraction distributions. However, the values of the injectant mole fraction are greatly overpredicted by the theory. This lack of agreement for the value of the injectant mole fraction is not believed to be due to errors in the method of surface sample collection.

5.3 Comparisor of Results for Downstream Profiles

Comparisons of the static pressure profiles data with theory are presented in Fig. 27 for the survey, locations of $x/b = 34$ and 68 . For nitrogen injection, the results are compared with data in Fig. 27a for PR = 10. Both the data and theory show that the recompression shock is about $y/b = 13$ for $x/b = 34$ and at about $y/b = 22$ for $x/b = 68$. A linear pressure rise is observed between the shocks; however, a smaller slope is noted for the theoretical results because the bow shock is located closer to the surface. At $x/b = 34$, the bow shock location is seen to be lower for the theory ($y/b = 34$) than the data ($y/b = 46$). Further downstream (at $x/y = 68$), the bow shock location in the theoretical results ($y/b = 54$) has increased in distance away from the location in the data ($y/b = 75$). By oblique shock theory, the bow shock angle is found to be 29° for the data. However, in the theoretical results, the bow

shock angle decreases from 31° to 29° further downstream. This accounts for the increasing distance between the bow shock locations for data and theory further downstream. In the theoretical results, the blunt bow shock indicates the distance between computational grid points. From this indication of the grid spacing at the bow shock location, the bow shock is seen to be smeared over only about three grid points (i.e., from $y/b = 54$ to 75 at $x/b = 68$). After the bow shock region, the static pressure is almost at the undisturbed value ($p/p_b = 0.032$) for both data and theory. In general, the theoretical results agree very well with the data trends. However, the shock structure is incorrectly predicted with regards to the recompression shock strength and the bow shock location and strength.

A similar comparison with the data is shown in Figs. 27b and 27c for helium injection. For $PR = 10$, the bow shock angle is found to be approximately 29° from the data (Fig. 27b). The theoretical results, however, show that the bow shock angle decreases from 37° at $x/b = 34$ to 29° at $x/b = 68$. For the theory, however, the shock angle decreases from 37° to 33° over the same region. The recompression shock is located at $y/b = 12$ for $x/b = 34$ and at $y/b = 26$ for $x/b = 68$. These locations are the same for both the data and results and for both jet pressures.

In general, the theory predicts the trends in data very well with the exception of the shock strength and bow shock location. At the same PR , the theoretical results predict the downstream static pressure field equally well for either injectant species. For the same injectant species, doubling the jet pressure mainly affects the

ORIGINAL PAGE IS
OF POOR QUALITY

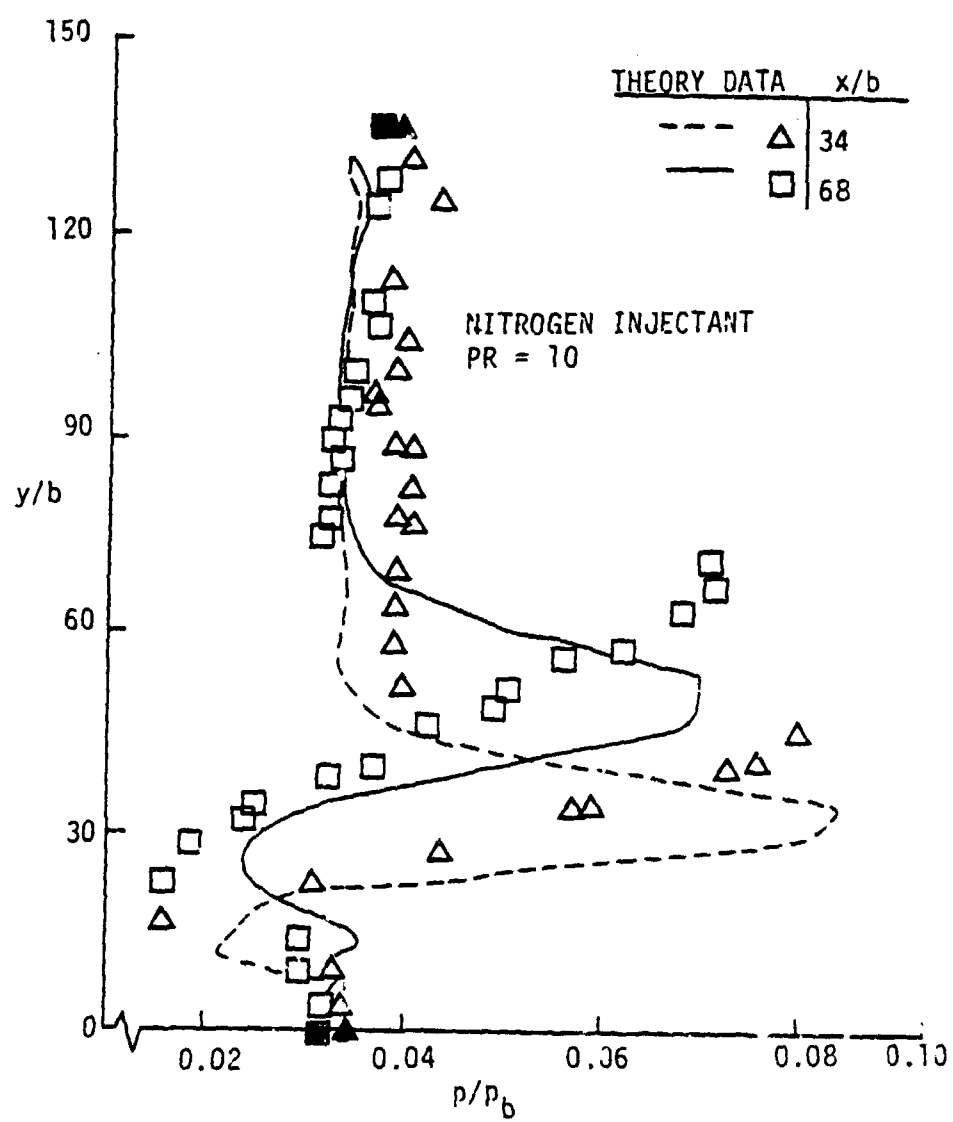


Fig. 27a. Comparison of static pressure profiles, $b = 0.056$ cm;
nitrogen injectant.

ORIGINAL PAGE IS
OF POOR QUALITY

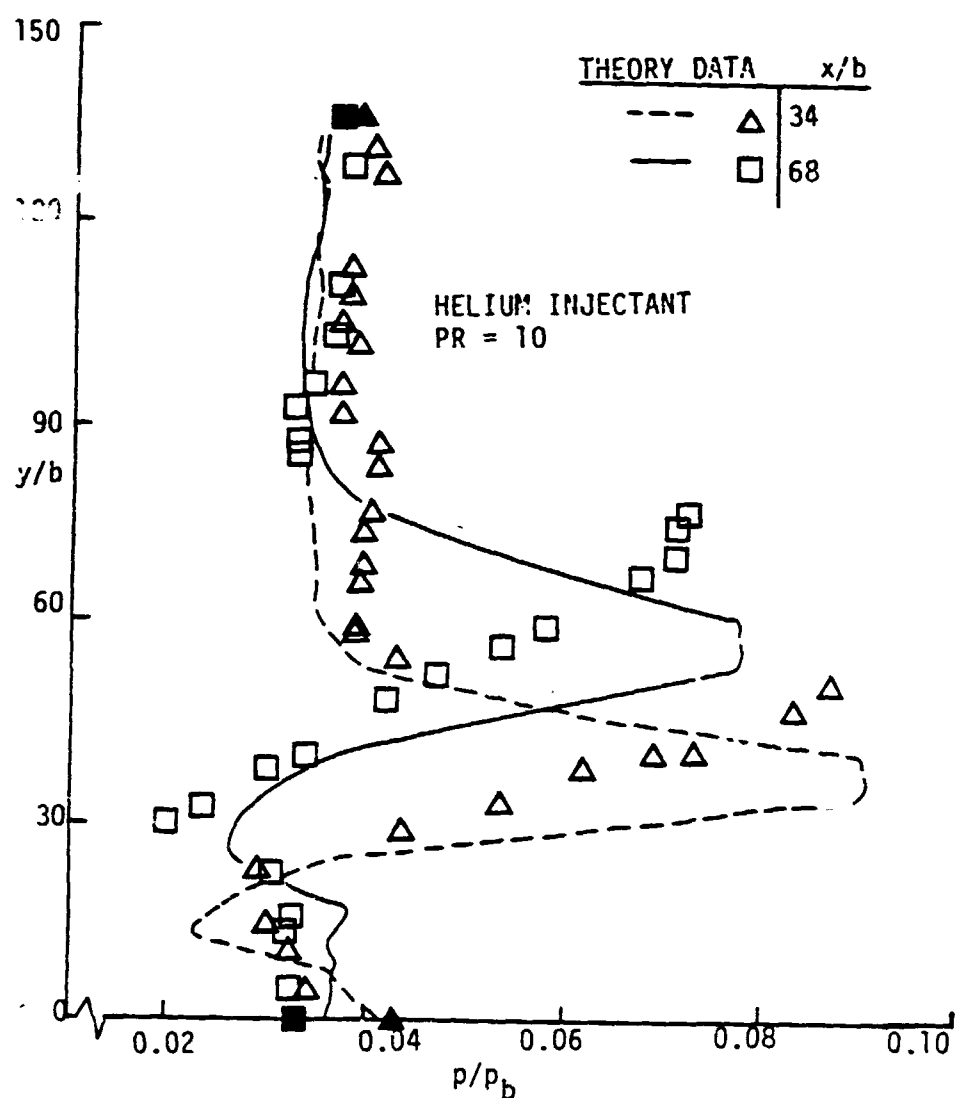


Fig. 27b. Comparison of static pressure profiles, $b = 0.056$ cm:
helium injectant.

C-2

ORIGINAL PAGE IS
OF POOR QUALITY

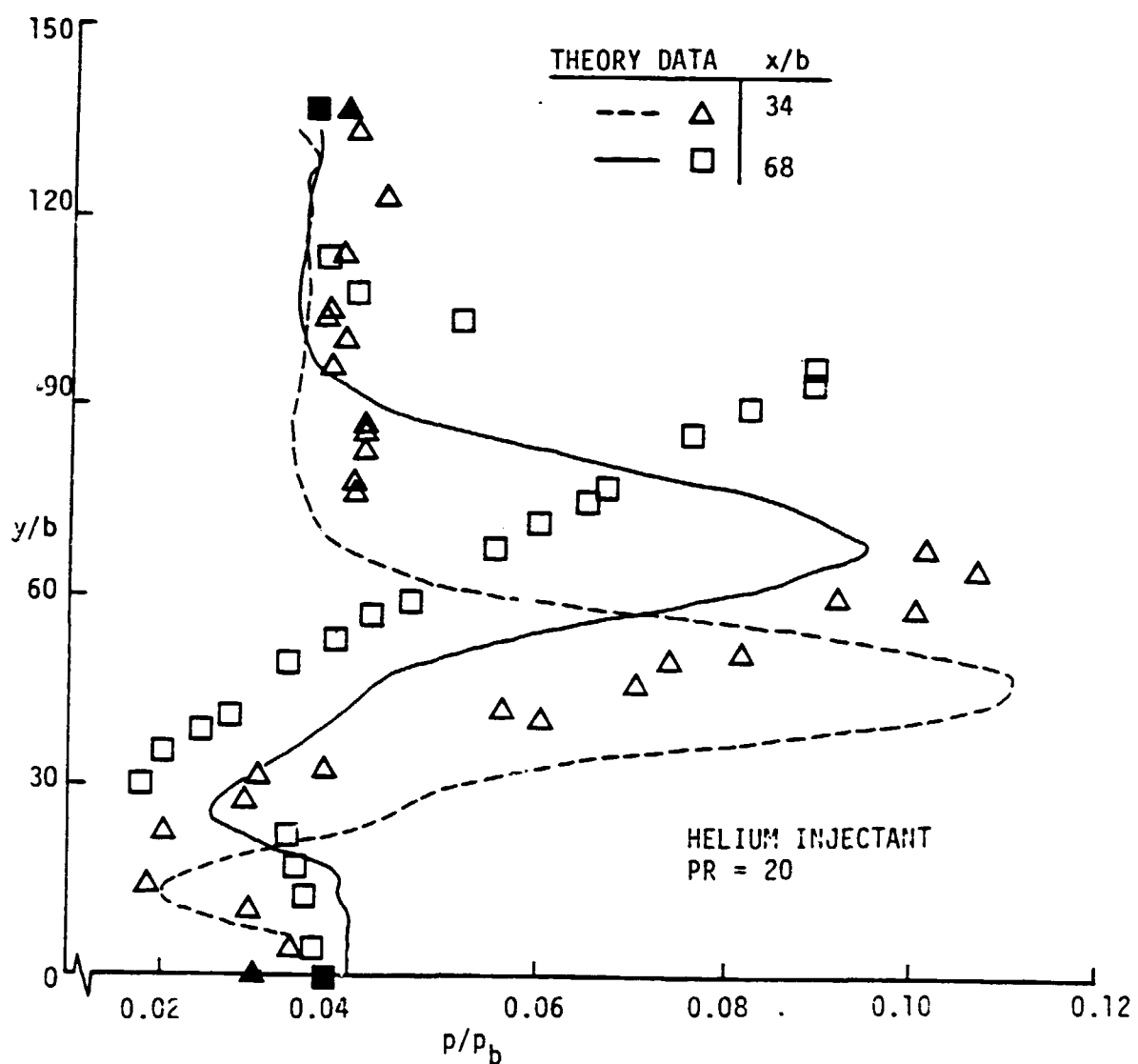


Fig. 27c. Comparison of static pressure profiles, $b = 0.056$ cm:
helium injectant.

prediction of the bow shock strength. The theory does predict correctly the independence of the recompression shock location with varying values of PR.

The pitot pressure profiles are compared in Figs. 28 for the downstream locations of $x/b = 34$ and 68 . For nitrogen injection, Fig. 28a shows a good agreement between the theory and data up to the theoretical bow shock location. The shock locations, of course, are the same as in the static pressure profiles. Both the recompression and bow shock strengths are underpredicted by the theory. After the bow shock, the data and theoretical results approach the undisturbed value of $p_t/p_b = 0.36$. For helium injection, a similar comparison is shown in Fig. 28b for $PR = 10$ and in Fig. 28c for $PR = 20$. Note that the agreement with data is not affected by the injectant species or jet pressure except for the bow shock location. In general, the theory predicts the trends in data very well. However, the shock strengths are underpredicted in the pitot pressure results.

The injectant mole fraction profiles are compared in Figs. 29 at $x/b = 34$ and 68 . Note that the vertical axis is expanded three times larger than previously used for the pressure profiles. For nitrogen injection, Fig. 29a shows a good agreement between the theory and data. However, the theory overpredicts the value of X_j from the surface to the first instream data point ($y/b = 5$). At the surface, the mean value of X_j from the surface to the first instream data point ($y/b = 5$). At the surface, the mean value of X_j is 0.56 for the data and 0.94 for the theory. Good agreement with data is observed after the first instream data point. For helium injection,

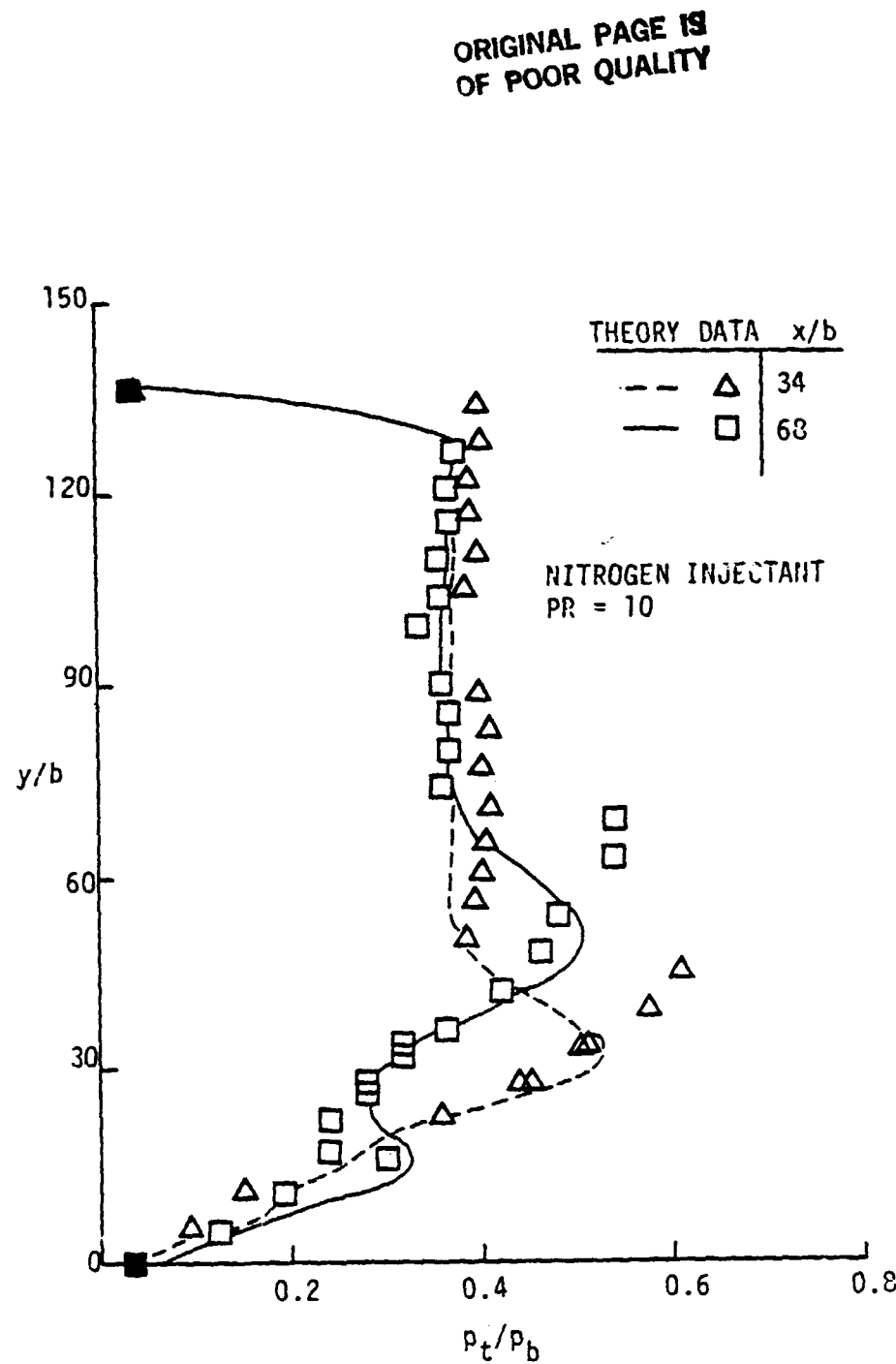


Fig. 28a. Comparison of pitot pressure profiles, $b = 0.056$ cm:
nitrogen injectant.

ORIGINAL PAGE IS
OF POOR QUALITY.

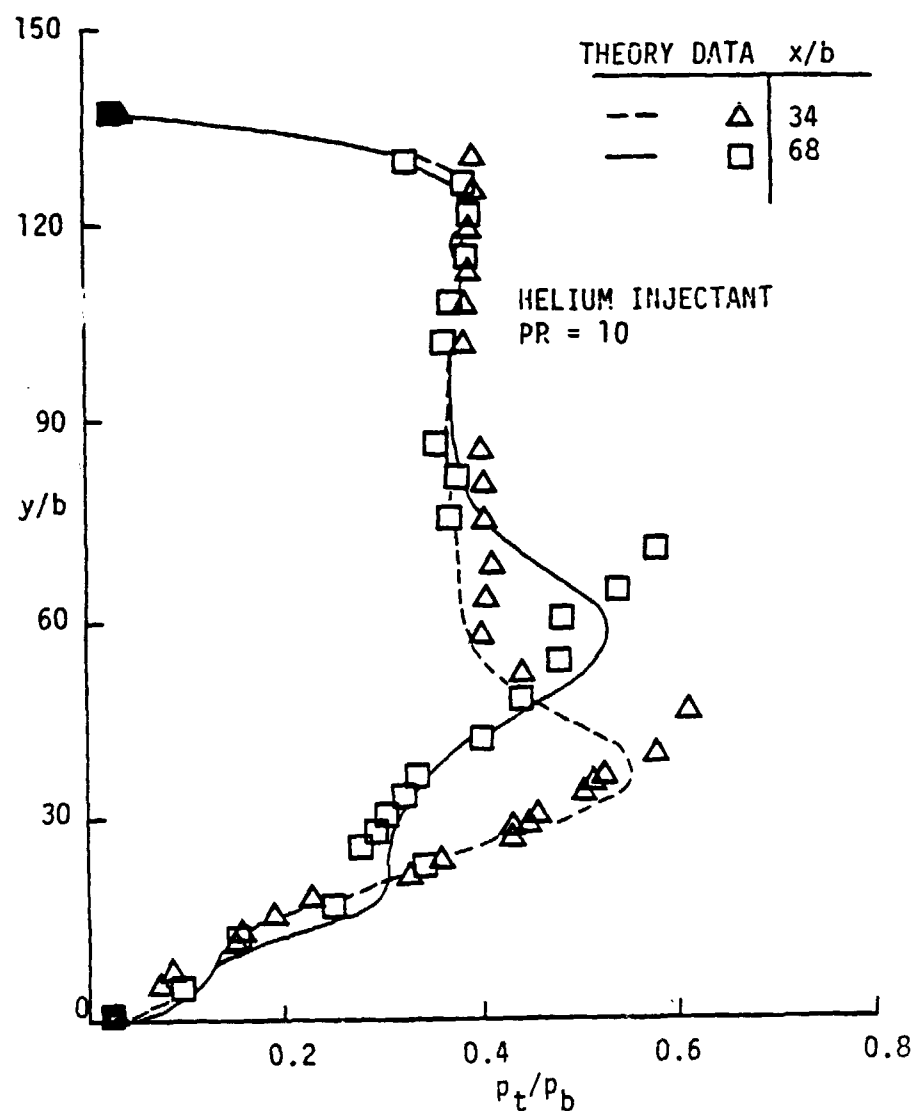


Fig. 28b. Comparison of pitot pressure profiles, $b = 0.056 \text{ cm}$: helium injectant.

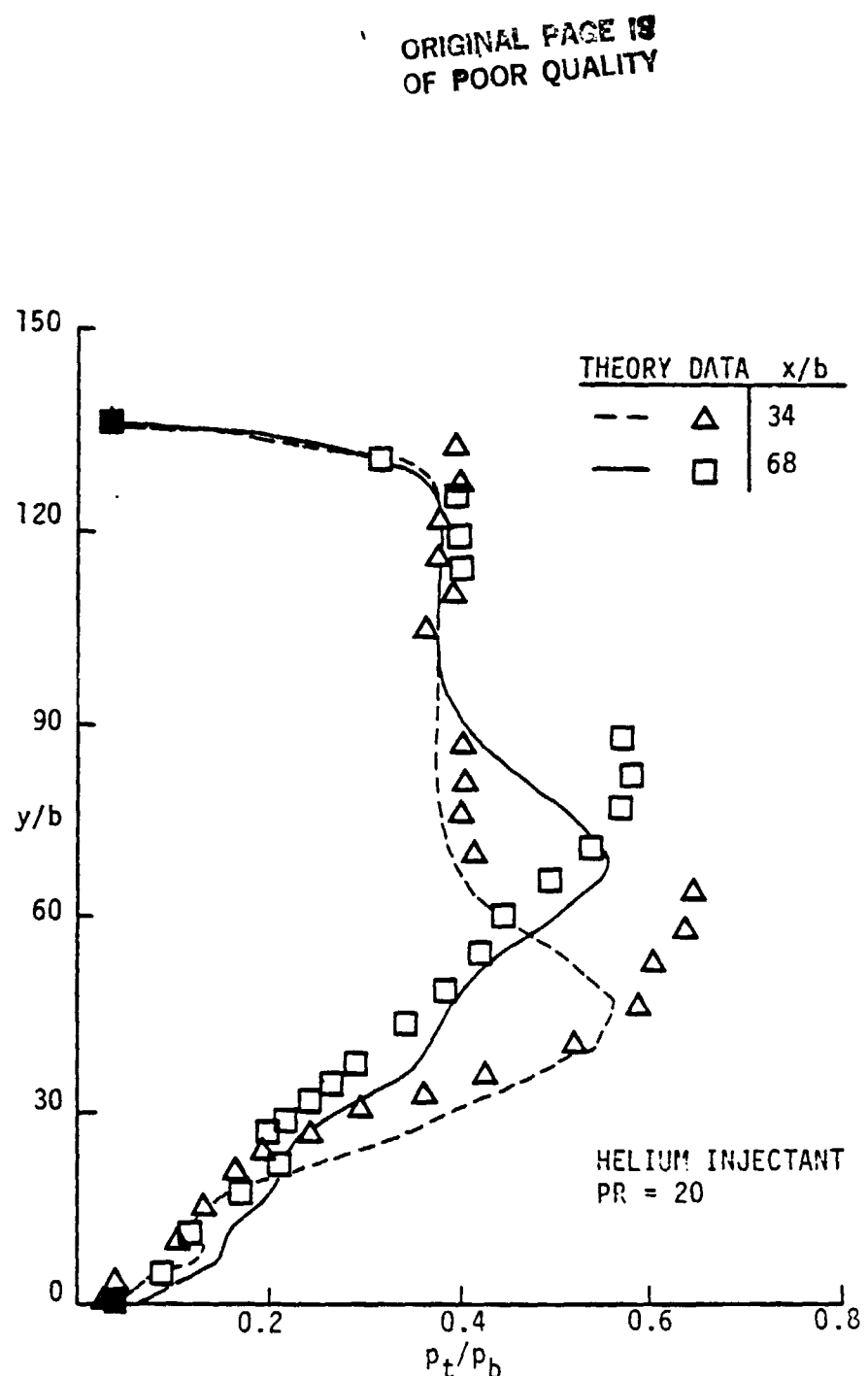


Fig. 28c. Comparison of pitot pressure profiles, $b = 0.056$ cm:
helium injectant.

ORIGINAL PAGE IS
OF POOR QUALITY.

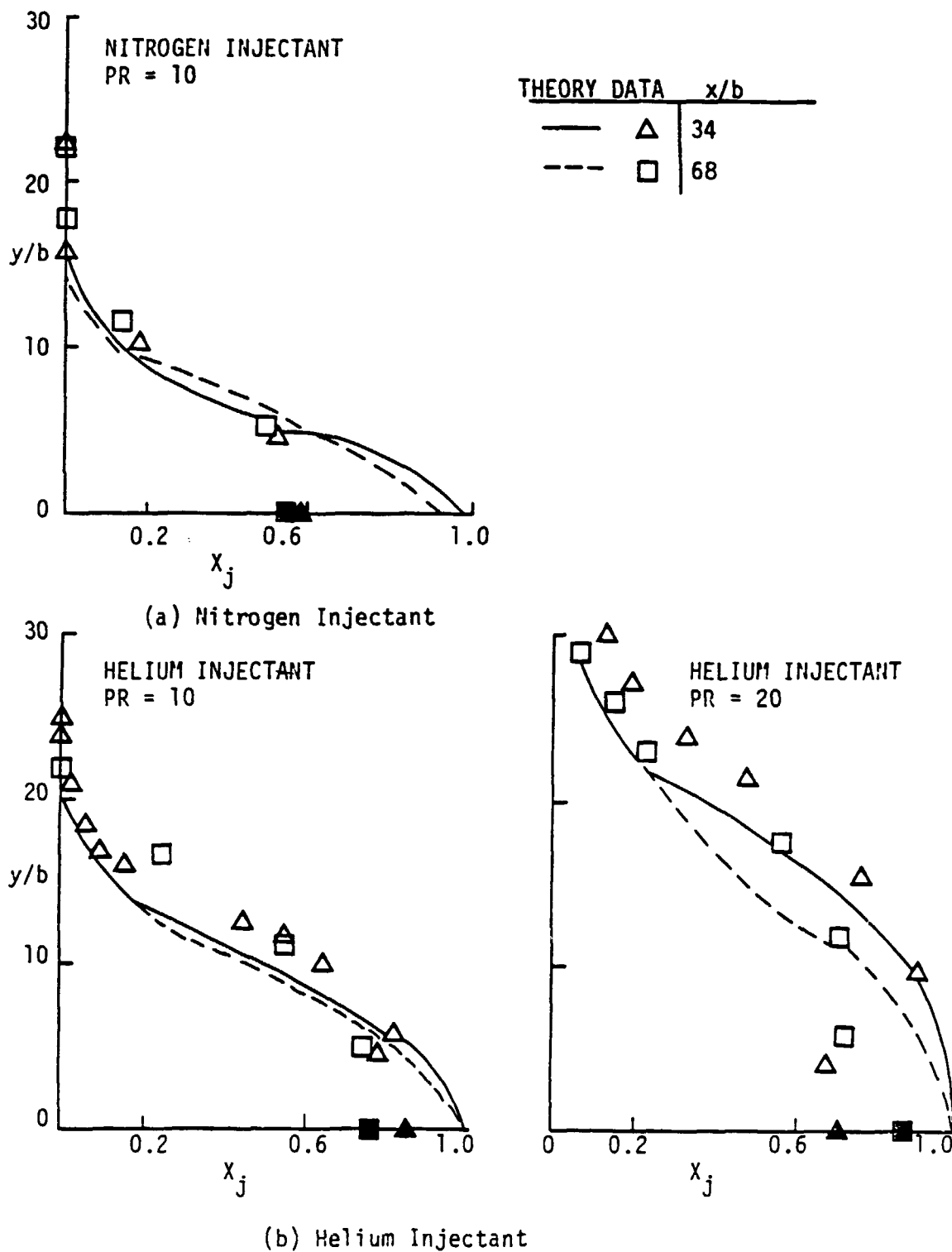


Fig. 29. Comparison of injectant mole fraction profiles, $b = 0.056$ cm.

a similar comparison is shown in Fig. 29b for $PR = 10$. A better agreement is evident from the mean surface X_j values of 0.83 for the data and 0.91 for the theory. The results for $PR = 20$ are also compared in Fig. 29b. It is seen that doubling the jet pressure decreases the agreement near the surface ($y/b > 10$). Good agreement in theoretical results is observed after $y/b = 10$. However, the theory predicts a slightly lower concentration. In general, a very good agreement between the data and theory is observed except very near the surface.

The above comparisons reveal that, in general, the theory predicts the trends in data very well. However, in certain regions the theory does not correctly predict the locations and values of the profile quantities. The bow shock location is underpredicted by the theory; the bow shock strength is overpredicted in the static pressure profiles and underpredicted in the pitot pressure profiles. In both profiles, the recompression shock strength is underpredicted. The injectant concentration is overpredicted very near the surface. The extent of these disagreements is further examined by comparing the injectant mass flux, total mass flux, and Mach number profiles in Figs. 30 to 32, respectively. In each figure, the typical case examined is for helium injection with $PR = 10$ at $x/b = 68$. As discussed in Sec. 3, the Mach number and mass flux are determined primarily by interpolating the value of the static pressure at pitot pressure locations and by using the Rayleigh pitot formula.

Downstream profiles of injectant mass flux ($\alpha_j \rho u$) are shown in Fig. 30. The injectant mass flux increases to an off-surface maximum before decreasing to zero at about $y/b = 21$. The maximum value

for the theoretical results is located at $y/b = 3$, whereas the maximum value for the data is at about $y/b = 7$ (Fig. 23a). This value appears to be less than one. However, the maximum value for theory is 1.24. The theory correctly predicts the profile trends but not the location or values of the injectant mass flux near the surface ($y/b < 11$) due mainly to the overprediction of X_j near the surface.

Downstream profiles of the total mass flux (ρu) are compared in Fig. 31. Very good agreement is observed except near the location of the recompression shock ($y/b = 20$) and the bow shock ($y/b = 60$ for theory). The theory overpredicts the mass flux near the recompression shock and underpredicts the mass flux near the bow shock by $\rho(\rho u)_T = 0.12$. The theory accurately predicts the boundary layer region at the opposite wall. In general, the theory agrees very well with the data.

The Mach number (M) profiles are shown in Fig. 32. At the locations previously noted, the Mach number is underpredicted by 0.4 at the shock locations. However, the theory predicts the general trends of the data very well.

In the downstream mixing region, the overprediction of the concentration near surface by the theory has a significant effect on the injectant mass flux profile. Therefore, the theory predicts that most of the injectant mass transport occurs closer to the surface. Weaker recompression and bow shock strengths are predicted by the theory, even though the bow-shock strength is overpredicted in the static pressure results.

The essential features of the complex flow field have been

ORIGINAL PAGE IS
OF POOR QUALITY

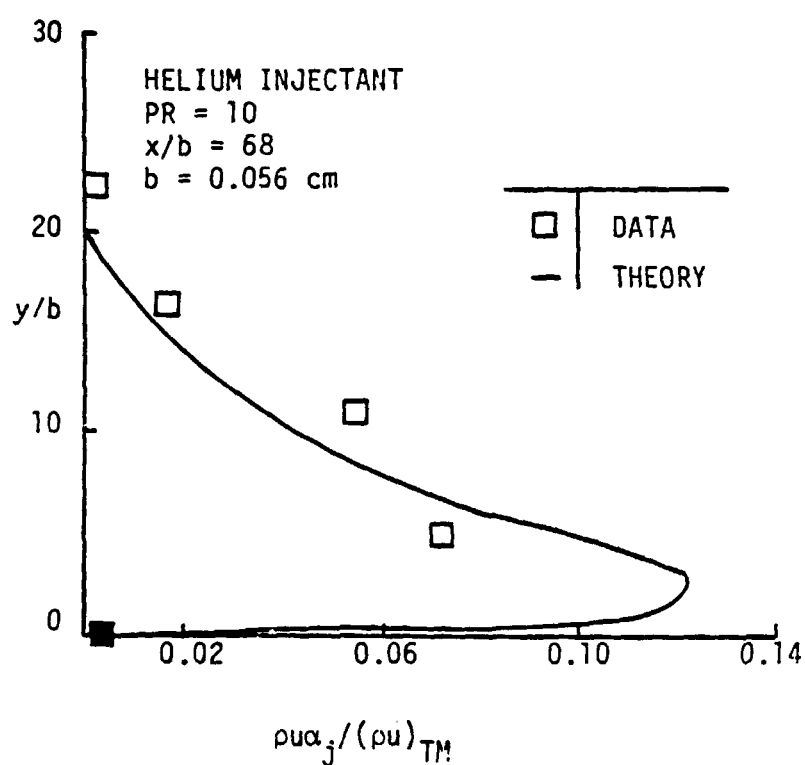


Fig. 30. Comparison of injectant mass flux profile.

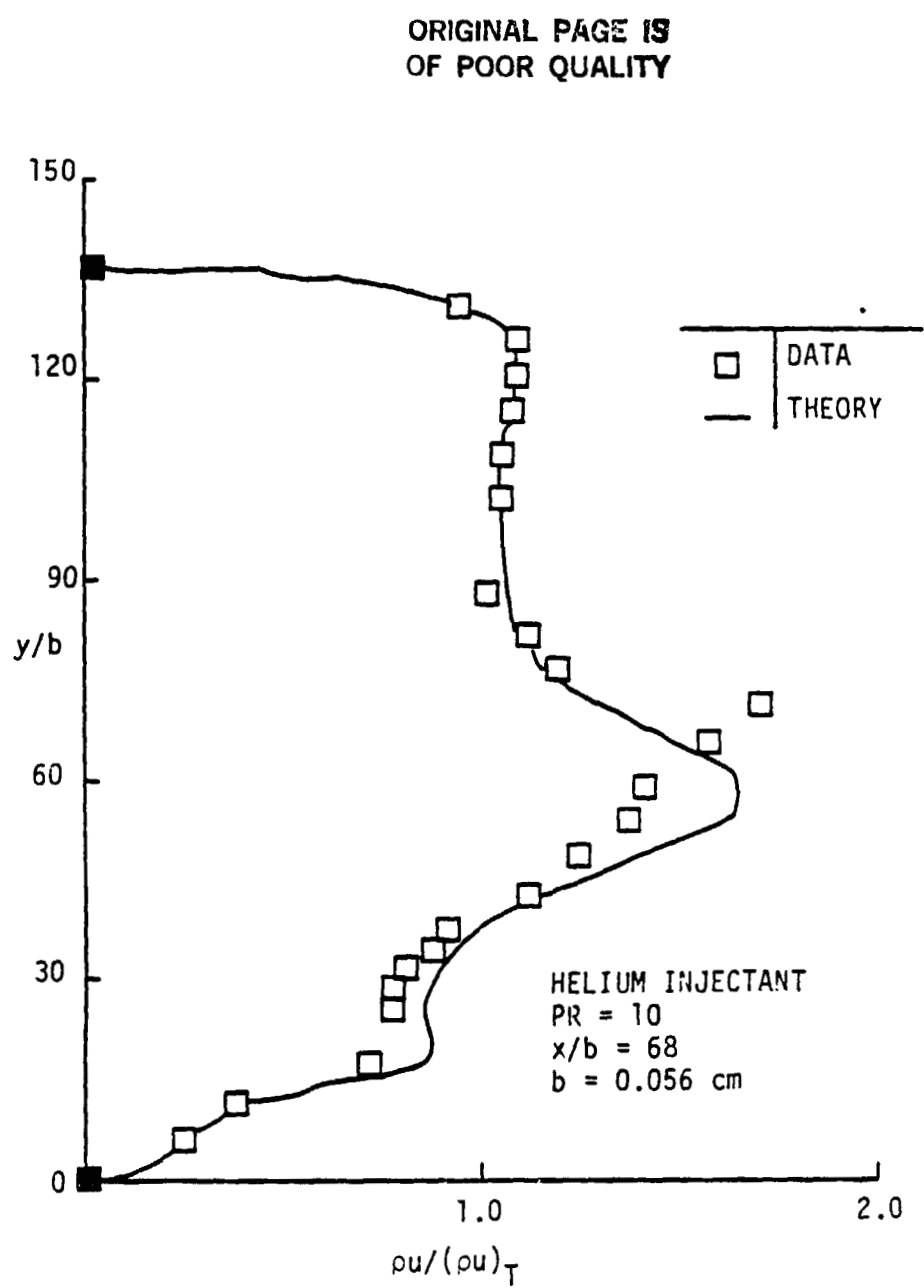


Fig. 31. Comparison of total mass flux profile.

ORIGINAL PAGE IS
OF POOR QUALITY

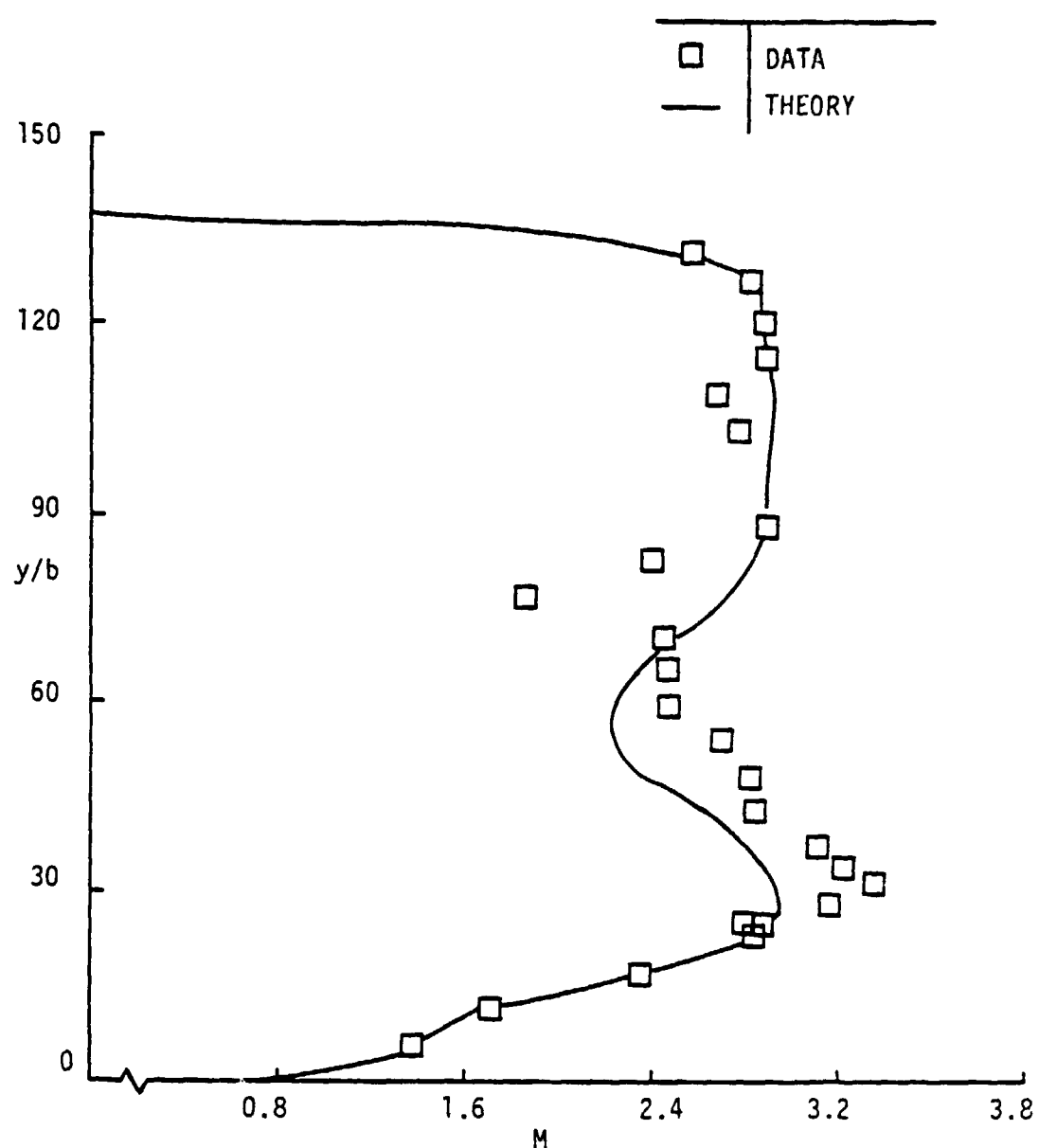


Fig. 32. Comparison of Mach number profile.

described by this computational analysis. Aside from a few noted exceptions, the theoretical results compare very well with the data. The locations of upstream boundary layer separation and downstream bow shock are underpredicted. Also, the recompression and bow shock are underpredicted by the theory. The concentration of injectant is overpredicted in the near surface region. The grid size and turbulence model used in the theory may have caused these differences. Since the computer code was not optimized for the particular experimental conditions, it should be considered valid due to the generally good agreement with data for this complex flow field.

6. CONCLUDING REMARKS

The flow field near a two-dimensional jet has been investigated. From a perpendicular slot nozzle, an underexpanded helium or nitrogen jet has been injected into a confined Mach number 2.9 flow. The flow field produced by the jet mixing and interaction has been investigated over a range of jet parameters. The jet parameters considered were the injectant species, jet static pressure, and gap width. Surface distribution and downstream profile data were used to develop empirical correlations and as a data base for an existing flow theory.

The flow field disturbance is increased by increasing the gap-width, increasing the jet static pressure, or injecting helium instead of nitrogen. The relative change in jet momentum was determined by the product of the gap width, jet static pressure, and injectant's specific heat ratio. This product was directly related to the relative size of the flow field disturbance, and was related linearly to the upstream separation distance. Using the upstream separation distance, a correlation has been developed to relate the upstream (or downstream) surface pressures into a single distribution for the jet conditions examined. The downstream injectant penetration height is directly proportional to the upstream separation distance. Thus, the surface disturbance and downstream-mixing limit are dependent on the relative change in the jet momentum.

For a particular injectant species, methods have been developed to correlate the data based on the relative change in the jet momentum (i.e., the product of the gap width and jet static pressure). The extent of mixing and interaction of the jet with the mainstream is related directly to the change in either the gap width or relative change in jet momentum. The flow-field disturbance is only slightly affected by the injectant used; however, the mixing in the flow field is affected greatly. The change in the flow field features can be related to changes in the jet parameters examined.

Results from an elliptic flow theory were compared with the data. The essential features of the complex flow field have been described by this computational analysis. Aside from the few noted exceptions, the theoretical results compare very well with the data. The theory underpredicts locations of upstream boundary layer separation and downstream bow shock, and the recompression and bow shock strengths. The concentration of injectant is overpredicted in regions closer to the surface. The computational grid size and turbulence model used in the theory may have caused these differences. Since the analysis was not optimized for the particular experimental conditions, and because of the uncertainty of the accuracy of the mole fraction downstream of the injector in the recirculation region, the code should be considered valid because of the reasonably good agreement with data for this complex flow field.

REFERENCES

1. Jones, R. A. and Huber, P. W., "Airframe-Integrated Propulsion System for Hypersonic Cruise Vehicles," Presented at the 11th Congress of the Aeronautical Sciences, Lisbon, Portugal, September 1978.
2. Sterrett, J. R., Barber, J. B., Alston, D. W., and Romeo, D. J., "Experimental Investigations of Secondary Jets from Two-Dimensional Nozzles with Various Exit Mach Numbers for Hypersonic Control Application," NASA TND-3795, January 1967.
3. Drummond, J. P. and Weidner, E. H., "A Parametric Study of Staged Fuel Injector Configurations for Scramjet Applications," AIAA Paper No. 81 - 1468, July 1981.
4. Rogers, R. Clayton, "A Two-Dimensional Model of the Interaction of a Transverse Jet in a Supersonic Stream with Application to Supersonic Stream," Ph.D. Thesis, 1979, North Carolina State University at Raleigh.
5. Werle, M. J., "A Critical Review of Analytical Methods For Estimating Control Forces Produced by Secondary Injection; The Two-Dimensional Problem," NOLTR-68-5, Naval Ordnance Laboratory, White Oak, Maryland, January 1968.
6. Spaid, F. W. and Zukoski, E. E., "A Study of the Injection of Gaseous Jets from Transverse Slots with Supersonic External Flows," AIAA Journal, Vol. 6, No. 2, February 1968, pp. 205-212.
7. Neilson, J. H., Gilchrist, A., and Lee, C. K., "A Theory for the Side Force Produced in Two-Dimensional Nozzles by Secondary Gas Injection," Aeronautical Journal, Vol. 72, pp. 267-274, March 1978.
8. Kaufman, L. G. and Koch, F., "High Speed Flows Past Transverse Jets," RE - 348, Grumman Aircraft Engineering Corp., Bethpage, New York, October 1968.
9. Wu, J. M. and Aoyama, K., "Analysis of Transverse Secondary Injection Penetration into Confined Supersonic Flow," AIAA 7th Aerospace Sciences Meeting, AIAA Paper No. 69-2, January 1969.
10. Werle, M. J., Driftmeyer, R. T., and Shafter, D. G., "Jet Interaction-Induced Separation of Supersonic Turbulent Boundary Layers - The Two-Dimensional Problem," AIAA 3rd Fluid and Plasma Dynamic Conference, Los Angeles, California, Paper No. 70-765, June 1970.

11. Werle, M. J., Driftmeyer, R. T., and Shafter, D. G., "Down-stream Pressure Distributions for Two-Dimensional Jet Interaction," AIAA Journal, Vol. 8, No. 6, June 1970, pp. 1165-1167.
12. Thayer, W. J., "The Two-Dimensional Separated Flow Region Upstream of Inert and Chemically Reactive Transverse Jets," Ph.D. Thesis, Department of Mechanical Engineering, University of Washington, March 1971.
13. Young, C. T. K. and Barfield, B. F., "Viscous Interaction of Sonic Transverse Jets with Supersonic External Flows," AIAA Journal, Vol. 10, No. 7, July 1972, pp. 853-855.
14. Spaid, F. W., "Two-Dimensional Jet Interaction Studies at Large Values of Reynolds and Mach Numbers," AIAA Journal, Vol. 13, No. 11, November 1974, pp. 1430-1434.
15. Andreev, A. E. and Shmanenkov, V. N., "Separation-Zone Parameters Ahead of a Jet Obstacle," Transactions of Izvestiya Akademii Nauk SSSR-Mikharika Zhirkosti i Gaza, Vol. 10, No. 2, June 1976, pp. 287-291.
16. Krishtal, V. I., "Application Factor of Two-Dimensional Transverse Sonic Jet Interacting with Supersonic Stream," Izvestiya VVA, Aviationsnaya Tekhnika, Vol. 22, No. 1, January 1979, pp. 102-105.
17. Broadwell, J. E., "Analysis of the Fluid Mechanics of Secondary Injection for Thrust Vector Control," AIAA Journal Vol. 1, No. 5, May 1963, pp. 1067-1075.
18. Hsia, H. T., Karamcheti, K., and Seifert, H. S., "Perturbation of Supersonic Flow by Secondary Injection (U)," Journal of Spacecraft, Vol. 2, No. 1, 1965, pp. 67-72.
19. Pinckney, S. Z., "A Short Static-Pressure Probe Design For Supersonic Flow," NASA TN D - 7978, July 1975.
20. Trexler, C. A., "Instant-Reply Data System For Combustion Tests," Presented at the 17th JANNAF Combustion Meeting, Hampton, Virginia, September 1980.
21. McClinton, C. R., NASA Langley Research Center, Hampton, Virginia, Personal communication.
22. Anon., "Equations, Tables, and Charts for Compressible Flow," NASA TR 1135, 1953.
23. Zukoski, E. E., "Turbulence Boundary Layer Separation in Front of a Forward Facing Step," AIAA Journal, Vol. 5, No. 10, October 1967, pp. 1746-1753.

24. Schlichting, H., Boundary Layer Theory, McGraw Hill, New York, Vol. 7, 1979.
25. Torrence, M. G., "Concentration Measurements of an Injected Gas in a Supersonic Stream," NASA TN D - 3860, January 1967.
26. McCormack, R. W. and Baldwin, E. S., "A Numerical Method for Solving the Navier-Stokes Equations with Application to Shock-Boundary Layer Interactions," AIAA Paper No. 75 - 1, January 1975.
27. Smith, R. E. and Weigel, B. L., "Analytic and Approximate Boundary Fitted Coordinate Systems for Fluid Flow Simulation," AIAA Paper No. 80 - 0192, January 1980.
28. Bogdonoff, S. M., "Some Experimental Studies of the Separation of Supersonic Turbulent Boundary Layers," Princeton University Report 336, June 1955.
29. Kistler, A. L., "Fluctuating Wall Pressure Under a Separated Flow," Journal Acoustical Society of America, Vol. 36, March 1964, pp. 543-550.
30. Speaker, W. V. and Ailman, C. M., "Spectra and Space Time Correlation of the Fluctuating Pressures at a Wall Beneath a Supersonic Turbulent Boundary Layer Perturbed by Steps and Shock Waves," NASA CR - 486, May 1966.

APPENDIX A

ERROR ANALYSIS

APPENDIX A
ERROR ANALYSIS

An error analysis was performed to examine the possible contribution of measurement errors in determination of the Mach number (M) and total mass flux (ρu). The measurement errors were considered from the supply temperature thermocouple (T_0), pitot pressure (p_t) transducer, static pressure (p) transducer, and composition analysis. The equations used assumed the flow was adiabatic and compared of a binary mixture of ideal gases (i.e., air and injectant). These equations were differentiated by a chain rule expansion for the measured flow parameters. In the final step, the derivatives were replaced by a finite difference representation.

The equations for the local Mach number error (ΔM) were determined for both the subsonic and supersonic cases. For this evaluation, the error in the mass averaged specific heat ratio (γ) was

$$\begin{aligned}\Delta\gamma/\gamma = \Delta\alpha_1 & \left\{ (C_{p_1} - C_{p_j}) / [\alpha_1 C_{p_1} + (1 + \alpha_1) C_{p_j}] + \right. \\ & \left. (C_{p_j} - \bar{R}_1 - C_{p_1} + \bar{R}_1) / [\alpha_1 (C_{p_1} - \bar{R}_1) + (1 - \alpha_1) (C_{p_j} - \bar{R}_j)] \right\}\end{aligned}$$

A.1

where the mass fraction measurement error of air (α_1) was determined

from the mole fraction error. The specific heat at constant pressure (C_p) and universal gas constant per gram molecular weight (\bar{R}) are constants for the particular gas. The error for the subsonic range of Mach numbers is given by

$$\Delta M/M = \frac{1}{2} \left\{ -\Delta \gamma / (\gamma - 1) + \Gamma^{1/\gamma} (\Delta p_t - p_t \Delta p/p) / p \right. \\ \left. + (\Delta \gamma / \gamma) [1 - \Gamma^{(\gamma-1)/\gamma} \ln(p_t/p)] \right\}$$

where $\Gamma = (\gamma - 1)p / (\gamma p_t)$

A.2

The error for the supersonic Mach number range can be found using the Rayleigh supersonic pitot formula, as

$$\Delta M/M = \left[4M^2 / [(\gamma - 1)(2M^2 - 1 - 1/\gamma)] \right]^{-1} \left\{ \Delta p_t / p_t - \Delta p/p - \right. \\ \left. [\Delta \gamma / (\gamma - 1)^2] [\ln(2\gamma M^2 - \gamma + 1) - \ln(r+1)] - \right. \\ \left. \Delta \gamma [(2\gamma M^2 + \gamma - 1) / [(\gamma + 1)(2M^2 \gamma - \gamma + 1)]] + \gamma / [(1 - \gamma)(1 + \gamma)] \right. \\ \left. + [1 / (1 - \gamma)] [1 - [\gamma / (1 - \gamma)] \ln \left[\frac{1}{2} (\gamma + 1) M^2 \right]] \right\} \quad A.3$$

The relative error of the Mach number ($\Delta M/M$) is used in the mass flux error determination.

The error in the mass flux was determined by assuming the flow

contains only the u velocity component. The mass flux error can be expressed in terms of the density (ρ), M , and the sound speed (a) by

$$\Delta(\rho u)/\rho u = \Delta\rho/\rho + \Delta M/M + \Delta a/a \quad A.4$$

Therefore, the error in the static temperature (T) and sound speed is needed in addition to Eqs. A.1, A.2, and A.3. By assuming that the local total temperature is the same as the supply temperature, the static temperature error is

$$\Delta T/T = \Delta T_t/T_t - [M\Delta M(\gamma-1) + \frac{1}{2} M^2 \Delta \gamma] [1 + \frac{\gamma-1}{2} M^2]^{-1} \quad A.5$$

The local sound speed error term can be determined by

$$\Delta a/a = \frac{1}{2} \{ \Delta \gamma/\gamma + \Delta T/T - [\Delta a_1 (\bar{R}_j - \bar{R}_1)] / [\alpha_1 \bar{R}_1 + (1-\alpha_1) \bar{R}_j] \} \quad A.6$$

By combining Eqs. A.4 to A.6, the mass flux error term can be expressed as

$$\begin{aligned} \Delta(\rho u)/\rho u &= \Delta\rho/\rho - \Delta T_t/2T_t + \\ &\quad 3\Delta a_1 (\bar{R}_j - \bar{R}_1) / [2(\alpha_1 \bar{R}_1 + (1 + \alpha_1) \bar{R}_j)] + \\ &\quad \Delta M(\gamma-1)M + M^2 \Delta \gamma/2[2 + (\gamma-1)M^2] \end{aligned} \quad A.7$$

Relative error in the Mach number and mass flux was examined over a range of Mach numbers from one to three, since the flow was

supersonic over most of the flow field. Also, the relative error terms were evaluated for helium or nitrogen injection over a range of mass fractions from zero to one. The tunnel supply conditions and assumed measurement error must be defined to obtain the relative error terms. The static and pitot pressure were determined by the Rayleigh supersonic pitot formula for a given value of M , injectant mass fraction (α_j), and for the nominal supply pressure of 2.07 MPa. Static temperature was determined for a particular value of M , α_j , and a nominal total temperature of 300 K. From Sec. 2.3, the values of the assumed measurement error were taken as 1. K for T_t , 862 Pa for P , 3.70 KPa for P_t , and 0.02 for the mole fraction. Results from three typical cases of M , α_j , and species are presented for discussion in Figs. A.1 and A.2.

Typical trends in the percent error in the calculated Mach number are shown in Fig. A.1. For nitrogen injection with $\alpha_j = 0.10$, the results are seen to have a small maximum percent error of 0.6 for $M = 1.75$. This trend with M for nitrogen injection was essentially the same for other values of α_j . For helium injection, the Mach number error is observed to have a large dependence on M and α_j . For values of $\alpha_j < 0.50$, the maximum error in M is less than 2.2 percent. As α_j decreases to 0.10, the error increased dramatically over the entire M range examined. The error in Mach number increases to a maximum of 9.2 percent for $M = 1.75$ and then decreases to about 4.5 percent by $M = 2.3$. The M error is essentially insignificant for nitrogen injection. However, the M error may be large in the mixing region for helium injection; essentially in regions of low helium concentration, where the M

ORIGINAL PAGE IS
OF POOR QUALITY

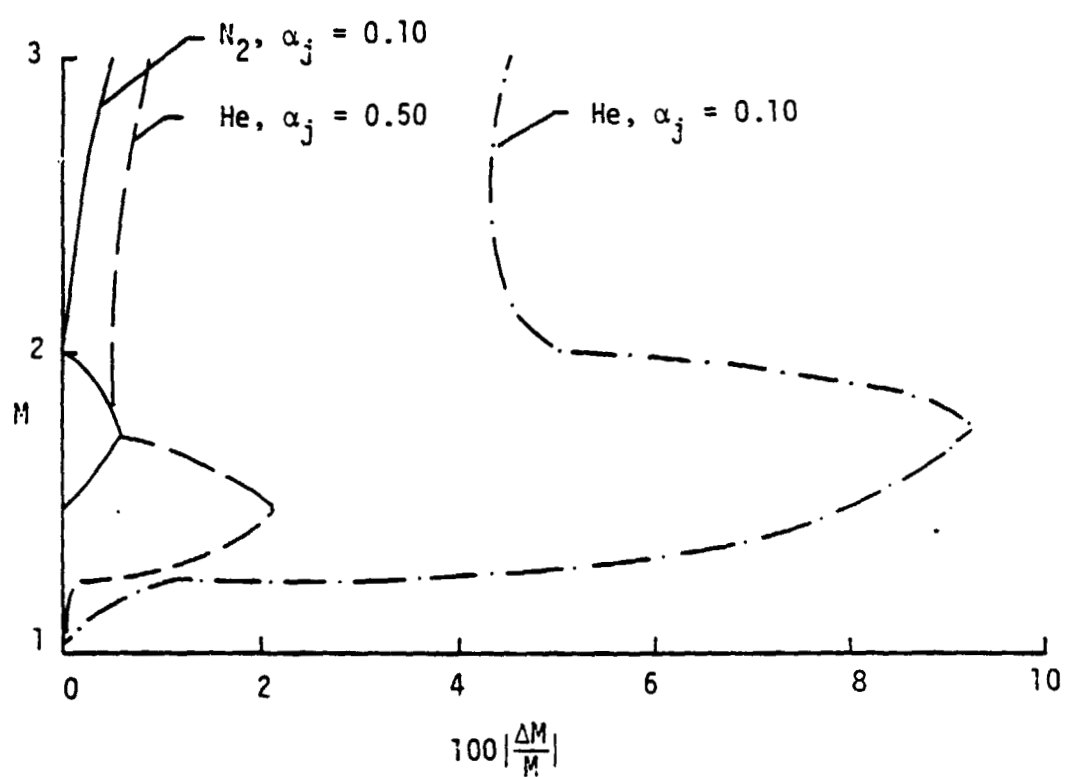


Figure A.1. Relative Mach Number Error.

error increases dramatically.

Typical trends for the mass flux error are shown in Fig. A.2. For nitrogen injection with $\alpha_j = 0.10$, the error increases from almost zero for $M = 1$ to 2.2 percent for $M = 3$. For helium injection with $\alpha_j = 0.10$, the trend and values are observed to be very similar to the nitrogen case except near a small peak at $M = 1.5$. A similar trend occurs for helium injection with $\alpha_j = 0.50$. For this case, the mass flux error rises to peak value (3.1 percent) at $M = 1.6$; then decreases to a local minimum of about 1.7% (for $M = 2.2$) before increasing to a value of 3.3 percent for $M = 3$. Therefore, these results show that the mass flux error as a result of measurement errors should be small for either helium or nitrogen injection.

The contribution of the measurement errors has been examined for both injectants. The measurement errors contribute less than a few percent error to the calculated local Mach number (for nitrogen injection) and mass flux. However, the possible measurement error contribution to the calculated Mach number may be large for helium injection in the mixing region, since the error increases dramatically with the decrease in helium concentration.

ORIGINAL PAGE IS
OF POOR QUALITY

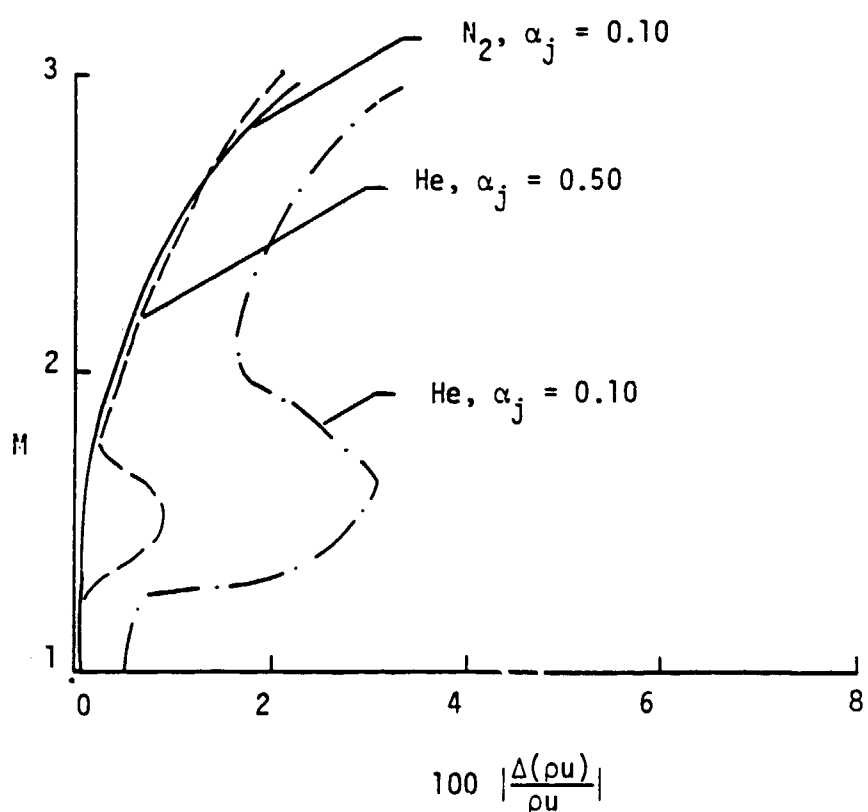


Figure A.2. Relative Mass Flux Error.